Bulk and Micro-scale Rheology of an Aging, Yield Stress Fluid, with Application to Magneto-responsive Systems

by

Jason P. Rich

B.S. Chemical Engineering, Cornell University (2006).

Submitted to the Department of Chemical Engineering
in partial fulfillment of the requirements for the degree of

Doctor of Philosophy in Chemical Engineering

at the

MASSACHUSETTS INSTITUTE OF TECHNOLOGY

February 2012

Author_____
Department of Chemical Engineering
February 15, 2012

Certified by_____
Patrick S. Doyle
Professor of Chemical Engineering
Thesis Supervisor

Certified by_____
Gareth H. McKinley
Professor of Mechanical Engineering
Thesis Supervisor

Accepted by_____
William M. Deen
Chairman, Department Committee on Graduate Students

Bulk and Micro-scale Rheology of an Aging, Yield Stress Fluid, with Application to Magneto-responsive Systems

by
Jason P. Rich

Submitted to the Department of Chemical Engineering
on February 15, 2012, in partial fulfillment of the
requirements for the degree of
Doctor of Philosophy in Chemical Engineering

Abstract

Understanding the ways that matter deforms and flows, which is the focus of the branch of science known as rheology, is essential for the efficient processing and proper function of such practically and technologically important materials as plastics, paints, oil-drilling fluids, and consumer products. Rheology is also powerful from a scientific perspective because of the correlation between rheological properties and the structure and behavior of matter on microscopic and molecular scales. The developing sub-field of microrheology, which explicitly examines flow and deformation behavior on microscopic length scales, provides additional clarity to this connection between rheology and microstructure. Aging materials, whose rheological properties evolve over time, are one class of materials that are of significant scientific and practical interest for their rheological behavior. Also, the unique field-responsive rheological properties of magnetorheological (MR) suspensions, which can be tuned with an applied magnetic field, have been used to create active vibration damping systems in such diverse applications as seismic vibration control and prosthetics.

A material that undergoes rheological aging and that has received much attention from soft matter researchers is the synthetic clay Laponite®. This material is attractive as a rheological modifier in industrial applications and consumer products because a rich array of rheological properties, including a yield stress, viscoelasticity, and a shear-thinning viscosity, can be achieved at very low concentrations in aqueous dispersions ($\sim$ 1 w%). Though this behavior has been investigated extensively using traditional 'bulk' rheology, a number of important questions remain regarding the nature of the dispersion microstructure. The techniques of microrheology, in which rheological properties are extracted from the motion of embedded microscopic probe particles, could help to elucidate the connection between microstructure and rheology in this material. Microrheological studies can be performed using passive techniques, in which probes are subject only to thermal motion, and active techniques, in which external forces are applied to probes.

Because aqueous Laponite® dispersions exhibit a significant yield stress, they could be beneficial as novel matrix fluids for magnetorheological suspensions. MR fluids consist of a suspension of microscopic magnetizable particles in a non-magnetic matrix fluid. When an external magnetic field is applied, the particles attract each other and align in domain-spanning chains of particles, resulting in significant and reversible changes in rheological properties. Because of the typically large density difference between the matrix fluid and the suspended magnetic particles, however, sedimentation is often problematic in MR fluids. A yield stress matrix fluid such as an aqueous Laponite® dispersion could help address this issue.

In this thesis, bulk rheology and microrheology experiments are combined in order to provide a thorough characterization of the rheological properties of aqueous Laponite® dispersions. Multiple Particle Tracking (MPT), a passive microrheology technique, is used to explore the gelation properties of dilute dispersions, while an active magnetic tweezer microrheology technique is used to examine the yield stress and shear-thinning behavior in more concentrated dispersions. MPT results show strong probe-size dependence of the gelation time and the viscoelastic moduli, implying that the microstructure is heterogeneous across different length scales. We also demonstrate the first use of magnetic tweezers to measure yield stresses at the microscopic scale, and show that yield stress values determined from bulk and micro-scale measurements are in quantitative agreement in more concentrated Laponite® dispersions. With a thorough understanding of the clay rheology, we study the magnetorheology of MR suspensions in a yield stress matrix fluid composed of an aqueous Laponite® dispersion. Sedimentation of magnetic particles is prevented essentially indefinitely, and for sufficient magnetic field strengths and particle concentrations the matrix fluid yield stress has negligible effect on the magnetorheology. Using particle-level simulations, we characterize the ability of the matrix fluid yield stress to arrest the growth of magnetized particle chains.

The methods and results presented in this thesis will contribute to the fundamental understanding of the rheology and microstructure of aqueous Laponite® dispersions and provide researchers with new techniques for investigating complex fluids on microscopic length scales. Additionally, our characterization of the effects of a matrix fluid yield stress on magnetorheological properties will aid formulators of MR fluids in achieving gravitationally stable field-responsive suspensions, and provide a new method for manipulating the assembly of particle building blocks into functional structures.

Thesis Supervisor: Patrick S. Doyle
Title: Professor of Chemical Engineering

Thesis Supervisor: Gareth H. McKinley
Title: Professor of Mechanical Engineering

Acknowledgments

I will forgo the cliché philosophical foray into what it means to complete a PhD and simply use this section to sincerely thank a number of people who have helped me along my path to this degree. I would first and foremost like to thank my advisors, Professors Patrick Doyle (Chemical Engineering) and Gareth McKinley (Mechanical Engineering), who have guided this work in both the day-to-day details as well as the larger direction and context. I feel that this co-advising arrangement provided me with a unique doctoral experience, exposing me to a greater diversity of fields and perspectives than a single advisor could offer. I am thankful for the complementary, balanced way in which they advised me, both equally contributing to this work. I appreciate Prof. Doyle for teaching me to explore problems and physical mechanisms in great depth, to think critically about results, and to build sound scientific arguments. For Prof. McKinley's part, I am grateful for his energy, encouragement, and generosity with his time despite myriads of responsibilities. I am also thankful for Prof. McKinley's attention to detail in preparing manuscripts and conference presentations. This set of careful and critical advisors has given me confidence that any of my work that makes it through both of their scientific 'filters' will be of high quality.

I also wish to thank other members of the M.I.T. community who have contributed to this work and/or my graduate experience. I am thankful to my thesis committee members, Professors T. Alan Hatton and Anette ('Peko') Hosoi, who have given me advice and provided a sounding board for ideas. I would also like to acknowledge Professors Preetinder Virk and Robert Armstrong, for whom I served as a Teaching Assistant for the undergraduate Fluid Mechanics course, 10.301.

I thoroughly enjoyed this experience, and it was a pleasure to teach such bright, energetic, and dedicated students. I am thankful to all my colleagues from the Doyle and McKinley groups for their friendliness and for their help in various capacities. I would particularly like to mention Matthew Helgeson, Ramin Haghgooie, Thierry Savin, David Appleyard, Ki-Wan Bong, Daniel Trahan, Daniel Pregibon, Murat Ocalan, Thomas Ober, and Randy Ewoldt, all of whom provided valuable advice and/or training, and many of whom contributed directly to the work in this thesis. I offer a special thanks to Professor Jan Lammerding of Harvard Medical School and Brigham and Women's Hospital (now at Cornell University), with whom I collaborated for the work in Chapter 3 of this thesis. Aside from science, I would like to sincerely thank the members of the M.I.T. Festival Jazz Ensemble, especially director Dr. Frederick Harris, for all the fun times spent pursuing my musical passions away from the rigors of research. I am also very grateful to Vivek Sharma, a postdoctoral researcher in the McKinley group, who was instrumental in helping me to find employment after graduation.

Going back in time, I wish to thank teachers and mentors from my undergraduate years who had lasting impacts on my scientific and overall academic development. I am especially thankful to Professor Donald Koch at Cornell University, who gave me my first opportunities in research and who provided invaluable guidance throughout the graduate school application process. I am also grateful to Professor Eric Shaqfeh (Stanford), Dr. Victor Beck (Stanford), Dr. Darran Cairns (3M), and Dr. Birbal Chawla (ExxonMobil) for their scientific mentorship and encouragement. Going back even further, I offer a special thanks to Ms. Regina Levine, Mr. Thomas Ryan, and Dr. Kimberly Smith. These teachers at Wakefield High School (Wakefield, MA) helped inspire in me a passion for learning and taught me the value of dedication and hard work.

Aside from science and academics, I am very grateful to all my friends and family who have been sources of encouragement and support through these years. I thank the members of the Melrose Church of Christ in Melrose, MA, especially the leadership and fellow students in the campus ministry, for their brotherly kindness, generosity, and love over these 5 years, and for regularly reminding me of what is truly important. Attending graduate school so close to my hometown has allowed me to stay connected with longtime friends, especially Chris Eaton, Ed Dunn, and John Luciani; I am thankful for their encouragement and for the chances they gave me to temporarily escape from M.I.T. I am especially grateful for the friendship and love of my girlfriend, Rebecca Jones, who has encouraged me, bared with me, and helped me keep perspective amidst the ups and downs of this PhD. It has also been a distinct blessing during these past 5 years to be so close to my family, who have given me incalculable support in my educational endeavors and have frequently welcomed me when I needed a break from research. Special thanks go to my grandparents, Robert and Marie Sciascia, with whom I lived prior to starting at M.I.T.; my aunt and uncle, Marcy and Richie Mignosa, who's enthusiastic support in all my pursuits has been unwavering since I was a child; and my father, Paul Rich, who's financial support made possible my Cornell education (and, by extension, my acceptance at M.I.T.). I would most of all like to thank my mother, Elaine Sciascia, who, having never attended college herself, has inspired me for as long as I can remember to set high academic goals and pursue educational advancement. This thesis is a testament to her constant dedication, encouragement, prayers, faith, and love, even in the midst of adverse circumstances. Finally, I reserve my highest and utmost thanks for The Lord my God and my Savior Jesus Christ, who have given me the strength to overcome the challenges of completing this degree, and who are the ultimate authors of and reasons for my life.

Acknowledgement for financial support of this work is given to the National Defense Science

and Engineering Graduate Fellowship program (U.S. Department of Defense, administered by the American Society of Engineering Education) and the Donors of the American Chemical Society Petroleum Research Fund (ACS-PRF Grant No. 49956-ND9).

Table of Contents

List of Figures

List of Tables

CHAPTER 1

Introduction

1.1 Rheology

Though the term 'rheology' is unfamiliar even to many scientists and engineers, so much so that it has often been assumed to be a misprint of 'theology' [1], it is a branch of science that is closely connected with everyday experiences. Rheological properties are exploited when spreading mayonnaise on a piece of bread; squeezing toothpaste onto a toothbrush; brushing, rolling, or spraying paint on a wall; applying cosmetic products; or stepping around muddy soil [2]. The classic definition of rheology is 'the study of the deformation and flow of matter' [3]. Typically, rheology is distinguished from the broader fields of fluid mechanics and solid mechanics by its focus on 'complex fluids' and 'soft solids'. This distinction often provokes the question of just what is it about the way a material flows or deforms that makes it 'complex'. Though a rigorous answer to this question is purely mathematical (the flow and deformation of 'simple' fluids and solids follow well-defined models that are not obeyed by complex fluids and soft solids), complex fluid behavior can be readily distinguished and observed phenomenologically [4]. For example, shaving cream can be differentiated from simple fluids like water or honey in that while it maintains its shape at rest and does not flow due to gravity (like a simple solid), it flows readily when sheared or pressed between two hands (like a simple liquid). In other words, the material is effectively a solid until sufficient stress is applied, at which point the material 'yields' and flows like a liquid. This combination of solid-like and liquid-like behavior is a hallmark of complex fluids. Other examples include Silly Putty®, which bounces like an elastic solid when thrown against a surface, but pools

like a liquid when left quiescent for about 30 minutes or more. The primary tasks of the rheologist are to characterize and quantify this type of mechanical behavior, as well as to connect deformation and flow properties to the physiochemical structure of materials.

From a chemical engineering perspective, because such a large number of practically and technologically important condensed materials cannot be described as simple liquids or simple solids, rheology plays a key role in industrial processing and product development. The typical chemical plant features hundreds of pipelines and process units through which fluids flow. Therefore, an understanding of complex, or so-called 'non-Newtonian', flow behavior is often essential to efficient processing and fluids handling [5]. For example, in the manufacture and packaging of hair conditioning products, non-Newtonian flow behavior can lead to complications when the product is forced through a nozzle in an attempt to fill the packaging bottle. Because of the gel-like nature of hair conditioners, the product tends to form a mound in the center of the bottle that must be distributed in order to fill the bottle completely [6]. Rheology is also essential in the manufacture of many plastics. Production processes such as injection molding and extrusion rely on detailed models of the complex flow behavior of the polymer melts from which plastics are formed [7]. In product development, rheology control is an important concern for the shelf-life and end-use of materials such as processed foods, paints, consumer products like toothpaste, and personal care products like cosmetics. In all of these cases, the rheological properties of the product must be optimized to ensure proper function.

Perhaps the most powerful aspect of rheology is that it provides fundamental insight into the physiochemical properties of complex fluids and soft materials. Because the microstructure of a material is closely correlated with its flow and deformation behavior, rheological measurements provide a window into molecular and micro-scale architecture and dynamics, as well as clues about the interactions between components [2]. By applying suitable models, rheological properties can be related to, for example, the relaxation time of polymer molecules [8], the critical conditions under which gelation occurs in a polymer solution or colloidal dispersion [9], or the nature of interactions between surfactant micelles and suspended nanoparticles [10]. It is this kind of fundamental physiochemical and microstructural insight that is the primary goal of the rheological studies presented in this thesis.

1.1.1 Measuring Bulk Rheological Properties

A large number of instruments and protocols are available for measuring rheological properties of complex fluids on the bulk scale [11]. The most common flows used for rheological measurements generally fall into two categories: *shear flows*, and *extensional flows* (also known as '*elongational flows*'). The work in this thesis primarily involves shear rheometry, which is described further below. For information about extensional rheometry, and its distinction from shear rheometry, interested readers are referred to the textbooks by Bird *et al.* [8] and Macosko [11].

Fig. 1.1 shows three typical arrangements for shear rheometry. In all three setups, a fluid sample that fills the gap between solid surfaces is subjected to shear when one of the surfaces is rotated around its central axis (by applying a torque or angular velocity), as indicated in the figure. In the geometry on the left, the fluid is held between parallel plates, while a cone-and-plate arrangement is shown at the center. In Fig. 1.1(c), the fluid lies in a cylindrical gap, and a thin cylindrical solid is inserted from the top into the center of the gap; this arrangement is known as a double-gap concentric cylinder Couette geometry, and is especially useful for studying low viscosity fluids due

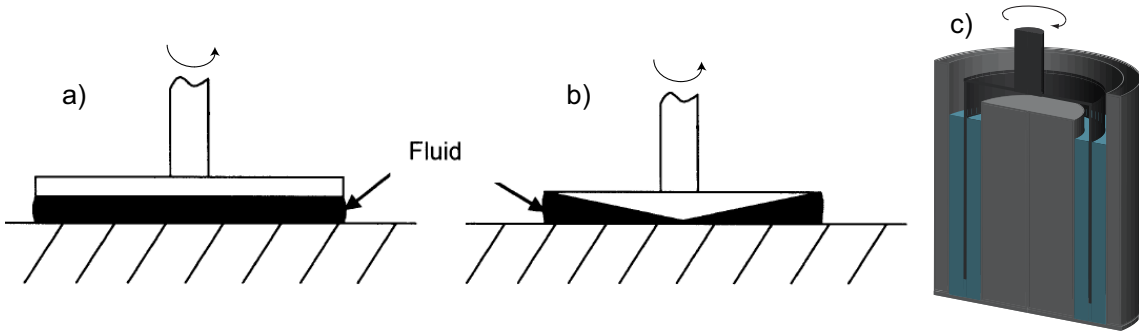

Fig. 1.1: *Geometries used for shear rheometry experiments. In all cases, the fluid sample fills a gap between solid surfaces, one of which is rotated to produce a shear flow in the fluid. The geometries shown are (a) parallel-plate, (b) cone-and-plate, and (c) a cross-section of a double-gap concentric cylinder Couette setup. The top of each geometry is attached to the spindle rod of a rheometer, which exerts a precise torque, angular strain, or angular velocity. Images (a) and (b) are adopted from [12].*

to the relatively large amount of surface–fluid contact area on the inside and outside of the rotated cylinder. Two basic types of rheometer instruments are available for carrying out shear rheology tests: *stress-controlled* rheometers and *strain-controlled* rheometers. Stress-controlled rheometers can apply very precise torque values to rigid fixtures in contact with fluids (as in Fig. 1.1) and measure the resulting angular strain and angular velocity, from which rheological properties are extracted. The bulk rheology studies described in this thesis were obtained using a stress-controlled rheometer. In contrast, strain-controlled rheometers can apply very precise angular strains and angular velocities. A torque transducer reports the resulting torque on the geometry. Most modern rheometers have tight feedback control mechanisms that allow a rheometer optimized for stress-controlled tests to also operate in a strain-controlled mode, and *vice versa*.

A large number of fluid properties can be measured with rheological experiments using geometries like those in Fig. 1.1. Techniques for measuring three common properties, of relevance to this thesis, are described here. Perhaps the most simple and fundamental property of a fluid is its viscosity, η, which can be measured using a test known as a *rate sweep*. In this test, known shear rates, $\dot{\gamma}$, are applied to the fluid and the resulting steady-state shear stresses, τ, are measured, yielding the viscosity as a function of shear rate with the equation:

$$\eta\left(\dot{\gamma}\right) = \tau/\dot{\gamma} \tag{1.1}$$

Though simple Newtonian fluids by definition have a constant viscosity, complex fluids often exhibit a viscosity that depends on the shear rate, as implied by Equation 1.1. Many complex fluids exhibit a decrease in the viscosity with increasing $\dot{\gamma}$, a property known as *shear-thinning*. Examples of shear-thinning fluids include ketchup, and many polymer solutions. The opposite phenomena, in which the viscosity increases with increasing $\dot{\gamma}$, is known as *shear-thickening*. This type of behavior can occur in dense particle suspensions due to microstructural 'jamming' [13].

Shaving cream was described above as exhibiting a threshold applied stress below which it maintains its shape like a solid, and above which the material flows like a liquid. This is an example of yielding phenomena, and the critical stress to induce flow is known as the *yield stress*, τ_y. There has been much debate in the rheology community about whether a true yield stress exists: that is, whether materials can truly be described as solid ($\eta \to \infty$) at applied stresses below the yield stress, or if there is actually a very large, but finite viscosity (see [14, 15, 16] for the arguments in this debate). Independent of whether there is a true solid–liquid transition at a critical applied stress, it is universally accepted that the concept of the yield stress is practically useful for characterizing flow behavior and understanding the associated microstructure; therefore, the work in this thesis employs the terminology of 'yield stress' materials without further comment on this debate. The yield stress can be a difficult parameter to measure precisely; despite the fact that there are numerous methods available for measuring the yield stress [17], different methods often give conflicting results [18]. In this thesis, because of complications arising from the time-dependent behavior of the fluids under study (see Section 1.3), the *stress ramp* test is the most suitable and straight-forward method for measuring the yield stress [14]. In this test, the shear stress on the fluid (i.e., the torque on the upper geometry in Fig 1.1) is slowly and continuously increased until there is a large jump in the shear rate and the material flows. τ_y is extracted as the value of the stress when this sudden increase in shear rate is observed.

While yield stress fluids undergo a transition from solid-like to liquid-like behavior at a critical applied stress, many complex fluids exhibit some combination of solid-like and liquid-like character simultaneously. This behavior is known as *viscoelasticity*. Perhaps the most straight-forward way to understand viscoelasticity is to understand how it is measured. Consider a fluid sample in one of the geometries shown in Fig. 1.1 and the case where a sinusoidal shear strain $\gamma(t) = \gamma_0 \sin(\omega t)$ with frequency ω is applied to the fluid. We consider the case where γ_0, the strain amplitude, is small enough that the internal structure of the material is not significantly altered by the application of the strain. This type of test is called *small-amplitude oscillatory shear* (SAOS), and the response of the fluid is referred to as its *linear* rheology (as opposed to *nonlinear* rheology, in which large deformations and/or deformation rates are applied that significantly disrupt the internal structure of the material). For the case of SAOS, the measured shear stress output, $\tau(t)$, is also necessarily sinusoidal, but generally has a phase shift δ:

$$\tau(t) = \tau_0 \sin(\omega t + \delta) \tag{1.2}$$

This expression can be expanded using trigonometric identities to arrive at the standard expression for the shear stress in SAOS [3]:

$$\frac{\tau(t)}{\gamma_0} = G' \sin(\omega t) + G'' \cos(\omega t) \tag{1.3}$$

where G' and G'' are the *storage* and *loss* moduli, respectively, given by:

$$G'(\omega) \equiv \frac{\tau_0}{\gamma_0} \cos(\delta) \qquad G''(\omega) \equiv \frac{\tau_0}{\gamma_0} \sin(\delta) \tag{1.4}$$

G' and G'' are related through the tangent of the phase shift, known as the *loss tangent*.

$$tan(\delta) = G''/G' \tag{1.5}$$

Since, in oscillatory shear, the stress in an elastic solid is in phase with the strain ($\delta = 0$, i.e., solids respond to stress by undergoing *deformation*) and the stress in a Newtonian liquid is in phase with the strain rate ($\delta = \pi/2$, i.e., liquids respond to stress by undergoing *flow*), Equation 1.3 shows that G' and G'' are the elastic and viscous contributions to the stress, respectively [3]. Equivalently, from Equation 1.5, $G''/G' \to 0$ for an elastic solid, and $G''/G' \to \infty$ for a Newtonian liquid.

1.2 Microrheology

Despite the power of rheology to elucidate complex fluid behavior, there are important situations in which traditional rheological analysis is impractical or unfeasible. Some disadvantages of traditional 'bulk' rheology include:

- The need for milliliter volumes of fluid, which can make the analysis of some materials impossible or prohibitively expensive.
- The need to conduct measurements in specialized and (typically) expensive instruments, which often prevents the study of complex fluids in their native environments. This and the previous point present major challenges to the study of *in vivo* biological fluids, for example.
- The fact that bulk scale measurements represent an average over milliliter volumes, which precludes the study of phenomena at smaller length scales in complex fluids, such as micro-scale spatial heterogeneities.
- The inertia of the measuring apparatus, which can produce artifacts in data during measurements at high frequencies. Instrument inertia also presents challenges for rheological measurements of very soft or low viscosity materials.

The sub-field of microrheology has been developed to address the issues above [19]. Most manifestations of microrheology techniques involve tracking the motion of microscopic probe particles embedded in complex fluids and relating the observed dynamics to fluid rheological properties [20]. Because the probe particles are microscopic in size, only microliter or nanoliter volumes of material are necessary for analysis, and measurements of fluids in their native environments, such as *in vivo* studies of cell cytoplasm and other biofluids, can be more easily facilitated. Additionally, probe inertia is usually negligible up to much higher frequencies than are accessible in typical bulk rheology measurements. Finally, probe particles in microrheology experiments more directly yield information about the micro-scale structure and behavior of complex fluids, so that properties such as spatial heterogeneity can be quantified. It is also important to recognize that in structured fluids, there is often a length scale below which bulk rheological properties that are averaged over macroscopic volumes of fluid are no longer representative of the local mechanical environment. This length scale usually corresponds to some microstructural length scale in the system, like a characteristic pore size in a network, or a radius of gyration of dissolved polymer. These microstructural length scales are often essential to the proper function of the fluid, either in nature or in industry [21]. In cases where the size of probe particles is comparable to or smaller than the largest microstructural length scale in the system, microrheology can provide different information about a material than bulk rheology: the material is probed on a different length scale [22]. While this behavior can lead to erroneus conclusions when extrapolating microrheology results to the bulk

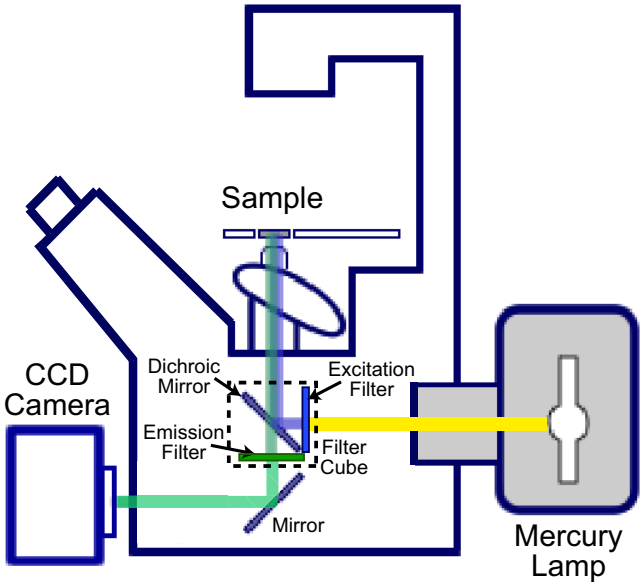

Fig. 1.2: *Schematic for the fluorescence microscopy setup used for Multiple Particle Tracking experiments. Light from a mercury arc lamp passes through an excitation filter and reflects off of a dichroic mirror to illuminate and excite the fluorescent probes in the sample. Light emitted from the fluorescent probe particles is transmitted through the dichroic mirror and passes through an emission filter, which isolates the emission spectrum of the particles. Filters and the dichroic mirror are housed in a filter cube. Image adopted from [25].*

scale [23], it also indicates that the *combination* of bulk rheology and microrheology can provide very thorough characterization of materials. In other words, microrheology is most powerful as a *complement* to bulk rheology, rather than as a replacement. Though specialized instrumentation has been developed, many microrheological techniques can be implemented with typical microscopy and diagnostic instrumentation readily available in many laboratories [24]. This is the case for Multiple Particle Tracking (MPT) microrheology, which is employed for the work described in Chapter 2. This and other common microrheology techniques are described below.

1.2.1 Microrheology Techniques

Microrheology techniques fall into two categories: *passive microrheology*, in which the probe motion is caused solely by Brownian bombardment from the surrounding fluid (i.e., thermal forces), and *active microrheology*, in which an external force is applied to the probe [24]. Passive microrheology is appropriate for studying the linear microrheology (small deformation and/or deformation rate) of very soft materials (moduli up to ~ 1 Pa), while active microrheology can be used for nonlinear measurements (large deformation and/or deformation rate) of stiffer and more viscous materials.

Numerous microrheology techniques have been developed. Three established techniques that involve tracking the motion of embedded probe particles are described below.

Multiple Particle Tracking (MPT)

Type: Passive

Description: Brownian motion of probe colloids (radius $a \sim 1$ μm) embedded in a fluid is visualized and captured directly via video microscopy. Typically, fluorescent particles are used in order to maximize the brightness contrast, increasing the spatial resolution. A standard setup, which matches that used for the work described in this thesis, is shown as a schematic in Fig. 1.2 (image from [25]). Light from a mercury arc lamp passes through an optical filter (the 'excitation' filter), which transmits only the range of wavelengths that causes fluorescence of the probe particles, then reflects off of a dichroic mirror to illuminate the sample. The resulting light emitted from the probes (i.e., the fluorescence), passes *through* the dichroic mirror as well as a final 'emission' filter, which transmits only a wavelength range corresponding to the fluorescence emission spectrum of the probes. This arrangement of filters and dichroic mirror maximizes the contrast of fluorescent probe particles against the background. The filtered emitted light then reaches the camera, which can be used in conjunction with appropriate software to capture videos of probe particle diffusion. Specialized software is applied to track the trajectories of each particle in a video [26], from which the ensemble-averaged mean-squared displacement $\left\langle \Delta x^2(\tau) \right\rangle$ can be calculated as a function of lag time, τ [27]. $\left\langle \Delta x^2(\tau) \right\rangle$ is the ensemble-averaged 1-dimensional displacement (horizontal, in the case of this thesis) that probes undergo when allowed to diffuse for a given time, called the lag time, τ (not to be confused with the applied stress as described above for bulk rheology, which is also traditionally denoted as τ). $\left\langle \Delta x^2(\tau) \right\rangle$ is the fundamental quantitative result of MPT experiments, from which rheological information is extracted. In a Newtonian fluid, the viscosity η is related to $\left\langle \Delta x^2(\tau) \right\rangle$ via the Stokes–Einstein equation, $\left\langle \Delta x^2(\tau) \right\rangle = \tau k_B T / 3\pi a \eta$, where k_B is the Boltzmann constant, T is the temperature, and a is the probe radius. However, Savin and Doyle [28] proposed that in order to extract accurate measurements from real MPT experiments as described above, the Stokes–Einstein equation must be modified to account for errors in the particle tracking experiment and data analysis. These authors showed that [28]

$$\left\langle \Delta x^2(\tau) \right\rangle = \frac{k_B T}{3\pi a \eta}(\tau - \sigma/3) + 2\epsilon^2 \tag{1.6}$$

where σ is the camera shutter speed (a dynamic error) and ϵ is the spatial resolution of the MPT experiment (a static error). ϵ can be measured by tracking probe particles immobilized in a stiff gel. Not accounting for these sources of error leads to spurious results, including non-zero values of the storage modulus even for Newtonian fluids. For more details about these sources of error and their implications, see [28]. Additional details regarding the particular MPT setup and experimental protocol in the present work, as well as a description of calculations to obtain additional rheological parameters, can be found in Section 2.3.2.

There are a number of advantages of the MPT technique over other methods of microrheology. Because specialized instruments are not necessary, implementation is relatively straightforward and inexpensive. Additionally, Brownian particles probe the fluid at all frequencies simultaneously, so that a large number of frequencies can be examined at once from a single video; the measureable frequencies are limited only by the frame rate of the camera and the length of a video (as long as particles do not diffuse out of focus over the time scale of a video). Finally, since a large number of particles are tracked at once, high statistical accuracy can be achieved and spatial properties such as heterogeneity can be explored. Because it is a passive technique, however, the stress applied by

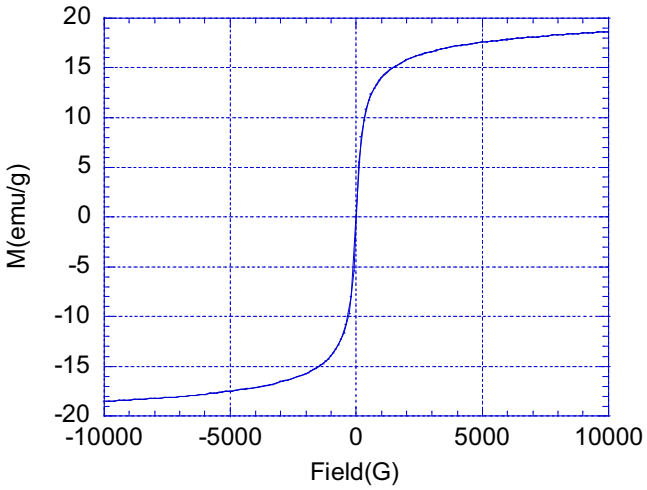

Fig. 1.3: *Magnetization curve for the superparamagnetic probe particles used for magnetic tweezer microrheology experiments in this thesis. The particles are M-450 Dynabead® particles, produced by Invitrogen Life Technologies (Carlsbad, CA), with an average diameter of* $d = 4.5$ *μm and a saturation magnetization of about 19 emu/g. The particles can be well-approximated as monodisperse. Magnetization data provided by Invitrogen Life Technologies (http://www.invitrogen.com).*

probes is on the order of $\sim k_B T/a^3$, which is typically ~ 1 Pa. For this reason, MPT is limited to very soft materials, with moduli less than about 1 Pa.

Magnetic Tweezers

Type: Active

Description: An external magnetic field imposes a force on magnetizable probe particles embedded in a fluid, and probe motions are visualized with video microscopy. The trajectories of the particles are tracked in a manner similar to MPT, and rheological data is extracted from the response [24]. Though various particle shapes can be used, and the kinematics of the induced flow surrounding the particle is highly dependent on the particle shape [29], spherical probe particles are widely available and the most common. Most studies employ superparamagnetic polymer-magnetite composite microspheres because they are available in monodisperse suspensions with well-defined magnetic properties. Though ferromagnetic particles generally exhibit a stronger magnetic response, they are usually less attractive for microrheological studies due to complications arising from magnetic hysteresis, polydispersity, and shape irregularity. Superparamagnetic particle sizes of about 0.1–10 μm with saturation magnetizations up to about 20 emu/g = 20 A·m^2/kg are available. The magnetization curve for the probe particles used in this thesis (see Chapter 3) is shown in Fig. 1.3. Upon application of an external magnetic field, $\mathbf{H}$, the magnetizable probe particles translate, rotate, or oscillate in response to the field. For the simple setup used in this thesis (see Chapter 3), only approximately unidirectional translation of magnetic probe particles is observed. In this case,

the applied magnetic field is approximately unidirectional ($\mathbf{H} = |\mathbf{H}|\mathbf{e}_x = H\mathbf{e}_x$), and the magnetic force, $\mathbf{F}_{mag}$, on an isolated particle of volume V is [30]:

$$\mathbf{F}_{mag} = \mu_0 \rho V (\mathbf{M} \cdot \nabla) \mathbf{H} = \mu_0 \rho M V \frac{dH}{dx} \mathbf{e}_x \tag{1.7}$$

where μ_0 is the magnetic permeability of free space, ρ is the particle mass density, and $\mathbf{M} = M\mathbf{e}_x$ is the magnetization of the particle per unit mass. Note that the magnetic force on a particle due to an external field is proportional to the magnetic field *gradient*, so that a spatially uniform field results in no net force on an isolated particle (though there are dipolar forces *between* particles in a uniform magnetic field, as will be discussed in Section 1.4). For translation experiments with spherical probes of radius a, the viscosity of the fluid can be found from Equation 1.1 by dividing the stress on the particle (obtained from calibration experiments in a fluid of known viscosity) by the shear rate, $\dot{\gamma}(x) = 3|U(x)|/2a$ where U is the measured velocity of the particle. Viscoelastic parameters can be found from oscillation experiments by employing the loss tangent given in Equation 1.5. Alternatively, the viscoelasticity can be estimated in a translation experiment by modeling the fluid with a mechanical equivalent circuit of springs and dashpots, and subsequently fitting the equation of motion from the model to the observed particle motion [31, 32]. Additional details regarding the particular magnetic tweezer setup and experimental protocol in the present work, as well as a description of calculations to obtain rheological parameters, can be found in Chapter 3.

The primary advantage of magnetic tweezer microrheology is its simplicity of mechanism and implementation (especially for unidirectional translation experiments), as well as the fact that relatively large forces can be achieved. For the experimental conditions in this thesis, stresses up to about 250 Pa are accessible. However, smaller numbers of particles are typically tracked (sometimes only one particle), which limits statistics and inhibits the study of spatial heterogeneity.

Optical Tweezers

Type: Active

Description: A probe particle embedded in a fluid is 'trapped' with incident laser light. Forward-scattered light is detected by a quadrant photodiode, allowing high spatial resolution tracking of the particle when the trap is translated [24]. Neglecting inertia, the equation of motion for a bead in an optical trap oscillating with a frequency ω and an applied force $F_0 \cos \omega t$ is [24, 33]:

$$6\pi\eta_{eff} a \frac{dx}{dt} + (k_f + k_t) x = k_t F_0 \cos \omega t \tag{1.8}$$

where η_{eff} is an effective fluid viscosity, and $k_f(\omega)$ and k_t are spring constants for the fluid and the trap, respectively. Measuring the resulting particle oscillation allows calculation of the true viscosity $\eta(\omega)$ and $k_f(\omega)$, which yields $G'(\omega)$ and $G''(\omega)$ [24].

$$G'(\omega) = \frac{k_f(\omega)}{2\pi a} \tag{1.9}$$

$$G''(\omega) = \omega(\eta(\omega) - \eta_s) \tag{1.10}$$

where η_s is the Newtonian viscosity of the pure solvent.

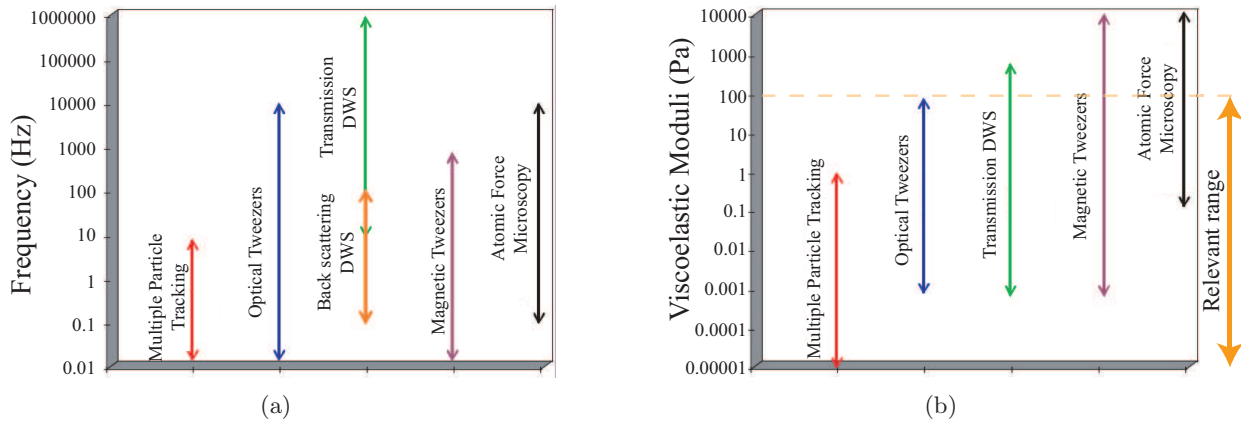

Fig. 1.4: *Measurable range of (a) frequency and (b) viscoelastic moduli for various microrheology techniques. The orange arrow on the right shows the relevant range of moduli for the materials studied via microrheology in this thesis. Images from [21].*

Though optical tweezer setups are usually more difficult to assemble than MPT setups or magnetic tweezer devices, they allow precise control over the position of the probe particle, so that particular regions of interest in a material can be explicitly explored. An additional advantage is the relative ease of conducting high-frequency oscillatory tests at various amplitudes. These detailed manipulations of a single particle come at the price of reduced statistics relative to multi-particle techniques like MPT.

Fig. 1.4 compares the ranges of frequency and moduli that can be probed with various microrheology methods (images from [21]). Note that DWS (Diffusing Wave Spectroscopy) measures laser light scattered from an ensemble of embedded colloidal probes [34], and atomic force microscopy extracts rheology from the response of an AFM tip immersed in a fluid [24]. The relevant range of viscoelastic moduli for the work in this thesis is up to about $\sim$ 100 Pa (see Fig. 1.6). Fig. 1.4(b) shows that combining magnetic tweezers and multiple particle tracking allows measurement over a wide range of viscoelastic moduli, from low viscosity liquids to soft solids having moduli or yield stresses greater than 100 Pa. These techniques also span a satisfactory frequency range [Fig. 1.4(a)], and are relatively straightforward and inexpensive to implement with available microscopy facilities.

1.3 Laponite®

Rheological studies in this thesis focus on a technologically and scientifically important microstructured material called Laponite®, a synthetic clay obtained from Rockwood Additives (Goncalves, TX). Dispersions of Laponite® in water exhibit a rich array of non-Newtonian behavior, including yield stress [35], viscoelasticity [36], shear-thinning [37], and rheological aging (that is, continual evolution of rheological properties over time) [37, 38, 39]. Further, the dispersion properties are highly tunable with concentration [35, 40], and for the 'RD' grade of Laponite® used in the present

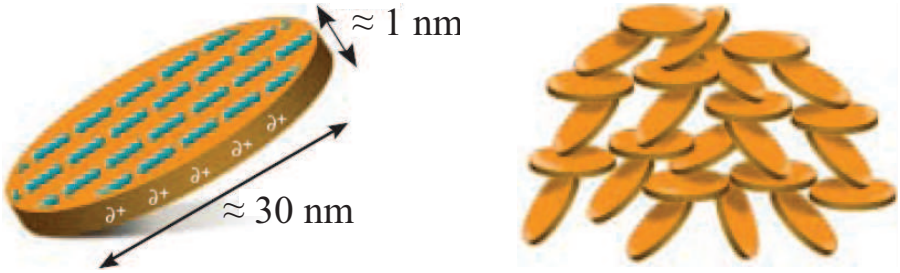

(a) (b)

Fig. 1.5: *(a) Schematic of a Laponite® platelet. Blue slashes indicate negative charges on the face of the disk, while small amounts of positive charge have been suggested on the rim. (b) Proposed 'house of cards' structure for Laponite® gels in water. The charge configuration in (a) leads to face-to-rim attractions that induce aggregation and gelation. Images from [42].*

study, soft solid states in aqueous dispersions can be formed at very low concentrations (as low as about 1 w%). For these reasons, Laponite® has been used as a rheological modifier in a number of technological and industrial applications [41, 42], and there has been significant fundamental interest in the microstructural mechanisms underlying its rheology and phase behavior [43].

1.3.1 Laponite® Platelets

Laponite® platelets are colloidal disks about 30 nm in diameter and 1 nm in thickness, with a reduced molecular formula of $[Na_{0.7}]^{+0.7}[(Si_8Mg_{5.5}Li_{0.3})O_{20}(OH)_4]^{-0.7}$ [42, 44]. The disk geometry and size have been verified by small angle x-ray scattering (SAXS) experiments [45, 46]. Due to the molecular structure of the Laponite® clay, platelets in aqueous dispersions exhibit a negative charge on each face and for pH less than about 11, appear to be positively charged along the rim [44, 47]. A schematic of a Laponite® platelet is shown in Fig. 1.5(a). Blue slashes indicate negative charges on the face of the disk. When dispersed in water, this charge configuration is thought to lead to the 'house of cards' structure in Fig. 1.5(b), though the structure at long times is still disputed and can be highly sensitive to conditions of pH and ionic strength. Previous reports have indicated the necessity of face-to-rim electrostatic attractions for inducing aggregation and gelation [48, 49].

Dissolution of Laponite® platelets in aqueous solutions can be problematic at acidic and neutral pH. Under these conditions, the following reaction breaks down the platelets [50, 51]:

$$[Na_{0.7}]^{0.7+}[(Si_8Mg_{5.5}Li_{0.3})O_{20}(OH)_4]^{0.7-} + 12\,H^+ + 8\,H_2O \longrightarrow 0.7Na^+ + 8\,Si(OH)_4 + 5.5Mg^{2+} + 0.3Li^+$$

To avoid dissolution, Laponite® is usually suspended at a pH of 10, and is stored in a nitrogen environment to hinder the uptake of CO_2, which lowers the pH over time through the formation of

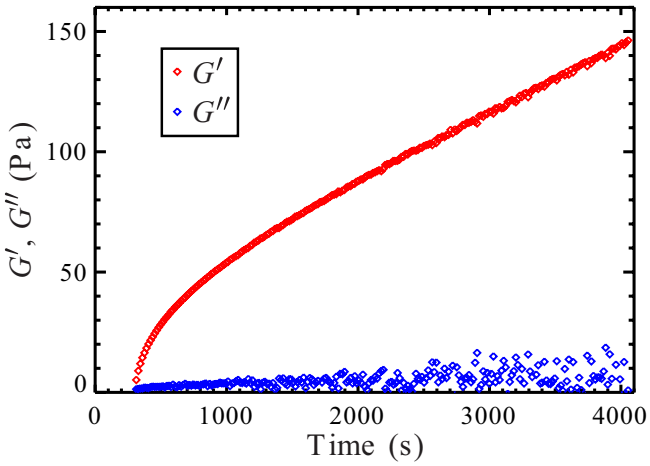

Fig. 1.6: *Linear viscoelastic moduli of a 1.5 w% aqueous Laponite® dispersion as a function of age time as measured with an SAOS time sweep test at a constant frequency of* $\omega = 1$ *rad/s. The stress amplitude is* $\tau_0 = 0.1$ *Pa, and the geometry is a 40 mm plate-plate arrangement with a 0.5 mm gap. The temperature is held constant at* $T = 25\ ^\circ C$*. While* G'' *remains small,* G' *continues growing steadily as the material ages.*

carbonic acid, H_2CO_3 [51].

1.3.2 Aqueous Laponite® Dispersions

Much controversy has surrounded the nature of aqueous Laponite® dispersions. Despite the debates, it has consistently been agreed that:

- Over a period of time that depends on the concentration, the viscosity grows by as much as 4 orders of magnitude, and both elasticity and a yield stress appear, also growing significantly with time (see Fig. 1.6 and [36]). This phenomena is characteristic of *rheological aging*; rapidly shearing the fluid (which is strongly shear-thinning) will '*rejuvenate*' the fluid by destroying structure developed during aging [37].
- The system does not reach an equilibrium state, but rather is kinetically trapped, having undergone an ergodic-to-nonergodic transition during the aging process [52].

During aging, the system evolves toward a state depending on the Laponite® concentration and the concentration of salt (i.e, the ionic strength of the solution), as seen in Fig. 1.7, which is a phase diagram from [43] compiled from a large number of studies. Note that Fig. 1.7 is not a true thermodynamic phase diagram, since the gel and glass states are kinetically trapped and are not true equilibrium states. The dashed green line in Fig. 1.7 shows the salt concentration used in this thesis, $C_s = 5.9$ mM. The phase map shows that there is ambiguity at this value of C_s as to the exact nature of the phase and microstructure of the aqueous Laponite® dispersions. The value of $C_s = 5.9$ mM was chosen before this information was fully available. It has been

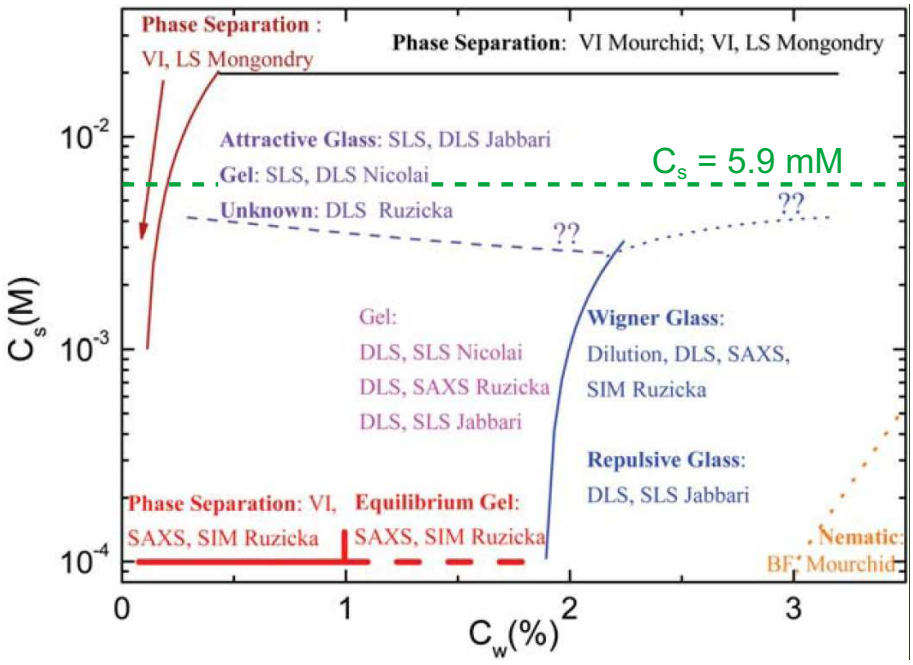

Fig. 1.7: *Proposed non-equilibrium phase diagram for aqueous Laponite® dispersions. Various nonergodic states are possible at long age times, depending on the salt concentration, C_s, and the Laponite® concentration in weight %. Results from various groups using a range of analysis methods are compiled and areas where uncertainty remains are noted. In this thesis, various Laponite® concentrations are examined at a salt concentration of $C_s = 5.9$ mM, which is noted with a dashed green line. Original image from [43]*

demonstrated, however, that the bulk rheology of aqueous Laponite® dispersions depends primarily on the Laponite® concentration; the flow behavior is far less sensitive to the salt concentration and the exact nature of the resulting phase [53]. Therefore, we focus here on what can be learned from rheology without concern for whether the arrested state is more appropriately described as a 'gel' or an 'attractive glass'. Attractive interactions between platelets are expected to dominate in both cases. Though we are unaware of any study directly comparing the microrheology of the different types of arrested states in Fig. 1.7, one aim of this thesis is to highlight this issue and spur further research. Independent of the exact nature of the nonergodic phase at long times, it has been demonstrated that arrested states of Laponite® can be characterized as *elasto-visco-plastic* fluids [2, 35]. That is, there is a yield stress, τ_y (i.e. plasticity), and significant viscoelasticity at stresses below τ_y [36]. The tunability of these properties with Laponite concentration has made aqueous Laponite® dispersions attractive as rheological modifiers in numerous applications, including paints, oil-drilling fluids, and consumer products like toothpaste [42]. Though much work has been done on the bulk rheology of discotic clays like Laponite® (see [36, 54, 55, 56] and the extensive review by Luckham [41]), their rheology on the microscopic scale has been studied in much less detail [57, 58, 59], despite the importance of micro-scale flow properties in many of the products in which Laponite® serves as a rheological additive. For example, in oil-drilling fluids, rock cuttings with sizes ranging from micrometers to centimeters must be entrained and removed from a well, and in paints, sedimentation and aggregation of micro-scale pigments must be inhibited. There remain important questions about the rheology of aqueous Laponite® dispersions on microscopic scales, many of which will be addressed in this thesis.

Before leaving this introduction to aqueous Laponite® dispersions, it is necessary to point out that one of the important motivations for fundamental studies of their rheology is that they serve as models for a class of materials called *soft glassy materials*. A theoretical model for such materials, called the 'soft glassy rheology' (SGR) model, was recently developed to describe rheological aging and shear rejuvenation phenomena [60, 61, 62]. The model characterizes the continual slowing down of microstructural rearrangements, as well as local rejuvenation due to shear or thermal energy, using an 'effective noise temperature'. Because Laponite® is a well-defined synthetic material that exhibits aging and shear rejuvenation in aqueous dispersions, a number of studies have explored Laponite® clays with the goal of understanding soft glassy materials in general [36, 63]. Though further discussion of the SGR model is beyond the scope of this thesis, introductions to soft glassy materials and the SGR model can be found in [60, 61], and a more thorough description is given in [62].

Further discussion of the current understanding of Laponite® phase behavior, microstructure, and rheology can be found in Section 2.2. Also, interested readers are directed to a thorough review by Ruzicka and Zaccarelli [43].

1.4 Magnetorheological Fluids

After characterizing the bulk and micro-scale rheology of aqueous Laponite® dispersions, we explore their application as matrix fluids in magnetorheoligcal (MR) suspensions in Chapter 4. This study takes advantage of the yield stress behavior of aqueous Laponite® dispersions to prevent sedimentation of magnetic particles and maintain a stable suspension. Relevant aspects of MR fluids are introduced below.

MR fluids are field-responsive materials that exhibit fast, dramatic, and reversible changes

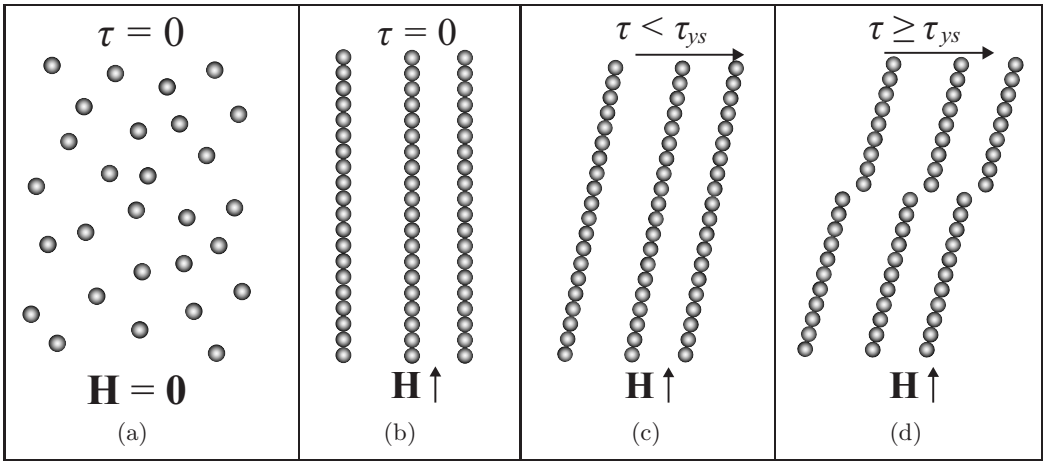

Fig. 1.8: *Basic microstructure of MR suspensions in a uniform applied magnetic field,* **H** *[72]. (a) Particles disperse randomly at* $\mathbf{H} = 0$*. (b) When a magnetic field is applied, chains form and align with the field. (c) Chains deforming in response to a shear stress,* τ*. (d) Chains rupture when the applied stress exceeds the field-induced static yield stress,* $\tau \geq \tau_{ys}$*, and the sample flows.*

in properties when subjected to a magnetic field. They consist of a suspension of microscopic magnetizable particles in a non-magnetic matrix fluid. The particles attract each other and align when an external magnetic field is applied, resulting in the formation of domain-spanning chains of particles [2]. This field-induced structuring of the suspension leads to significant changes in rheological properties, including order-of-magnitude growth in the steady-shear viscosity and the emergence of field-dependent yield stress and viscoelastic behavior [64]. The tunability of rheological properties with the applied magnetic field provides the basis for a wide variety of commercial applications of MR fluids, including automobile clutches [65], active mechanical dampers [66], seismic vibration control [67], prosthetics [68], precision polishing [69], and drilling fluids [70] (for a review of applications, see [71]).

Starting with Rabinow in 1948 [65], a large number of studies have probed the bulk rheology, microstructure, dynamics, and applications of MR fluids as well as analogous electrorheological (ER) fluids [72]. The most prominent rheological feature of these fluids is a field-induced and field-dependent yield stress caused by the alignment of magnetizable particles into domain-spanning chains that must be ruptured for the sample to flow. This basic behavior is shown schematically in Fig. 1.8. The critical stress necessary to rupture activated chains from rest and cause bulk flow, τ_{ys}, corresponds to the bulk field-induced *static* yield stress (as opposed to the field-induced *dynamic* yield stress, which is discussed below).

Most MR fluid formulations use carbonyl iron powder (CIP) or similar ferromagnetic microparticles as the dispersed phase because of their large saturation magnetization $M_{sat} \sim 200$ emu/g [71, 64]. CIP particles develop a dipole moment in an external magnetic field and exhibit negligible magnetic hysteresis. Further information about the CIP particles used to formulate MR fluids in this thesis, including size distribution and magnetization data, can be found in Section 4.3.1 and

Table 1.1: *Typical parameters for MR fluids in commercial applications.*

Particle diameter	1–10 μm, [71]
Vol. % of magnetic particles	20–40 v% [73]
Applied magnetic flux density, $\mathbf{B}$	$\sim$ 1 Tesla [71]
Magnetic susceptibility, χ	$\sim$ 10 [74]
Saturation Magnetization, M_{sat}	$\sim$ 200 emu/g = 200 A·m^2/kg [74]
Max induced yield stress	$\sim$ 100 kPa typically, but up to 800 kPa in specialized apparatus [75]

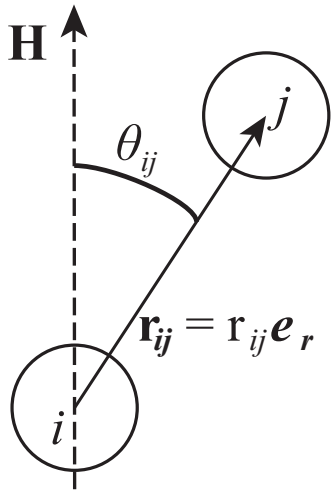

Fig. 1.9: *Magnetizable particles subject to an applied magnetic field,* $\mathbf{H}$*. Image from [76].*

Fig. 4.1. Some typical characteristics of MR fluids in commercial settings are given in Table 1.1.

When a uniform external magnetic field is applied to an MR suspension, a dipole moment $\mathbf{m}$ is induced in each of the dispersed particles [77]. Treating the particles as identical point dipoles and assuming negligible magnetic induction, the particles interact via the pairwise potential, U_{ij} [76],

$$U_{ij} = \frac{m^2 \mu_0}{4\pi} \left(\frac{1 - 3\cos^2 \theta_{ij}}{r_{ij}^3} \right) \qquad m = \|\mathbf{m}\| \tag{1.11}$$

where μ_0 is the magnetic permeability of free space (usually very close to the magnetic permeability of the medium in MR fluids), r_{ij} is the separation distance between the particles, and θ_{ij} is the angle that the line connecting the particle centers makes with the direction of the applied magnetic field, as in Fig. 1.9 (Image from [76]). Equation 1.11 shows that the energy is minimized when $\theta_{ij} = 0$ and r_{ij} is minimum, corresponding to a particle chain aligned with the external magnetic field $\mathbf{H}$. Typically, this chaining occurs over a time scale of $\sim$1–10 ms [78], though generally the microstructure formation is governed by an interplay between magnetic, viscous, thermal, and

buoyancy effects, as well as any non-Newtonian rheological properties of the matrix fluid. The depth of the energy well, which is related to the applied stress necessary to rupture chains, is proportional to m^2. This implies a simple approximate scaling relationship between the field-induced static yield stress, τ_{ys}, and the particle magnetization per unit mass, M.

$$\tau_{ys} \sim m^2 \sim M^2 \tag{1.12}$$

Here we have used the fact that $m = V\rho M$, where V is the volume of a particle and ρ is the particle mass density.

In addition to the dipolar stress between particles, other relevant stresses in MR suspensions may arise from viscous, thermal, and buoyancy effects. If the matrix fluid exhibits a yield stress, $\tau_{ys,0}$, it may also play a significant role in the behavior of dispersed magnetic particles. Table 1.2 presents a number of key dimensionless groups comparing the magnitudes of these stresses. In general, significant field-induced chaining occurs if the characteristic magnetic dipolar stress is large enough to overcome all other stresses on particles (i.e., if Mn $\ll 1$ and λ, $\mathrm{Y}^*_{\mathrm{M},\phi} \gg 1$). Particularly important for the purpose of this thesis is the *Magnetic Yield Parameter*, $\mathrm{Y}^*_{\mathrm{M},\phi}$, which reflects the competition between magnetic dipolar forces and the matrix fluid yield stress. The definition of this parameter in Table 1.2 incorporates the effect of particle volume fraction, ϕ, which is not included in previous definitions [79]. This dimensionless group will be further discussed in Chapters 4 and 5. For the definitions of the dimensionless groups in Table 1.2, it is assumed that the magnetic permeability of the matrix fluid is approximately equal to the permeability of free space, μ_0.

Particle chaining in commercial MR fluids occurs on a time scale of ~ 1 ms [78]. In the absence of Brownian motion, the time scale for chaining can be approximated as the time necessary for a particle to move its own diameter in response to magnetic forces. We will show in Chapter 5 that this time scale for chaining is approximately

$$t_{chain} = \frac{48\zeta}{\pi a \mu_0 \rho^2 M^2} \tag{1.13}$$

where $\zeta = 6\pi\eta_c a$ is the drag coefficient and the other parameters are defined in Table 1.2. Lateral aggregation of chains into clusters has been observed at longer time scales [81]. This phenomena occurs through a 'zippering' mechanism in which two chains approach in an attractive configuration and become inter-digitated [82]. For Brownian chains, Fermigier and Gast proposed the following expression for the time scale of lateral aggregation [81]:

$$t_{lat} \sim \frac{\sqrt{\lambda}}{\phi^{2/3}} \frac{\pi \eta_c a^3}{k_B T \phi} \tag{1.14}$$

Depending on the system parameters, this time scale is often $\sim$ 1–100 s. We are unaware of any report of the lateral aggregation time scale when only magnetic forces are present (i.e., no thermal forces or bulk flow).

In the vast majority of work on MR fluids, magnetizable particles are suspended in a Newtonian matrix fluid; however, due to the typically large density difference between the iron-containing magnetizable particles and the matrix fluid, particle sedimentation is often problematic. In terms of the dimensionless groups defined above, $\mathrm{Y_G} \to 0$ in Newtonian matrix fluids. Yield stress matrix fluids have been proposed to address this issue [79], but the few studies in which they are used focus on

Table 1.2: *Important dimensionless groups in magnetorheology [76, 79, 80].*

Parameter		**Stresses**	**Definition**	**Comments**
Mason Number	Mn	$\frac{viscous}{magnetic}$	$\frac{9\eta\dot{\gamma}\phi^2}{2\mu_0\rho^2M^2}$	**Particle chains occur if** $\mathrm{Mn} \ll 1$ η = viscosity of continuous phase $\dot{\gamma}$ = macroscopic shear rate ϕ = volume fraction of magnetic particles μ_0 = magnetic permeability of free space ρ = particle mass density M = particle mass magnetization
Magnetic Thermal Parameter	λ	$\frac{magnetic}{thermal}$	$\frac{\pi\mu_0 a^3\rho^2M^2}{9k_BT}$	$\lambda \gg 1$ **for MR fluids** a = particle radius k_B = Boltzmann constant T = temperature
Magnetic Yield Parameter	$\mathrm{Y}^*_{\mathrm{M},\phi}$	$\frac{magnetic}{yield\ stress}$	$\frac{\mu_0(\rho M)^2\phi^{4/3}}{24\tau_{ys,0}}$	**Particle chains occur if** $\mathrm{Y}^*_{\mathrm{M},\phi} \gg 1$ $\tau_{ys,0}$ = matrix fluid yield stress
Gravity Yield Parameter	$\mathrm{Y_G}$	$\frac{yield\ stress}{buoyancy}$	$\frac{3\tau_{ys,0}}{a(\rho-\rho_c)g}$	**Sedimentation occurs if** $\mathrm{Y_G} \lesssim 1$ ρ_c = density of continuous phase g = acceleration of gravity
Induced Yield Parameter	$\mathrm{Y_{ind}}$	$\frac{induced\ yield\ stress}{zero\text{-}field\ yield\ stress}$	$\frac{\tau_{ys}}{\tau_{ys,0}}$	$\mathrm{Y_{ind}} \gg 1$ **in most applications** τ_{ys} = field-induced yield stress $\tau_{ys,0} \approx$ yield stress at zero-field

the bulk rheology of the suspension and provide no quantitative investigation of the microstructure [79, 83, 84, 85]. Additionally, previous studies of MR suspensions in yield stress matrix fluids have measured only the field-induced *dynamic* yield stress. The field-induced *static* yield stress, however, is also an important property in many MR fluid applications and is a more direct measure of the 'strength' of an MR fluid [86]. The dynamic yield stress is typically measured by imposing a set of decreasing steady-state shear rates, $\dot{\gamma}$, and extrapolating the resulting shear stresses to $\dot{\gamma} = 0\ \mathrm{s}^{-1}$. In contrast, the static yield stress is defined as the stress required to induce flow from rest [17]. For MR suspensions in a matrix fluid that requires a finite time to re-form microstructure after being sheared (as is the case for aqueous Laponite® dispersions), it is unclear *a prioiri* whether these two yield stress measures will agree when a magnetic field is applied. Because of the many applications in which yield stress matrix fluids could prove beneficial in preventing particle sedimentation in MR fluids, it is important to characterize the field-induced static yield stress in MR suspensions stabilized by yield stress matrix fluids. Additionally, a fundamental understanding of the effect of a matrix fluid yield stress on the evolution of the microstructure in these field-responsive suspensions would be extremely helpful when developing rheological constitutive equations for use in engineering design.

The dimensionless groups given in Table 1.2 are helpful in relating the work in this thesis on yield-stress stabilized MR fluids to previous studies and existing technology. Fig. 1.10 shows parametric maps of $[\mathrm{Y_G}, \lambda]$ and $\left[\mathrm{Y_G}, \mathrm{Y}^*_{\mathrm{M},\phi}\right]$ with regimes for various magnetic fluid phenomena.

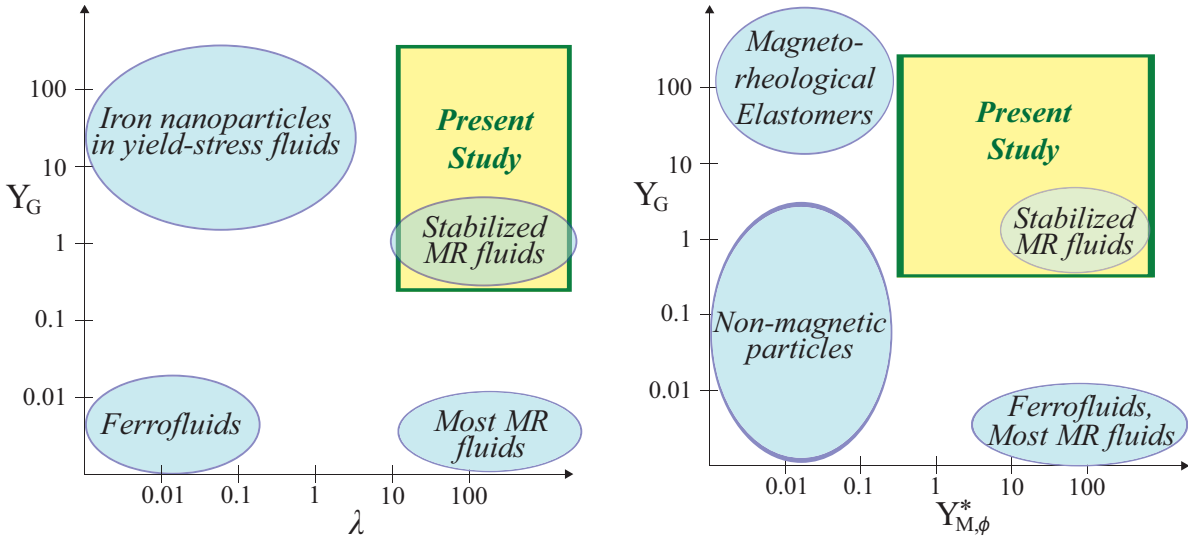

Fig. 1.10: *Parameter space maps comparing the relative magnitudes of different forces in various magnetic fluid formulations using the dimensionless groups defined in Table 1.2 [12, 76, 79, 87, 88]. The present study examines gravitationally stable MR suspensions* ($Y_G \gtrsim 1$, $\lambda \gg 1$) *in yield stress matrix fluids. Regimes are explored in which inter-particle magnetic forces dominate over the matrix fluid yield stress* ($Y^*_{M,\phi} \gg 1$) *and in which magnetic forces approximately balance the matrix fluid yield stress* ($Y^*_{M,\phi} \sim 1$). *Note that applications for iron nanoparticles in yield-stress fluids have not yet been found.*

In ferrofluids, thermal energy maintains dispersion of iron nanoparticles in a Newtonian fluid, so they lie in a regime where $\mathrm{Y_G}, \lambda \ll 1$ and $\mathrm{Y^*_{M,\phi}} \gg 1$ [87]. Applications for iron nanoparticles in yield stress fluids, which are in the top-left corner of the $[\mathrm{Y_G}, \lambda]$ map, have yet to be found. The MR fluid regimes correspond to $\lambda \gg 1$ and $\mathrm{Y^*_{M,\phi}} \gg 1$, and since most MR suspensions use Newtonian solvents, $\mathrm{Y_G} \approx 0$ in most cases, with $\mathrm{Y_G} \gtrsim 1$ for the few yield stress-stabilized MR fluid studies published to date [79, 76]. Since the work in this thesis involves MR suspensions in aqueous Laponite® dispersions, which exhibit time- and concentration-dependent yield stresses, a span of $\mathrm{Y_G}$ and $\mathrm{Y^*_{M,\phi}}$ values will be explored. In particular, we examine regimes from $\mathrm{Y^*_{M,\phi}} \gg 1$, where inter-particle magnetic forces are expected to dominate over the matrix fluid yield stress, to $\mathrm{Y^*_{M,\phi}} \sim 1$, where magnetic forces are approximately in balance with the matrix fluid yield stress. The regime where $\mathrm{Y^*_{M,\phi}} \gg 1$ and $\mathrm{Y_G} \gtrsim 1$ is important for MR suspensions that are resistant to sedimentation. While not practical for traditional MR fluids, the regime wher $\mathrm{Y^*_{M,\phi}} \sim 1$ has yet to be explored. It is possible that new technologies or applications could take advantage of the unique microstructure observed in this regime where the matrix fluid yield stress has significant influence over the growth of dipolar chains (see Chapter 5).

Additional information about existing approaches to preventing sedimentation in MR suspensions, as well as details of the particular setup and protocol for magnetorheology experiments in

this thesis, can be found in Chapter 4. For a review of recent progress on other aspects of MR fluid research and technology, see [64].

1.5 Thesis Objectives

The first goal of this research is to combine bulk rheology and microrheology experiments to obtain an improved understanding of the flow behavior and microstructure of aqueous Laponite® dispersions. Secondly, we aim to determine the effect of the visco-elasto-plasticity and aging behavior of aqueous Laponite® dispersions on the magnetorheology and microstructure of field-activated suspensions of dipolar particles. To this end, the following specific projects are described:

- Gelation of dilute aqueous Laponite® dispersions using linear bulk rheology and Multiple Particle Tracking microrheology with a range of probe sizes (Chapter 2). (Rich *et al.*, *J. Rheol.*, 2011) [89];
- Nonlinear rheology (shear-thinning and yielding) of more concentrated aqueous Laponite® dispersions using bulk measurements and a fully-characterized magnetic tweezer microrheology technique (Chapter 3). (Rich *et al.*, *Soft Matter*, 2011) [90];
- Magnetorheology in an aging, yield stress matrix fluid composed of an aqueous Laponite® dispersion (Chapter 4). (Rich *et al.*, submitted to *Rheol. Acta*, 2011) [91];
- Particle-level simulations of field-activated dipolar particle assembly in a yield stress matrix fluid (Chapter 5). (Rich *et al.*, submitted to *Langmuir*, 2011) [92];

1.6 Overview of Results

In Chapter 2, we examine the linear viscoelasticity of 1 w% aqueous Laponite® dispersions during gelation using bulk rheology and Multiple Particle Tracking microrheology. We find order-of-magnitude differences between rheological properties and gelation times measured at the different length scales. Further, we find that microrheology results are highly dependent on probe size, indicating that the microstructure and rheology are highly length-scale–dependent. We hypothesize that this behavior is due to a porous, heterogeneous network structure having characteristic length scales (i.e., pore size, aggregate size, etc) on the order of the probe sizes. This hypothesis is supported by direct measurements of the spatial heterogeneity of probe dynamics and qualitative features of probe trajectories.

In Chapter 3, the nonlinear rheology of more concentrated aqueous dispersions of Laponite® is examined and compared at bulk and microscopic length scales. Through collaboration with Professor Jan Lammerding of Harvard Medical School and Brigham and Women's Hospital (currently at Cornell University), a magnetic tweezer device was obtained and characterized in terms of the accessible stresses, the applied magnetic fields, and the measurable viscosities and shear rates. Stresses up to about 250 Pa are achieved on 4.5 μm diameter superparamagnetic probe particles. We demonstrate the first use of magnetic tweezers to measure yield stresses on the microscopic scale, as well as the first comparison between bulk and micro-scale yield stress measurements. For Laponite® concentrations greater than or equal to 2.0 w%, we find that bulk and micro-scale yield

stress measurements are in quantitative agreement, both exhibiting an approximately logarithmic dependence on the age time.

Chapter 4 describes measurements of the magnetorheology of MR suspensions in matrix fluids composed of aqueous dispersions of Laponite®. While the sedimentation of the magnetic particles is prevented essentially indefinitely by the yield stress of the Laponite® matrix fluid, results indicate that aging and yield stress properties of the matrix fluid have negligible effect on the magnetorheological properties as long as a sufficient magnetic field is applied. These observations are explained in terms of the magnetic yield parameter, $\mathrm{Y}^{*}_{\mathrm{M},\phi}$, defined in Table 1.2. For $\mathrm{Y}^{*}_{\mathrm{M},\phi} \gtrsim 10$, the field-induced dynamic and static yield stresses are found to be in good agreement, and aging effects of the matrix fluid can be safely neglected. The effects of the magnetic field strength and the magnetic particle concentration are synthesized in a master curve relating the field-induced yield stress to the particle magnetization, amounting to a concentration–magnetization superposition.

In Chapter 5, particle-level simulations are used to examine the microstructure of dipolar particles assembling in a yield stress matrix fluid. The competition between the yield stress and inter-particle magnetic stresses is again characterized in terms of a magnetic yield parameter similar to that in Table 1.2. We find that the yield stress results in an arrest of chain growth, so that the length of particle chains at equilibrium decreases as the matrix fluid yield stress increases relative to the inter-particle magnetic stresses. Additionally, the lateral 'zippering' mode of aggregation observed in Newtonian fluids is suppressed by the presence of the yield stress. For sufficiently high yield stresses (i.e., magnetic yield parameters ≤ 1) structure formation is almost entirely arrested and individual immobile particles dominate. These results are discussed in the general context of particle assembly, highlighting the potential for yield stress matrix fluids to aid in the assembly of various kinds of complex functional materials.

Conclusions and an outlook to future work are summarized in Chapter 6. The appendix provides details about particular calculations used to understand the MPT microrheology results in Chapter 2.

CHAPTER 2

Particle Tracking Microheology of Aqueous Laponite Dispersions

This chapter begins our examination of the rheology of aqueous Laponite® dispersions at bulk and microscopic length scales. Here we focus on the dependence of microrheological properties on probe size during gelation, exploring detailed aspects of the probe trajectories and various statistics of the diffusion behavior to gain insight into the dispersion microstructure. The results presented in this chapter can be found in the following publication [89]: Rich, J. P.; McKinley, G. H.; Doyle, P. S. *J. Rheol.* **2011**, *55*, 273–279, copyright 2011 by The Society of Rheology.

2.1 Overview

Soft materials such as gels and colloidal glasses often exhibit different rheological properties at bulk and microscopic scales as a result of their complex microstructure. This phenomena has recently been demonstrated for a gel-forming aqueous dispersion of Laponite® clay by Oppong *et al.* [59]. For this material, microrheology reveals a significantly weaker gel and a longer gelation time than bulk measurements. By performing multiple particle tracking microrheology experiments with different probe sizes, it can be shown that length-scale–dependent rheology is a general feature of Laponite® gels. Small changes in probe size are accompanied by order of magnitude differences in the observed rheological properties and gelation time. The probe dynamics also exhibit

size-dependent spatial heterogeneities that help to elucidate a microstructural length scale in the system. Through analytical theory and Brownian dynamics simulations, it can be shown that the correlations described by previous authors between successive displacements of individual probes are more directly a result of material elasticity than of microstructural confinement. The apparent gelation times of dispersions with different Laponite® concentrations exhibit a self-similar dependence on probe size, suggesting a superposition of Laponite® concentration and probe size. From these observations, an accordant description of the microstructural evolution of the gel is proposed.

2.2 Introduction

Colloidal gels are an important class of soft materials that are found throughout nature and used in many industrial applications. They typically consist of a suspension of colloidal particles that undergoes dynamical arrest through the formation of an interconnected fractal-like network [93]. This process, called gelation, can occur via equilibrium or non-equilibrium routes [94] and results in a soft viscoelastic solid called a gel state [2]. Though suspended particles are often spherical and uncharged, anisotropic charged particles like discotic colloidal clays are common in nature and are used as rheological modifiers in many applications, such as paints, drilling fluids, consumer products, and cosmetics [95]. Dispersions of discotic colloidal clays are attractive for applications because of their ability to form various types of arrested states with rich rheological behavior even at low clay concentrations (around 1 wt%) [41].

In this chapter we investigate the gelation and rheological aging of aqueous dispersions of the synthetic clay Laponite RD® (Rockwood Additives, Gonzales, TX) by tracking the thermally driven motion of embedded microscopic probe particles [24, 21, 96, 97]. Individual Laponite® crystals consist of colloidal disklike particles about 30 nm in diameter and 1 nm in thickness (see Fig. 1.5), with a reduced molecular formula of $[Na_{0.7}]^{+0.7}[(Si_8Mg_{5.5}Li_{0.3})O_{20}(OH)_4]^{-0.7}$ [44]. The disk geometry and size have been verified by small angle X-ray scattering (SAXS) measurements [45, 46]. Due to the molecular structure of the Laponite® clay, platelets in aqueous dispersions exhibit a negative charge on each face and for pH less than about 11, appear to be positively charged along the rim [44]. Previous reports have indicated the necessity of the resulting face-to-rim attractions for inducing aggregation and gelation [48, 49]. Attractive and repulsive surface charge interactions can be tuned by adjusting the ionic strength I in the solution, which affects the extent of the electrical double layer [93]. Therefore, ionic strength strongly influences the nature and kinetics of structural arrest as well as the dispersion mechanical properties [45, 98, 47].

2.2.1 Phase Behavior and Microstructure of Aqueous Laponite® Dispersions

When Laponite® is dispersed in water, the system evolves over time from a liquidlike state to a nonergodic disordered arrested state. During this process, known generally as aging, the mechanical properties of the material change over time as the microstructure develops. Aging in Laponite® dispersions has been studied by a number of authors using dynamic light scattering (DLS), in which the transition from a liquid to an arrested state is typically monitored by analyzing the growth over time of a non-ergodicity parameter [99]. Though the physical mechanism of the aging process and the nature of the nonergodic states that develop have been the subject of much debate, the current status of DLS studies of aging in Laponite® dispersions is well-summarized by Jabbari-Farouji *et al* [100] (see also the recent review by Ruzicka and Zaccarelli [43]). Here the authors also present a state

diagram obtained from DLS measurements that attempts to unify the long age time observations of previous studies (a similar updated diagram from [43] is shown in 1.7). Different nonergodic states are identified that correspond to regions in the (ionic strength)-(Laponite® concentration) state diagram: gel, repulsive 'Wigner' glass, and a so-called 'attractive glass' or 'cluster glass' [101]. Generally, high values of I result in the screening of repulsive charge interactions between platelets, leading to the dominance of attractive interactions and the emergence of a gel or attractive glass state for Laponite® concentrations greater than or equal to about 0.5 wt% [see also Ruzicka *et al.* [102]]. For $I > 10$ mM, repulsive interactions are screened to the extent that bulk phase separation via flocculation occurs [45, 102]. At low I, long-range repulsive interactions dominate, leading to a repulsive colloidal glass, even for Laponite® concentrations as low as about 1 wt%. In this thesis, a relatively high ionic strength is used ($I = 5.9$ mM). Further, this chapter describes studies of dispersions at low Laponite® concentration (~ 1 wt%). For this set of parameters, it is expected that attractive interactions will dominate, resulting in either a gel or an attractive glass state. Since an attractive glass shares many structural and mechanical features with a gel, including spatial heterogeneity [100], the terminology of gelation shall be emploed in the analysis. While it is possible that some of the samples might be more accurately characterized as 'attractive glasses' in the arrested state, the DLS observations of [100] imply that such a distinction would have negligible effect on results and analysis, and that the two states would be essentially indistinguishable from a microrheological perspective.

By combining small-angle x-ray and neutron scattering with static light scattering, Pignon *et al.* [103] studied the physical structure of Laponite® dispersions in the gel state, obtaining the scattering curve over 5 orders of magnitude in length scale. Their results indicate that there are two scales of fractal organization. On length scales ranging from about a few clay platelets to about 1 μm, aggregates form that exhibit spatial variations in Laponite® density ('micro-domains' separated by 'voids'). These aggregates are themselves loosely connected in a fractal network, with clusters of aggregates exhibiting sizes up to about 5 μm. Beyond this length scale the dispersion appears homogeneous. Their observations also indicate that the characteristic sizes of aggregates and clusters, as well as their densities and fractal dimensions, are dependent on the Laponite® concentration and the ionic strength [104].

2.2.2 Rheology of Aqueous Laponite® Dispersions

Motivated by applications of Laponite® and other colloidal clays as rheological modifiers, the aging process in Laponite® dispersions has also been studied using rheology experiments. This work has also been driven by the fact that Laponite® dispersions serve as model soft thixotropic materials. As the system ages and develops structure, the viscosity of the dispersion increases by orders of magnitude and a yield stress emerges, also increasing over time. Early work on Laponite® rheology was performed by [105] who observed that at long age times, both the storage modulus G' and the yield stress of the dispersion increase strongly with Laponite® concentration. At a given age time and Laponite® concentration, Mourchid *et al.* [98] observed that the linear viscoelastic moduli increase with ionic strength up to the point at which bulk phase separation occurs via flocculation. They also found that the bulk storage modulus G' is nearly independent of frequency at long age times, a result confirmed by Ewoldt *et al.* [35], who explored the use of an aqueous Laponite® dispersion as a simulant for a mucin gel in robotic mechanical crawlers. In this article, the steady shear viscosity was reported to decrease sharply when the applied stress exceeds the yield stress.

Cocard *et al.* [106] studied the age time and frequency dependence of the linear viscoelastic moduli at low Laponite® concentration and moderate ionic strength, observing growth in both G' and G'' over time and an approximate power-law frequency dependence. These results are consistent with the formation of a self-similar network structure (i.e., a gel), and the gelation time t_{gel} is defined as the time at which the power law exponents for the frequency dependence of G' and G'' are equal [9]. Bonn *et al.* [36] attempted to fit the rheological behavior of Laponite® dispersions in the repulsive glass state to the 'soft glassy rheology' (SGR) model [60, 61, 62]. Their findings indicate good agreement in the linear viscoelastic regime. The model also correctly predicts qualitative features of shear-thinning and shear rejuvenation, which refers to the reduction in relaxation time that occurs when shearing motion breaks apart the dispersion microstructure [37]. The competition between aging and shear rejuvenation at a constant shear rate, a feature of the SGR model, was demonstrated in glass-forming Laponite® dispersions by Abou *et al.* [107]. Some deviations from the SGR model were observed at large strains, however, due to shear banding and a viscosity bifurcation, in which the viscosity grows indefinitely at low applied shear stress but remains orders of magnitude lower when a critical shear stress is exceeded [36]. The SGR model has recently been extended to capture these effects [108].

In this chapter, the method of multiple particle tracking (MPT) is used to study the rheological properties of aqueous Laponite® dispersions at the microscopic scale. As with most microrheology techniques, MPT relates the motion of embedded microscopic probe particles to the rheology of the surrounding fluid [20]. In the case of MPT, probe motion is driven solely by Brownian bombardment, with many probes (~ 100) being simultaneously visualized via video fluorescence microscopy [24]. Due to the small Brownian stress acting on the probe particles (usually 0.01–1 Pa), and the limited spatial resolution of optical microscopes, MPT is best suited for fluids with moduli ≤ 1 Pa [21]. Software has been developed by Crocker and Grier [26] for extracting trajectories from movies of diffusing probe particles, allowing the calculation of the ensemble average mean squared displacement as a function of lag time. This quantity can be related to the linear viscoelastic moduli $G'(\omega)$ and $G'(\omega)$ by a generalized Stokes–Einstein relation [96, 97, 109]. If the probes are much larger than any characteristic microstructural length scale in the fluid, then microrheological results will match those on the bulk scale. If, however, there are microstructural length scales on the order of the probe size (as is the case in Laponite® dispersions for probes smaller than about 5 μm [103]), then the results will reflect the mechanical properties of the material on that length scale and will generally not match bulk measurements [22]. Because individual probe trajectories are available, analysis is not limited to ensemble averages. In particular, significant insight can be gained into the local microenvironments of individual probe particles [110], although Levine and Lubensky [23] have shown using a two-fluid model that local dynamics cannot be completely decoupled from fluid properties farther from probes. A number of industrially and biologically relevant gel-forming materials have been studied recently with MPT including Carbopol gels [111], gellan gum [112], oligopeptide dispersions [113, 114], and hectorite clay dispersions [115].

Despite considerable interest in the bulk rheology and phase behavior of Laponite® dispersions, there have been relatively few studies of the rheology on the microscopic scale. Jabbari-Farouji *et al.* [57] used an optical tweezer setup to validate the fluctuation-dissipation theorem in an aging Laponite® dispersion by comparing results from passive and active microrheology experiments. In a subsequent publication, the thermal fluctuations of embedded probe particles in an optical trap were monitored in both gel-forming and glass-forming dispersions [58]. From a microrheological perspective, the aging behavior of the two types of dispersions was found to be similar, though

an examination of particles at various positions revealed differences in the spatial distribution of probe dynamics. Dispersions in the glass state exhibited spatially homogeneous microrheology that matched bulk rheology measurements, while significant heterogeneity and discrepancies with bulk results were observed in the gel state. Using MPT, Oppong *et al.*[59] performed a more detailed comparison of the rheology at bulk and microscopic scales during the gelation process, confirming the discrepancies and the spatial heterogeneities reported by Jabbari-Farouji *et al.* [58]. Additionally, these authors found that as the system ages, probes exhibit correlations between successive displacements, which were reported to result from microstructural confinement.

The results of Oppong *et al.*[59] imply that the local rheology and gelation properties of the dispersion, and therefore the nature of the probe dynamics, may generally depend on the length scale that is probed: that is, the rheology may be probe-size-dependent. DLS observations by Strachan*et al.*[116] of probe-size-dependent diffusive behavior in the repulsive glass state support this notion. Measurements of the average diffusivity of various sized particles by Petit*et al.*[117] using fluorescence recovery after photobleaching (FRAP) are also consistent with this hypothesis. FRAP results were interpreted in terms of a scale-dependent effective viscosity that increases with probe size.

In this chapter, MPT is used to study the gelation of aqueous Laponite® dispersions at the microscopic scale, expanding on the comparisons of bulk and micro-scale rheology made by Oppong*et al.*[59] to explore the probe-size dependence of the microrheology. Based on our observations at different length scales, we propose a description of the microstructural evolution with age time and check the consistency of this scenario with measurements of the heterogeneity of probe dynamics for various probe sizes. Further, by examining correlations between successive probe displacements, evidence is found of a microstructural length scale in the system, though the interpretation of correlations as necessarily a result of microstructural confinement is challenged. Motivated by the probe-size dependence of the microrheological observations, in the final section a common scaling is proposed for the gelation time that collapses data at different Laponite® concentrations and probe sizes.

2.3 Materials and Methods

2.3.1 Sample Preparation

Laponite RD® powder was obtained from Rockwood Additives. To prepare the clay dispersion, dry Laponite® powder is added to an aqueous buffer of pH ≈ 10 consisting of 1.8 mM NaOH and 4.1 mM $NaHCO_3$. The purpose of the buffer is to avoid the dissolution of Laponite® platelets, which has been observed at lower pH [50], and to fix the solvent ionic strength at $I = 5.9$ mM. The dispersion is kept under N_2 gas in order to prevent the uptake of CO_2, which would lower the solution pH and contribute to the dissociation of platelets [45, 51, 48]. After mixing vigorously for at least 1.5 hours, the clay dispersion is passed through a 0.8 μm filter, breaking apart most of the remaining aggregates with a strong shear [53]. This filtration marks the point of zero age time t_w, in accordance with previous work on Laponite® dispersions [39], and structuring of the clay begins thereafter as the system ages. Petit *et al.* [117] demonstrated that about 7% of the initial Laponite® concentration is lost when dispersions of about 3 wt% Laponite® are passed through 0.45 μm filters. However, since the present study uses filters with larger pores (0.8 μm) and dispersions of lower concentration (presumably reducing the size of aggregates), it is assumed

that filtration does not change the nominal concentration of Laponite®.

2.3.2 Multiple Particle Tracking

Immediately following filtering, fluorescent microparticles (Fluoresbrite® Yellow Green (YG) Carboxylate Microspheres from Polysciences, Inc.) are added to a concentration of about $\phi \sim$ 0.01 vol%, or about 100 particles per microscope view frame depending on the particle size. The fluorescent particle concentration is chosen to achieve a large number of individual particle trajectories with approximately non-interacting particles. After vortex mixing for about 15 seconds, the fluorescent particles are randomly dispersed in the sample. The additional rejuvenation of the sample due to vortex mixing is minimal since it is conducted immediately after filtering.

It is important to consider the electrostatic and van der Waals interactions between probes and Laponite® particles, which could affect microrheological measurements [118]. Fluoresbrite® YG Carboxylate Microspheres were shown to be negatively charged in aqueous solutions close to the pH used in the present work, with a zeta potential of about −40 mV [119]. Additionally, Laponite® particles exhibit surface charges of about $-700e$ per particle in aqueous solution, where e is the elementary charge [48]. In order to determine the significance of probe–clay colloidal interactions, solution microcalorimetry measurements were performed using an Isothermal Titration Calorimeter (Nano ITC from TA Instruments) [120]. When titrating a probe dispersion of 0.004 vol% (probe radius a = 0.161 μm) into 0.04 vol% Laponite®, the probe–clay interaction energy was found to be about 35 mJ/g of Laponite®: less than the Laponite® dilution enthalpy into buffer at the same concentration (200 mJ/g of Laponite®) and below the reliable resolution of the instrument. This result implies that such interactions can be safely neglected.

After incorporating the probe particles, the dispersion is sealed in a sample chamber consisting of two cover slips separated by 250 μm thick spacers and mounted on a microscope (Carl Zeiss Optical, Axiovert 40 CFL). Experiments are performed at room temperature, $T \approx 23 \pm 0.5$ °C. A 63× water-immersion objective (N.A. = 1.2) is used for all particle sizes except the largest particles, with radius $a = 1.040$ μm, for which a 20× objective (N.A. = 0.5) is used. An HBO 100 Mercury lamp (Carl Zeiss Optical), with an HBO 103 bulb (Osram) and an XF130-2 filter set (Omega Optical), is used to excite the particles and isolate their fluorescent emission (see Fig. 1.2 for a schematic of the fluorescence microscopy setup). Movies of particle dynamics are captured with a CCD camera (Hitachi KP-M1A) having a variable shutter speed between 1/60 s and 1/10,000 s set to frame integration mode. Scion Image software is used to record movies at a rate of 30 frames/s over the span of one minute. Each video frame consists of two interlaced fields (the odd or even rows of the CCD matrix) that are exposed 1/60 s apart, requiring each frame to be de-interlaced during the movie analysis. The interlacing also results in a loss of resolution in the spatial direction perpendicular to the interlacing [26]; thus, particle displacements in this study are only analyzed in the horizontal direction (the x-direction). Movies of probe particle diffusion are analyzed to obtain particle trajectories using publically available software developed by Crocker and Grier [26] (see `http://www.physics.emory.edu/~weeks/idl/`, 'Particle Tracking Using IDL', site maintained by Eric Weeks). Typical probe particle trajectories in 1 wt% Laponite® at various dispersion age times are shown in Fig. 2.1(a), from which the decreased mobility of the particles with age is immediately apparent. The most fundamental quantitative result extracted from probe

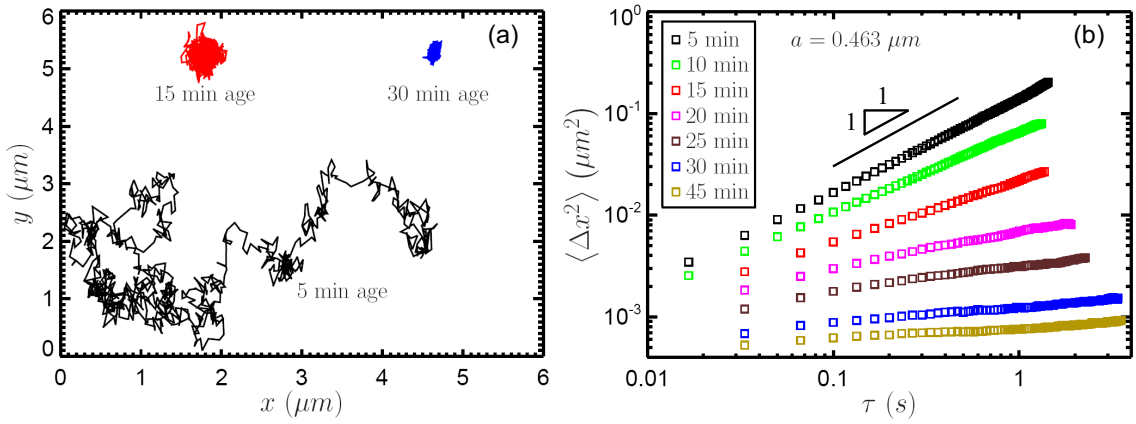

Fig. 2.1: *(a) Typical trajectories of fluorescent probe particles with radius* $a = 0.463$ *μm in 1 wt% Laponite® at various age times. Though particles exhibit diffusive motion at early age times, trajectories become increasingly localized as the dispersion ages. At late age times, probe particles fluctuate around a fixed central position. (b) The most fundamental quantitative result of multiple particle tracking is the mean-squared displacement as a function of lag time* τ*, shown here for various age times of a 1 w% Laponite® dispersion and a probe radius of* $a = 0.463$ *μm. At early age times, the probe motion is approximately diffusive and the logarithmic slope is close to 1. As the dispersion ages, the logarithmic slope decreases, and a plateau that is characteristic of a gel is eventually apparent at long lag times.*

trajectories is the mean-squared displacement (MSD).

$$\left\langle \Delta x^2 (\tau) \right\rangle = \langle x (t+\tau) - x (t) \rangle \tag{2.1}$$

The mean-squared displacement is a function of the lag time τ, which is the time step over which displacement due to particle diffusion is measured. If the MSD data is smoothly varying, it can generally be fit to a local power law [97],

$$\left\langle \Delta x^2 (\tau) \right\rangle = 2D\tau^{\alpha(\tau)} \tag{2.2}$$

Here D is the probe diffusivity and $\alpha(\tau)$ is the diffusive exponent, equivalent to the logarithmic slope of the mean-squared displacement:

$$\alpha (\tau) = \frac{d\ln \left\langle \Delta x^2 \right\rangle}{d\ln \tau} \tag{2.3}$$

$\alpha(\tau) = 1$ for diffusion in a Newtonian fluid, whereas probes in non-Newtonian fluids generally exhibit sub-diffusion with $0 < \alpha(\tau) < 1$. Unbiased statistical results for the ensemble average of MSD and the ensemble variance of MSD as a function of lag time τ are calculated using the estimators described by Savin and Doyle [121] for multiple particle tracking in heterogeneous

systems. Software to implement these calculations in the IDL language is publically available (`http://web.mit.edu/savin/Public/.Tutorial/` 'Microrheology of Heterogeneous Systems', T. Savin). Measured MSD data is corrected for static error by subtracting the apparent MSD of probe particles immobilized in a 3 wt% Agarose gel [28] (see Section 1.2.1 and Equation 1.6). Typical results for the MSD as a function of τ and dispersion age time t_w are shown in Fig. 2.1(b). As expected for a system that gels over time, the data exhibits a logarithmic slope $\alpha(\tau)$ close to 1 at early age times, with the slope decreasing as the material ages. After gelation, the MSD exhibits a plateau at long lag times.

Measurements of $\langle \Delta x^2(\tau) \rangle$ can be used to obtain the linear viscoelastic moduli via a generalized Stokes–Einstein relation [96, 109]. This relation assumes that the probe particle inertia is negligible and that the probes experience a homogeneous continuum local environment. For smoothly varying MSD data capable of being fit to the form in Eq. 1, the generalized Stokes–Einstein relation simplifies to the expression [97]

$$G^*(\omega = 1/\tau) = \left\{ \frac{1}{a \langle \Delta x^2(\tau) \rangle} \right\} \frac{k_B T}{3\pi} \frac{\exp[i\pi\alpha(\tau)/2]}{\Gamma[1+\alpha(\tau)]} \tag{2.4}$$

Here $G^*(\omega) = G'(\omega) + iG''(\omega)$ is the complex modulus, a the probe radius, k_B the Boltzmann constant, and T the temperature. Γ represents the Γ-function. The angular frequency ω is the inverse of the lag time τ that is probed.

2.3.3 Bulk Rheology

Bulk rheology measurements are made using an ARG-2 stress-controlled rheometer from TA Instruments. In order to obtain reliable data in the pre-gel state at early age times when the viscosity of the Laponite® dispersion is quite low, an aluminum double-gap concentric cylinder Couette geometry is used [see Fig. 1.1(c)], maximizing solid–liquid contact. The inner stator of the geometry has a radius of 20.00 mm, and the inner and outer rotor radii are 20.38 mm and 21.96 mm, respectively. The fluid sits in two gaps on either side of the rotor, both having a thickness of 0.38 mm, with an immersed cylindrical height of 59.5 mm. The Couette cell is equipped with water circulation tubes for temperature control, and is maintained at the same temperature as microrheology experiments at $T = 23 \pm 0.1$ °C. The Laponite® dispersion is prepared in the same way as in the microrheology experiments, and is introduced into the Couette cell immediately after filtering, which we again mark as the time of zero age. Subsequently, the sample is pre-sheared at a shear rate of $\dot{\gamma} = 250$ s^{-1} for 30 s prior to measurement, helping to ensure a reproducible initial condition. Though the pre-shear may keep aggregates from forming and partially rejuvenate the fluid [36], we find this additional rejuvenating effect to be negligible when the pre-shear is performed immediately after filtration. Oscillatory time sweep tests are used to measure the linear viscoelastic moduli, G' and G'', as a function of age time at a constant angular frequency of $\omega = 1$ rad/s. In order to obtain reliable measurements at early age times, an oscillatory stress of amplitude $\sigma_0 = 0.02$ Pa is initially applied, with this first step terminating once the strain amplitude γ_0 decreases to $\gamma_0 = 0.02$. Though strains in this step may initially appear to be in the nonlinear regime, the material is still essentially a viscous liquid, so that results are approximately strain-independent. Once the strain amplitude decreases to $\gamma_0 = 0.02$, a second step applies a continuous oscillatory strain with a constant amplitude of $\gamma_0 = 0.02$. We have checked that the rheometer feedback mechanism is sufficient to maintain the applied strain within 0.02 ± 0.001.

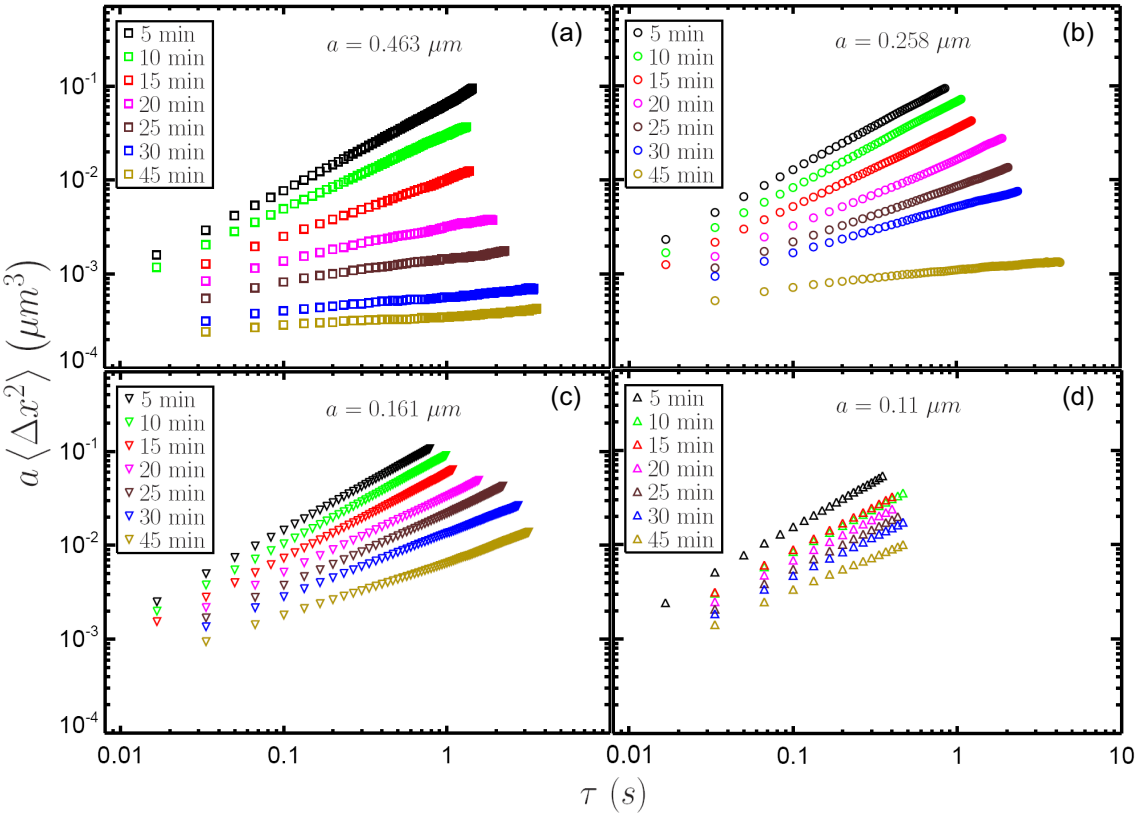

Fig. 2.2: *Scaled MSD versus lag time for various probe sizes in an aging 1 w% Laponite® dispersion. Probe radii are (a)* $a = 0.463\ \mu m$*, (b)* $a = 0.258\ \mu m$*, (c)* $a = 0.161\ \mu m$*, and (d)* $a = 0.11\ \mu m$*. For a homogeneous material with no length-scale dependence, data for all probe sizes should superimpose at a given dispersion age, in contrast to the results above. This non-superposition of data for various probe sizes implies that the dispersion structure and rheology are length-scale-dependent, and that the dispersion is heterogeneous in nature.*

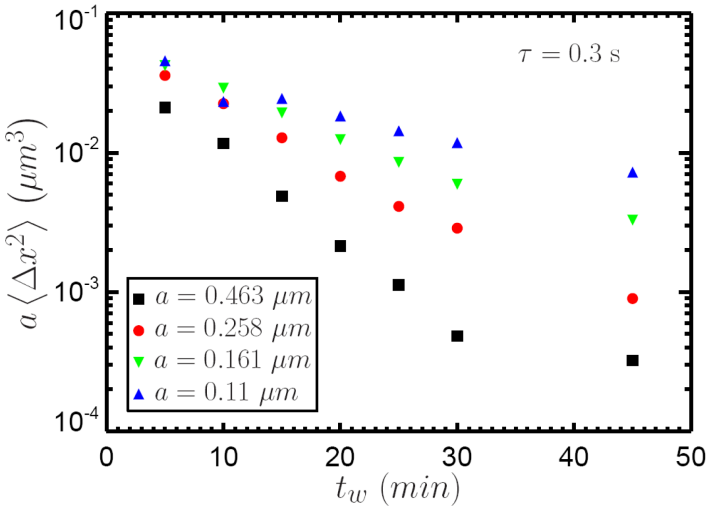

Fig. 2.3: *Scaled MSD versus age time for various probe sizes in a 1 wt% Laponite® dispersion at a constant lag time of $\tau = 0.3$ s. Probe-size effects are clearly observed, as the non-superposition of data for different probe sizes indicates a variation in structure and rheology at different length scales. The deviations generally grow with age, signifying that the length-scale dependence of the rheology becomes more pronounced as the microstructure of the dispersion evolves.*

2.4 Results and Discussion

2.4.1 Effects of Probe Size on Measured Rheology

It was previously noted that the diffusive exponent $\alpha(\tau)$ in Equation 2.3 describes the nature of the probe diffusion in the fluid (i.e Newtonian diffusion or sub-diffusion). For a continuum fluid with homogeneous rheological properties across the length scales being probed, $\alpha(\tau)$ is purely a fluid property and thus should be independent of probe size. Therefore, we see from Equation 2.4 that if the material exhibits the same properties at all length scales probed, the factor will be independent of probe size. In Fig. 2.2, $a\langle\Delta x^2(\tau)\rangle$ is plotted as a function of lag time τ for four different probe sizes in an aging 1 wt% Laponite® dispersion. Though there is reasonably good agreement between different probe sizes at early age times, significant deviations are observed as the material ages. This is seen more clearly in Fig. 2.3, where the factor $a\langle\Delta x^2(\tau)\rangle$ is plotted as a function of the age time t_w for the four probe sizes at a single value of the lag time, $\tau = 0.3$ s. The data show that at 30 min age, for example, values of $a\langle\Delta x^2(\tau)\rangle$ differ by more than an order of magnitude between the smallest and largest probes. These results indicate that there are strong probe size effects and that the Laponite® dispersion is not a continuum fluid with homogeneous properties across the length scales probed.

Because of this scale-dependent behavior, it is necessary to proceed with care when extracting rheological properties from MPT measurements of $\langle\Delta x^2(\tau)\rangle$. We therefore consider rheological properties found from MPT as 'effective' or 'apparent' properties. The effective linear viscoelasticity

at the microscopic scale can be calculated from the data in Fig. 2.2 by applying the generalized Stokes–Einstein relation in Equation 2.4. When the diffusive exponent $\alpha(\tau)$ satisfies $0.5 < \alpha(\tau) < 1$, the material is dominated by viscous losses, whereas when $0 < \alpha(\tau) < 0.5$, the material is elastically dominated. Fig. 2.4 shows the frequency dependence of the storage and loss moduli calculated from Equation 2.4 at four age times for a representative probe size of $a = 0.463$ μm. The loss modulus $G''(\omega)$ is dominant at early age times, indicating an initially viscous 'sol'. Both moduli increase with age time as the material develops structure and forms a gel, with the storage modulus $G'(\omega)$ eventually surpassing $G''(\omega)$. At late age times, $G'(\omega)$ is dominant and only weakly frequency-dependent, while $G''(\omega)$ exhibits a minimum value.

These results are consistent with a system undergoing gelation and are in qualitative agreement with previous observations on both bulk and microscopic scales [106, 58, 59]. We note in Fig. 2.4(b) that at the time when $G'(\omega) \approx G''(\omega)$, both moduli exhibit approximately the same power law frequency dependence. This is a hallmark of the critical gel point [9], and indicates that the gelation time t_{gel} can be approximated as the time when the storage and loss moduli are equal. This is seen also in Fig. 2.5, where the loss tangent $\tan\delta = G''/G'$ is plotted as a function of angular frequency ω for various dispersion age times. According to the gelation theory of Chambon and Winter [9], $\tan\delta$ is independent of frequency at the critical gel point. Interpolating between the data in Fig. 2.5, $\tan\delta$ is approximately independent of frequency at an age time of about 17 min; at this time $\tan\delta = G''/G' \approx 1$ for all frequencies. This again indicates that the gel point for this system is determined by the time when $G' \approx G''$. Similar behavior was seen for all probe sizes and Laponite® concentrations, and so we subsequently take the gelation time t_{gel} as the age time when $G' \approx G''$.

Applying Equation 2.4 to MSD data for different probe sizes allows the direct comparison of apparent rheological properties in this heterogeneous clay dispersion at different length scales. Fig. 2.6 shows the evolution of the storage and loss moduli with age time for a 1 wt% Laponite® dispersion at a representative frequency of $\omega = 1$ rad/s (i.e, lag time $\tau = 1$ s). Results for two different probe sizes are shown, as well as the bulk response. In agreement with Oppong *et al.*[59], we observe significant deviation in the linear viscoelastic measurements between bulk and microscopic scales, with the bulk moduli exhibiting values that are at least an order of magnitude larger than those measured by MPT. The dispersion also reaches the gel point significantly earlier at the bulk scale. As the probe size is decreased from $a = 0.463$ μm to $a = 0.11$ μm, these trends continue. At a given age time, smaller probes result in lower measured viscoelastic moduli, sometimes by more than an order of magnitude. This indicates that the material is effectively a weaker gel at the smaller length scale. Additionally, t_{gel} is observed to be about 120 min with the smaller probes, significantly delayed compared to the measurement of $t_{gel} = 17$ min with the larger probes. Specifically, at $t_{gel}(a = 0.463\ \mu\text{m}) = 17$ min, the smaller probes are still quite mobile, diffusing as if in a relatively low viscosity fluid with weak elasticity. The probe-size dependence of the apparent t_{gel} are shown in Fig. 2.7 for a 1 wt% Laponite® dispersion. Almost an order of magnitude increase in t_{gel} is observed as the probe diameter decreases by about an order of magnitude.

2.4.2 Microstructural Description

We can conclude from these results that the Laponite® dispersion is not a continuum gel with homogeneous viscoelastic properties across the length scales probed; rather, in qualitative agreement with the long age time observations of Pignon *et al.* [103], there must be microstructural features

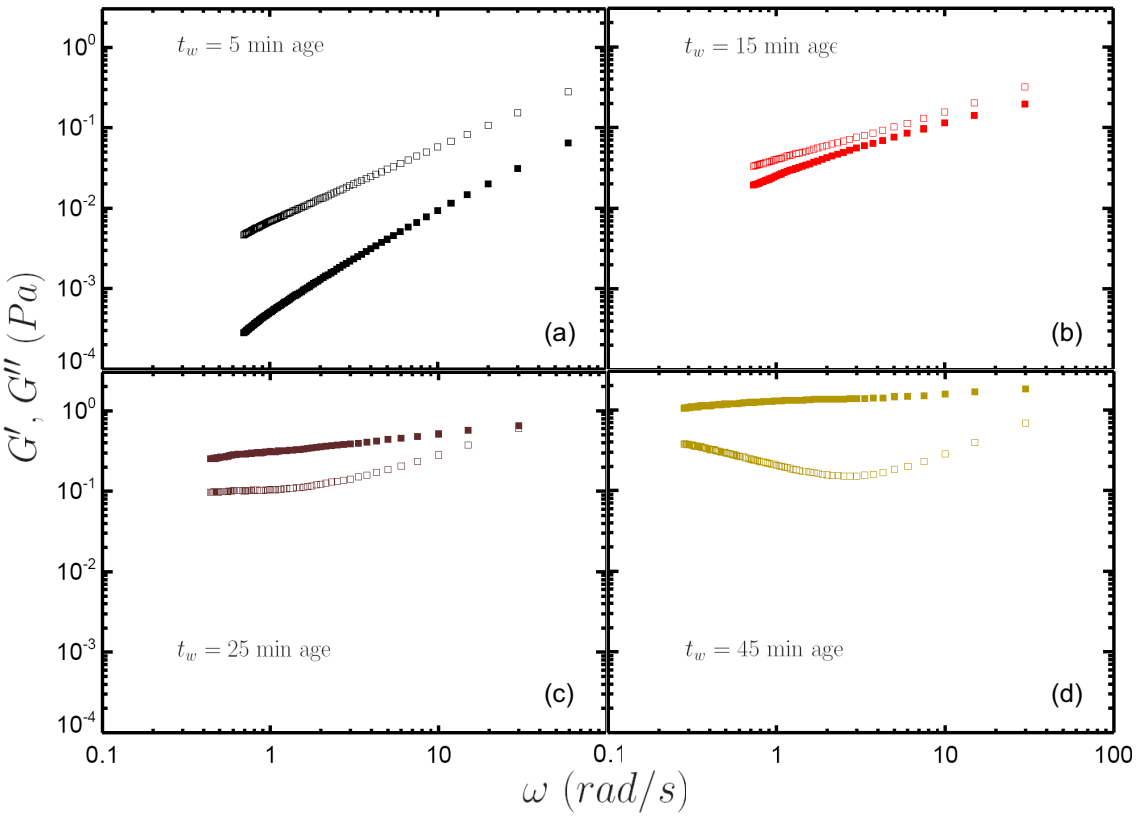

Fig. 2.4: *Effective viscoelastic moduli calculated from microrheology versus angular frequency for 1 wt% Laponite® and a representative probe size of* $a = 0.463$ *μm at age times of (a) 5 min, (b) 15 min, (c) 25 min, and (d) 45 min. Filled symbols* $= G'$*, open symbols* $= G''$*. Though the dispersion is originally viscous-dominated, a crossover to elastic-dominated behavior occurs between 15 and 25 min of age. Near this crossover time at 15 min, the moduli have approximately the same frequency dependence, indicative of gelation [9].*

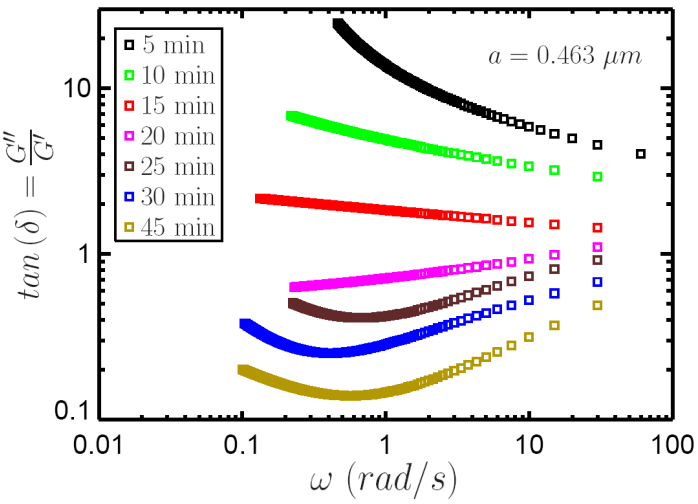

Fig. 2.5: *Loss tangent calculated from microrheology versus angular frequency for 1 w% Laponite® and a representative probe size of* $a = 0.463\ \mu m$. $\tan\delta$ *is approximately independent of frequency when* $\tan\delta = G''/G' \approx 1$, *indicating that gelation occurs when* $G' \approx G''$ *[9].*

in the gel on length scales comparable to the probe particle sizes ($\sim$ 0.1–1 μm). This microstructure could result in different local environments, with different rheological properties, at different length scales. Since probe particle motions are directly related to structure and microrheological properties on the length scale of their size [24], this microstructure could provide an explanation for the observed phenomena. Because individual Laponite® particles are much smaller than the probes, the microstructure must result from larger aggregates of Laponite® particles, as proposed by Pignon *et al.* [103]. These aggregations can create gelled regions of relatively high Laponite® concentration, and regions where the Laponite® has been depleted, resulting in a type of porous network structure.

Based on our observations and those of previous authors, we propose the following scenario for the evolution of the microstructure with age time t_w. At early age times $t_w \ll t_{gel}$, the dispersion is homogeneous at the microscopic scale, with Laponite® crystals (or small clusters of crystals) randomly distributed throughout the medium and diffusing freely. However, as the crystals diffuse, they encounter one another and occasionally aggregate due to Van der Waals forces and electrostatic attraction. These aggregates grow more extended over time and eventually some span the container: this percolation characterizes the bulk gelation time. At this point, however, most of the dispersion still appears relatively homogeneous and viscous on the microscopic scale, and probe particles still diffuse through the 'sol' with only slight hindrance [59]. As the microstructure continues to develop, interconnected elastic clusters take up more and more of the dispersion volume, eventually trapping most of the larger probe particles in a viscoelastic gel network. Smaller probe particles, however, are not as restricted, and though some may have been trapped in gelled regions, most are still able to diffuse in non-gelled, or more weakly gelled pores in the aggregate structure. After a longer period of time, the smaller probes also become trapped by the shrinking pores in the gel network,

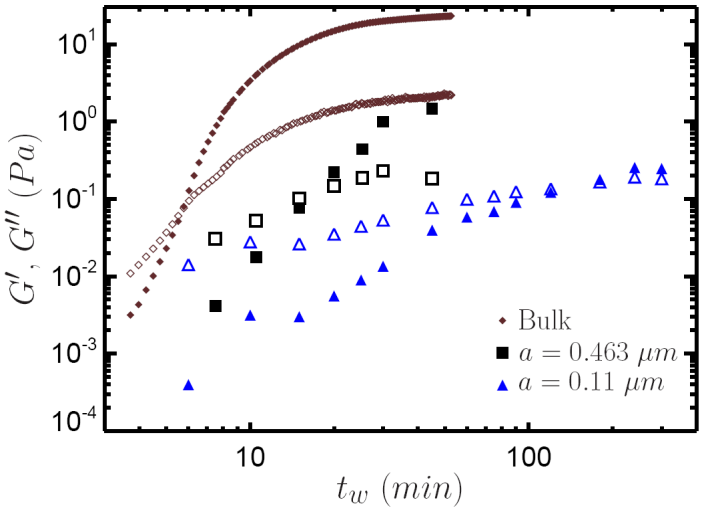

Fig. 2.6: *Viscoelastic moduli as a function of age time for 1 w% Laponite® at a representative frequency of $\omega = 1$ rad/s. Bulk rheology data as well as microrheology data for two different probe sizes are shown. G' = filled symbols, G'' = open symbols. Though the trends are similar, at a given age time, probing at smaller length scales using microrheology results in lower apparent moduli (i.e. a weaker gel). The observed gelation time is also delayed when determined using a local versus a bulk measurement.*

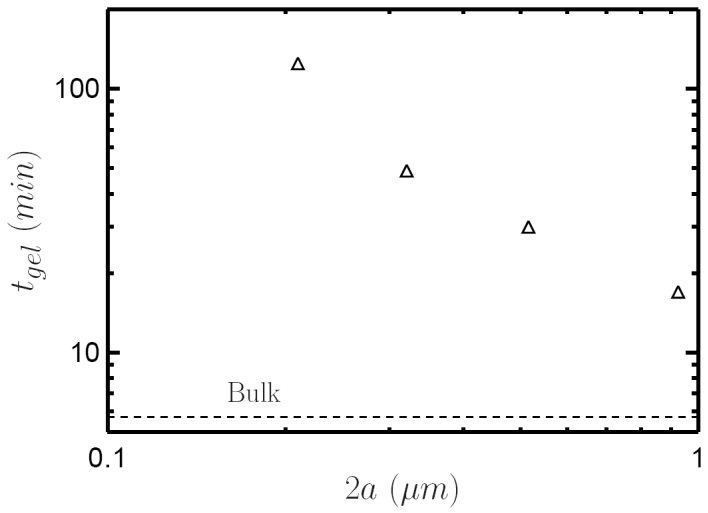

Fig. 2.7: *Apparent gelation time versus probe diameter for a 1 w% Laponite® dispersion. The bulk gelation time is denoted by the dashed line. From the bulk value to that observed for the smallest probe size, the gelation time changes by over an order of magnitude.*

leading eventually to the observation of a gelation time even at the length scale of the smallest probes.

If the proposed microstructural description is accurate, there are a number of indicators we would expect to observe. First, we would expect to see evidence of a spatially heterogeneous medium. That is, for intermediate t_w, probe particle trajectories should reflect the fact that some probes are trapped in more strongly gelled regions while others diffuse more freely in pores and weakly gelled regions. At a given t_w, we expect the microstructure will appear more or less heterogeneous at different length scales, so that the heterogeneity of the probe dynamics will also depend on the probe size. Second, we would expect probe trajectories to reflect the confinement due to the microstructure of the surrounding gel. Specifically, for particles diffusing in pores or other confined regions, we expect successive probe displacements over a sufficiently long lag time to be negatively correlated-having moved along a confined path over one time step, the probe will have a higher probability of rebounding in the opposite direction over the subsequent time step than a probe particle that is not confined, for which displacements would be uncorrelated [122, 123, 111, 124, 59]. Lastly, analysis of these correlations and the spatial heterogeneity for different probe sizes should reveal a characteristic length scale (characteristic pore size, cluster size, etc.) for the microstructure at a given age time t_w.

2.4.3 Heterogeneity

Savin and Doyle [121] describe a method for obtaining unbiased quantitative measures of spatial heterogeneity in a multiple particle tracking experiment (Additional available at `http://web.mit.edu/savin/Public./Tutorial/.`). Briefly, the result of the finite depth of tracking in MPT (i.e.,

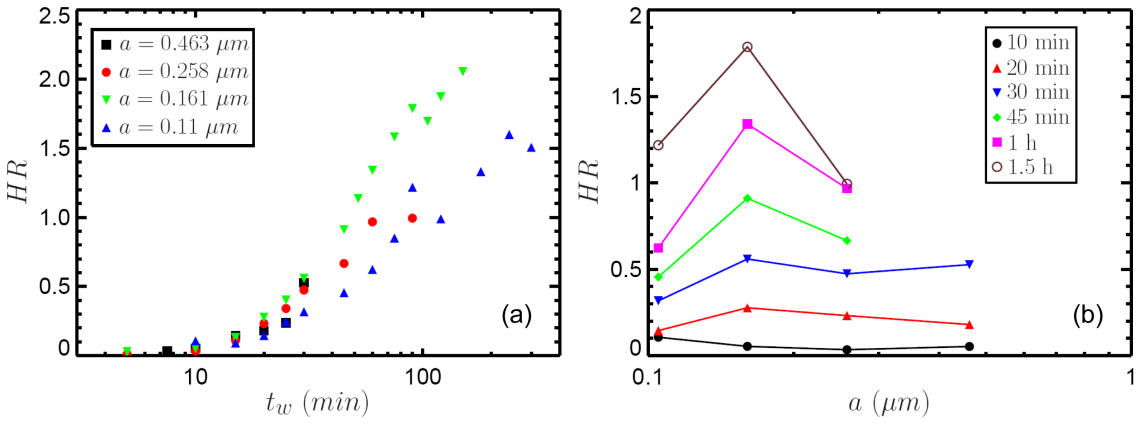

Fig. 2.8: *Heterogeneity Ratio HR for four probe sizes in 1 w% Laponite® at a lag time of $\tau = 0.33$ s. (a) At early age times, heterogeneity is negligible for all probe sizes. As the dispersion ages and structure develops, significant heterogeneity is observed and HR becomes dependent on probe size. (b) At long age times, the relationship between HR and probe size is non-monotonic, with the heterogeneity exhibiting a maximum for a probe size of $a = 0.161$ μm for $t_w \geq 30$ min.*

the fact that particles diffuse in and out of focus in the z-direction) is that simple ensemble averaging of individual trajectory MSD's in a system with spatially heterogeneous rheology produces a statistical bias toward more mobile particles-these particles leave and enter the trackable depth more often, registering many short, mobile trajectories. If each trajectory is weighted by a factor proportional to its duration in time, however, unbiased estimators for the ensemble average of MSD and the ensemble variance of MSD can be calculated. From these estimators, a quantitative dimensionless measure of the spatial heterogeneity can be defined, which we shall call the Heterogeneity Ratio, HR:

$$HR = \frac{M_2(\tau)}{M_1(\tau)^2} \tag{2.5}$$

Here $M_1(\tau)$ is the estimator for the ensemble average of MSD, and $M_2(\tau)$ is the estimator for the ensemble variance of MSD, both functions of the lag time τ. As a point of reference, in a theoretical situation of MPT in an equally-weighted bimodal fluid where half the microscope view frame is water ($\eta_1 = 0.9$mPas), and half is a Newtonian fluid with viscosity $\eta_2 = 10\eta_1$, the result is a Heterogeneity Ratio of $HR \approx 0.6$. Additionally, exploratory calculations show the maximum value of HR for an equally-weighted bimodal Newtonian fluid is 3.

In Fig. 2.8(a), the Heterogeneity Ratio HR is plotted as a function of t_w for a 1 wt% Laponite® dispersion and four probe sizes at a lag time of $\tau = 0.33$ s. The Laponite® dispersion does exhibit significant heterogeneity and HR generally increases with t_w, consistent with our hypothesis for the microstructural evolution. Further, there is a non-monotonic dependence of HR on the probe size. This is highlighted in Fig. 2.8(b) where HR is plotted as a function of probe radius. For $t_w \geq 30$ min, HR is peaked at the intermediate probe size of $a = 0.161$ μm. To understand why

this occurs, we examine the particle trajectories in further detail to elucidate the nature of the heterogeneous probe dynamics.

Representative probe particle trajectories are shown in Fig. 2.9 for a 1 w% Laponite® dispersion at $t_w = 90$ min. Twenty discrete trajectories are shown for probes with radii (a) $a = 0.258$ μm and (b) $a = 0.161$ μm, which exhibit Heterogeneity Ratios of $HR = 0.99$ and $HR = 1.72$, respectively. All of the larger probe particles seem to be immobilized to varying degrees, diffusing around fixed locations. In contrast, some of the 0.161μm radius particles are immobilized, while others exhibit tortuous paths, as if exploring pores in the dispersion microstructure or 'hopping' between adjacent distinct regions. As an approximation, it is possible to group these two types of trajectories into two populations, mobile and immobile, corresponding to spatial regions of two different average rheological properties. This is demonstrated in Fig. 2.10(a), where for each trajectory we plot the product of the range $[\max(r_x) - \min(r_x)]$ and the standard deviation σ_x of the x-coordinate position of the particle. The ordinate is therefore a simple measure of the mobility of a particle in a trajectory. Identifying an approximate cutoff, we designate the mobile particles as those falling above the dotted line, and the immobile particles as those falling below the dotted line. In Fig. 2.10(b), the probability distribution of displacements $P(\Delta x)$ over a lag time τ, known as the van Hove correlation function, is plotted for the mobile and immobile populations, as well as for the full data set with all trajectories. Displacements are taken over a lag time of $\tau = 0.33$ s. The immobile population is in good agreement with the full data set for small displacements, while the mobile population characterizes the region of large displacements. This demonstrates that the majority of small displacements come from immobile particles, while mobile particles contribute most of the large displacements.

In Fig. 2.11, van Hove correlation data is shown for three different probe sizes in a 1 wt% Laponite® dispersion at an age time of $t_w = 90$ min. Probe particle displacements are again taken over a lag time of $\tau = 0.33$ s. If the material was homogeneous, the van Hove correlation function would exhibit a characteristic single Gaussian shape; deviations from single Gaussian behavior indicate heterogeneous probe dynamics. We note also that the Heterogeneity Ratio HR is similar to the non-Gaussian parameter N reported by previous authors [59, 125, 126], except that statistical biases introduced by the finite depth of tracking in MPT are corrected. As expected based on the values of HR shown in Fig. 2.8 and the heterogeneous dynamics seen in Fig. 2.9, deviations from single Gaussian behavior are observed, with probes of radius $a = 0.161$ μm exhibiting the most significant deviations. Motivated by the results from Fig. 2.10(b), each of the van Hove correlation functions are fitted with two Gaussian distributions [126]: one capturing the small displacements (contributed mostly by immobile particles), and one capturing the large displacements (contributed mostly by mobile particles). The cutoff $|\Delta x|$ between these two regions identifies a characteristic length scale in the system. Probe particle displacements begin to deviate from single Gaussian behavior very close to $|\Delta x| = 0.161$ μm, which is the value of the probe radius at which a peak in HR is observed. This value of $|\Delta x| = 0.161$ μm is denoted by the black dotted lines in Fig. 2.11. The fact that this cutoff $|\Delta x|$ is independent of probe size suggests that it is a microstructural length scale. We assert, therefore, that the peak in HR at $a = 0.161$ μm and $t_w \geq 30$ min is due to a microstructural length scale in the dispersion that is very close in size to this probe radius. A similar length scale was measured by Mourchid *et al.* [45] and Pignon *et al.* [103] using various scattering techniques. The tortuous paths exhibited by trajectories in Fig. 2.9(b) imply that this length scale may correspond to a characteristic pore radius in the gelled dispersion.

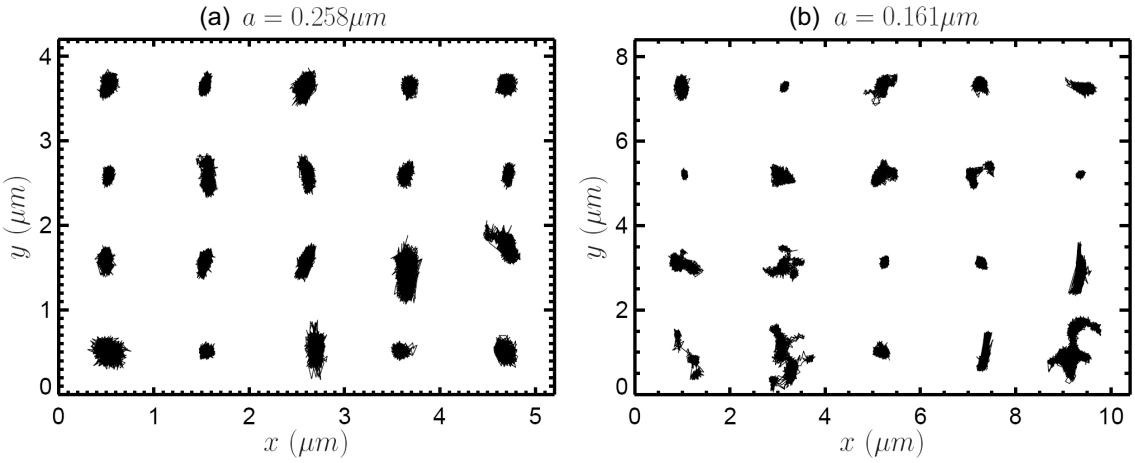

Fig. 2.9: *Representative probe particle trajectories in 1 w% Laponite® at* $t_w =$ 90 *min. Probe sizes are (a)* $a = 0.258$ μm *and (b)* $a = 0.161$ μm*, resulting in Heterogeneity Ratios of* $HR = 0.99$ *and* $HR = 1.78$*, respectively. While all the larger probes seem to diffuse around fixed locations, a significant fraction of the smaller probe trajectories exhibit more tortuous paths and/or 'hopping' between distinct regions. At the same time, some of the smaller probe particles are relatively immobilized. The greater degree of variation in the dynamics for the smaller probe particles leads to the larger value of* HR*.*

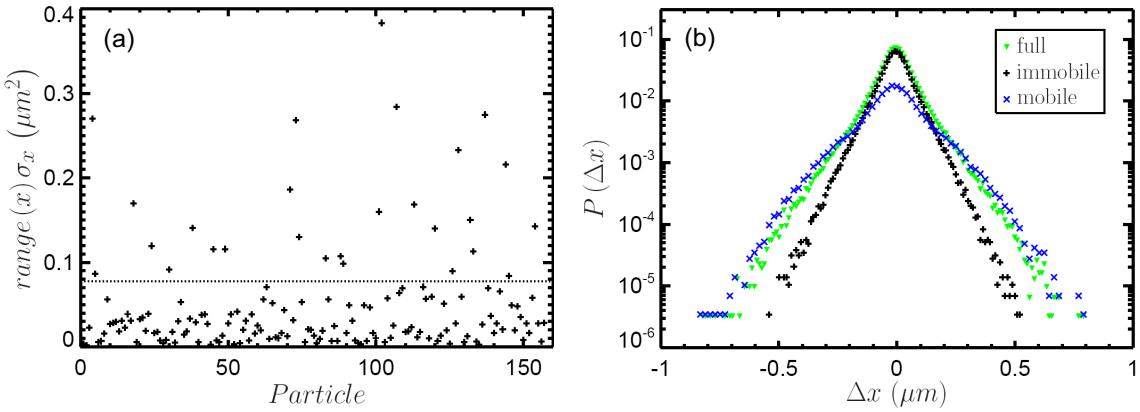

Fig. 2.10: *Partitioning probe particles into two populations, mobile and immobile, for $a = 0.161$ μm in 1 w% Laponite® at $t_w = 90$ min. (a) As an indicator of the mobility of particles, the product of the range and standard deviation of the x-coordinate position of probe particles is plotted. Particles falling above the dotted line are designated as a mobile population, and those below the line as an immobile population. (b) van Hove correlation data for mobile and immobile populations, as well as the full data set including all trajectories. Displacements over a lag time of $\tau = 0.33$ s are shown. There is good agreement between the immobile population and the full data set for small displacements, while the mobile population characterizes the outer regions of large displacements.*

2.4.4 Correlations Between Successive Probe Displacements

The study of correlations between successive particle displacements has been adopted from examinations of cage effects in colloidal glasses [122, 123] and applied to multiple particle tracking experiments, in which correlations yield insight into the confinement of probe particles by the surrounding fluid microstructure [111, 124, 59]. Let $\mathbf{r}_{01}$ and $\mathbf{r}_{12}$ represent successive two-dimensional displacement vectors of a probe particle over a lag time τ. That is, between time t_0 and $t_1 = t_0 + \tau$, the probe's displacement in the plane of focus is given by $\mathbf{r}_{01}$, and between time t_2 and $t_2 = t_1 + \tau$, the probe's subsequent displacement is given by $\mathbf{r}_{12}$. If the probes are executing a random walk, as in a viscous Newtonian fluid, then $\mathbf{r}_{01}$ and $\mathbf{r}_{12}$ will be uncorrelated. Successive displacements will be correlated, however, if probes are confined by the fluid microstructure. The correlation between successive displacements $\langle x_{12} \rangle$ is defined as

$$\langle x_{12} \rangle = \left\langle \frac{\mathbf{r}_{01} \cdot \mathbf{r}_{12}}{r_{01}} \right\rangle \tag{2.6}$$

Here r_{01} is the magnitude of the initial displacement, $r_{01} = \|\mathbf{r}_{01}\|$, and angled brackets represent ensemble averages. To gain a better physical understanding of $\langle x_{12} \rangle$, consider a probe particle confined in a pore and assume its displacement over an initial lag time τ is $\mathbf{r}_{01} = \mathbf{r}\,(t_0 + \tau) - \mathbf{r}\,(t_0)$. Therefore, $\mathbf{r}_{01}$ represents an accessible path for the confined probe, and in the subsequent time step τ there is an increased probability that the probe will retrace its steps through that known

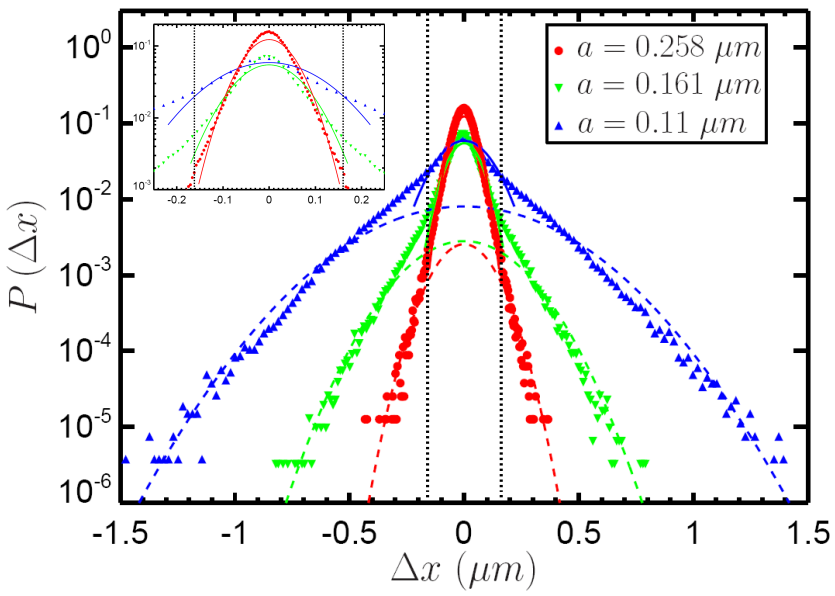

Fig. 2.11: *van Hove correlation plots for three probe sizes in 1 w% Laponite® at* $t_w = 90$ *min. Displacements over a lag time of* $\tau = 0.33$ *s are shown. The distribution broadens as the probe radius decreases, reflecting the increased mobility of smaller particles. Deviations from single Gaussian behavior are a result of the spatial heterogeneity in the dispersion, with Heterogeneity Ratios of* $HR = 0.99$*, 1.78, and 1.2 being observed for the probe sizes* $a = 0.258$ μm*, 0.161* μm*, and 0.11* μm*, respectively. For each probe size, the data is sub-divided into two regions, each fit by a Gaussian distribution. The fits to the immobile subsets with small displacements are shown as solid lines (with a zoom shown in the inset), and the fits to the subsets of mobile particles with large displacements are shown as dashed lines. The vertical black dotted lines correspond to* $|\Delta x| = 0.161$ μm*, which is equal to the intermediate probe size exhibiting a peak in heterogeneity in Fig. 2.8(b). The experimental data for all probe sizes begins to deviate from single Gaussian behavior very close to this value of* $|\Delta x|$*, suggesting that it may correspond to a characteristic microstructural length scale.*

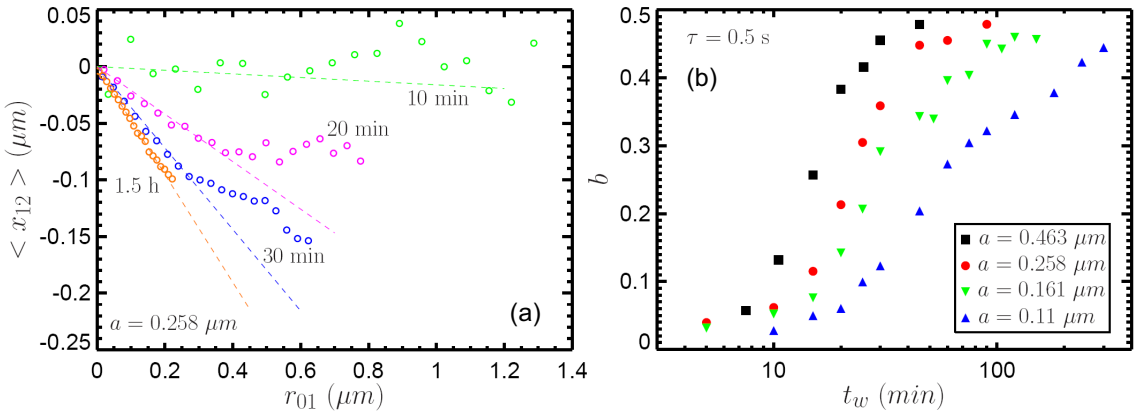

Fig. 2.12: *The degree of correlation between successive probe particle displacements at four age times in 1 w% Laponite®. Data is shown for a representative probe size of $a = 0.258$ μm and a lag time of $\tau = 0.5$ s. Dashed lines show linear fits of the form $\langle x_{12} \rangle = -br_{01}$ to the first 10 points of data. The negative slope of the dashed lines gives the parameter b, which increases with the dispersion age time. The displacement magnitude r_{01} at which correlations deviate from linear behavior indicates a microstructural length scale in the system. (b) Evolution of the b parameter with age time for four probe sizes in 1 wt% Laponite®, over a lag time of $\tau = 0.5$ s. The b parameter grows with age and exhibits probe-size dependence, though self-similar behavior is seen between all probe sizes. The data reaches a plateau value of b slightly less than 0.5.*

accessible path. In that case, $\mathbf{r}_{12}$ would be in the opposite direction of $\mathbf{r}_{01}$, so that $\mathbf{r}_{01}$ and $\mathbf{r}_{12}$ are negatively correlated. We therefore expect $\langle x_{12} \rangle$ to be negative when microstructural confinement effects probe motion.

$\langle x_{12} \rangle$ is plotted as a function of r_{01} in Fig. 2.12(a) at four age times for 1 wt% Laponite® and a representative probe size of $a = 0.258$ μm. Correlations between successive displacements of duration $\tau = 0.5$ s are shown. While values of $\langle x_{12} \rangle$ are scattered around 0 at $t_w = 10$ min, the correlations grow in magnitude as the system ages. The degree of correlation also grows with the size of the initial displacement r_{01}, and we observe a linear relationship of the form $\langle x_{12} \rangle = -br_{01}$. The coefficient b, which grows with t_w as the microstructure develops, is reported to represent the ability of the fluid microstructure to restrict the motion of the probe particles [59]. b is plotted as a function of t_w for four probe sizes in Fig. 2.12(b). Though b is probe-size–dependent at a given t_w, data for different probe sizes exhibit self-similar age-time dependence, suggesting a common scaling. At late age times, b seems to plateau at $b = 0.5$ for all probe sizes. The fact that correlations become increasingly significant as the dispersion ages implies that microstructural confinement effects on probe motion are important, which is consistent with our hypothesis for the microstructural evolution in Section 2.4.2. In Fig. 2.12(a), the degree of correlation is seen to deviate from linear behavior past a critical value of r_{01} for $t_w > 10$ min. This value of r_{01} represents a microstructural length scale in the system. Though these results are in contrast to the results of Oppong *et al.* [59], these authors use only a larger probe size ($a = 0.50$

μm), so that initial displacements r_{01} large enough to observe the deviation from linearity are inaccessible. Upon measuring this critical displacement $r_{01,crit}$ for various probe sizes and age times, we find $\bar{r}_{01,crit}$, approximately twice the length scale observed in the previous section from heterogeneity measurements. We propose that these two independent measurements actually reflect the same microstructural length scale, and that the difference by a factor of 2 is a result of the different methods of probing it. Having examined the evolution of the b parameter and its probe-size dependence in an aging Laponite® dispersion, we now consider in more depth the physical meaning of b. It has been reported [59] that b reflects microstructural confinement; however, one could imagine that successive displacements may also be correlated for probes embedded in a model material with no microstructure but with viscoelasticity that persists on time scales of the lag time τ or longer. To investigate this, we consider probes suspended in a Kelvin–Voigt model viscoelastic solid, which is represented by a mechanical equivalent circuit of a spring and a dashpot in parallel. The linear spring has an elastic modulus G, and the dashpot has a Newtonian viscosity η. The relaxation time of the material is therefore given by $\lambda_V = \eta/G$. The equation of motion for a Brownian probe particle diffusing in such a material is [127]

$$\lambda_V \lambda_I \ddot{\mathbf{r}}(t) + \lambda_V \dot{\mathbf{r}}(t) + \mathbf{r}(t) = \mathbf{f}(t)/6\pi aG \tag{2.7}$$

where $\lambda_I = m/6\pi aG\lambda_V$ is an inertial time scale (with m being the mass of the probe particle) and $\mathbf{f}(t)$ is the stochastic Brownian force [128]. By taking the Fourier transform of both sides of Equation 2.7, we obtain an expression for the power spectral density of the position $S^*_{\mathbf{r}}(\omega) = \left\langle \|\mathbf{r}^*\|^2(\omega) \right\rangle$ [127],

$$S^*_{\mathbf{r}}(\omega) = \frac{\lambda_V k_B T/\pi aG}{\left(1+\lambda_+^2\omega^2\right)\left(1+\lambda_-^2\omega^2\right)} \tag{2.8}$$

where * represents the complex conjugate and the roots $\lambda_\pm$ are given by

$$\lambda_\pm = \frac{\lambda_V}{2}\left(1 \pm \sqrt{1-4\lambda_I/\lambda_V}\right) \tag{2.9}$$

In writing Equation 2.8 we have applied the fluctuation-dissipation theorem, which can be represented mathematically as

$$S^*_{\mathbf{f}}(\omega) = \left\langle \|\mathbf{f}^*\|^2(\omega) \right\rangle = 36\pi aG\lambda_V k_B T \tag{2.10}$$

Using the method detailed in Appendix A.1, we can obtain the relationship between $\langle x_{12}\rangle$ and r_{01},

$$\langle x_{12}\rangle = -\frac{1}{2}\left[1-\exp\left(-\tau/\lambda_V\right)\right] r_{01} \tag{2.11}$$

where τ/λ_V is the ratio between the lag time and the material relaxation time. Comparing this expression to $\langle x_{12}\rangle = -br_{01}$, we find a simple expression for b for probe particles embedded in a Kelvin–Voigt material,

$$b = \frac{1}{2}\left[1-\exp\left(-\tau/\lambda_V\right)\right] \tag{2.12}$$

This expression is plotted in Fig. 2.13. In order to validate the approximations that were made to derive Equation 2.12 (see Appendix A.1), we perform a Brownian dynamics (BD) simulation of a probe particle undergoing Brownian motion in a Kelvin–Voigt material. The details of the

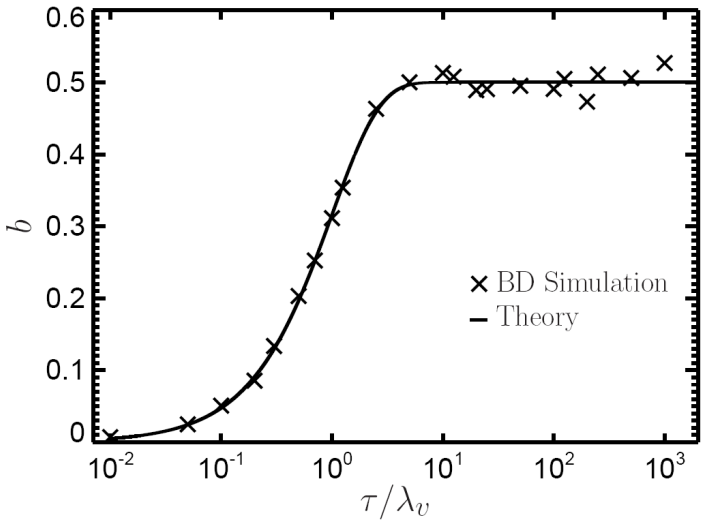

Fig. 2.13: *The variation of b with the dimensionless lag time τ/λ_V for a Kelvin–Voigt material, from theory and Brownian dynamics (BD) simulation. Theoretical results match those from the BD simulation. The plot shows that non-zero values of b can result from elasticity even in a homogeneous material without microstructure. In the case of a Kelvin–Voigt material, b depends solely on the ratio of the relaxation time to the lag time that is probed.*

simulation are given in Appendix A.2. Fig. 2.13 shows that the simulation and the theoretical results match quantitatively. The fact that $b > 0$ for the Kelvin–Voigt material demonstrates that if there is elasticity present, even a continuum material with no microstructural features can exhibit correlations between successive probe displacements. Further, if the relaxation time λ_V is spatially homogeneous (i.e. independent of r_{01}), b is a constant at a given lag time τ, so that there is a linear relationship between $\langle x_{12} \rangle$ and r_{01} for all r_{01}. This indicates that the departure from linearity observed in Laponite® results from microstructural heterogeneities. The connection between b and elasticity implies that the common scaling between the data for different probe sizes in Fig. 2.12(b) may be related to the development of elasticity in the material. That is, if b is plotted as a function of some measure of the local elasticity, the data for different probe sizes may collapse. With this motivation, we plot b as a function of the apparent storage modulus $G'(\omega)$ in Fig. 2.14, where ω is evaluated at the inverse of the correlation lag time $\omega = 1/\tau$. The data for all probe sizes collapses onto a single curve. This suggests that b is more directly related to apparent elasticity than to microstructural confinement in Laponite® dispersions, though the observed elasticity is undoubtedly a result of the structural development in the material. The observation that $\langle x_{12} \rangle$ deviates from a linear variation with r_{01} beyond a critical displacement remains a strong indicator of a microstructural length scale.

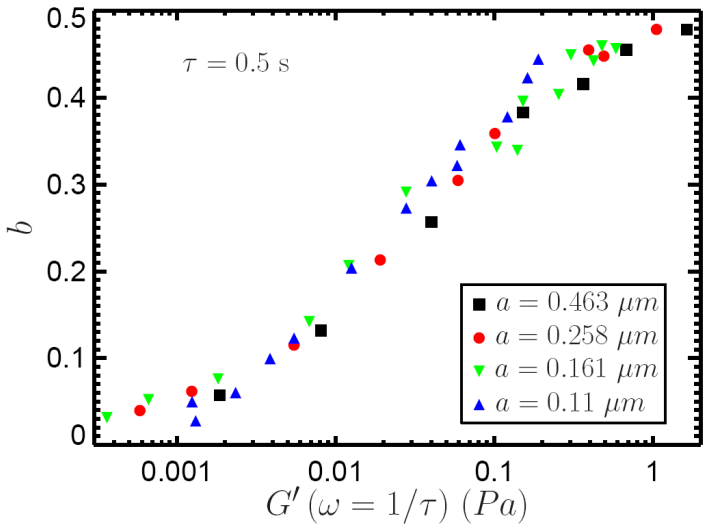

Fig. 2.14: *b plotted against the measured storage modulus for various probe sizes in 1 wt% Laponite®, over a lag time of $\tau = 0.5$ s. $G'(\omega)$ is evaluated at a frequency of $\omega = 1/\tau = 2$ rad/s from MPT measurements at the corresponding probe size. The results for b from various probe sizes collapse, confirming the connection between b and the material elasticity and suggesting that b is more directly related to elasticity than to microstructural confinement for Laponite® dispersions.*

2.4.5 Effects of Laponite® Concentration

All of the experimental results presented thus far have been for a 1 wt% Laponite® dispersion. The observed probe size effects could be interpreted as indicating that at a given age time t_w, the dispersion 'appears' more concentrated in Laponite® as the probe size increases. That is, at a given age time, smaller probes experience local environments that are on average like a relatively dilute dispersion, whereas larger probes experience local environments that are more characteristic of the bulk concentration. Recognizing this, we investigate the connection between probe size effects and Laponite® concentration. Specifically, we examine whether a superposition can be found between concentration and probe size.

Fig. 2.15(a) shows the observed gelation time t_{gel} as a function of probe diameter for three different Laponite® concentrations. The gelation time t_{gel} exhibits a similar trend with probe size for all three dispersions, though the value of t_{gel} is highly sensitive to Laponite® concentration, decreasing rapidly as the concentration is increased by just 0.5 wt%.

We seek a relationship describing the scaling of t_{gel} with the probe radius a and the Laponite® concentration c, expressed in wt%. From Fig. 2.15(a), it appears that t_{gel} follows approximately a power law scaling with probe size a for each concentration. Kroon *et al.* [129] used dynamic light scattering to investigate the sol-gel transition of aqueous Laponite® dispersions with various concentrations. For dispersions with 2.2 wt% $\leq c \leq$ 3.4 wt% and no added salt, they found that the gelation time scales exponentially with c according to $t_{gel} \sim \exp(-2.83c)$. Motivated by these

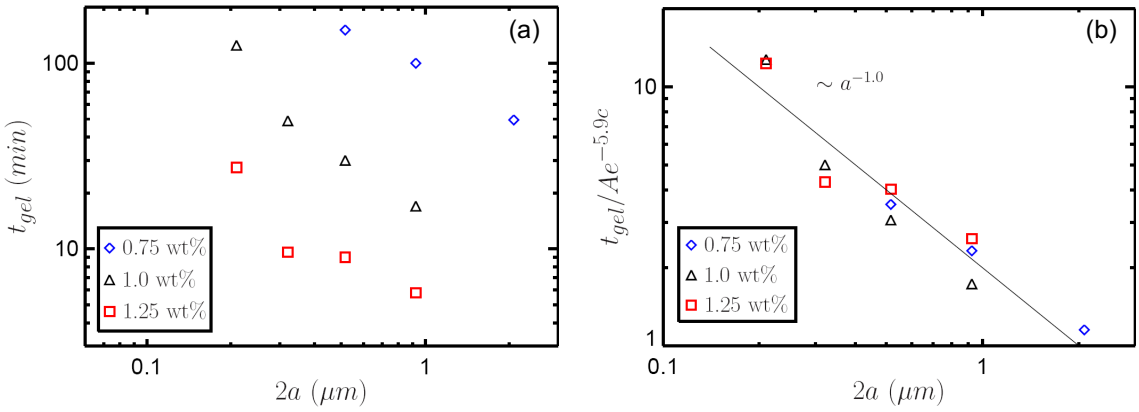

Fig. 2.15: *(a) Apparent gelation time versus probe diameter for three Laponite® concentrations. The gelation time is very sensitive to the Laponite® concentration, decreasing rapidly for small increases in concentration. The probe-size dependence is similar for all three concentrations. (b) Gelation time data scaled by an exponential factor of the Laponite® concentration c in wt%. This scaling serves to collapse the gelation time data for the three concentrations examined onto a single curve, exhibiting a* -1.0 *power law scaling with probe size. The existence of such a master curve is an indication of a concentration–probe-size superposition.*

observations, we therefore assume an empirical expression for t_{gel} of the form

$$t_{gel} = Aa^{\beta}\exp\left(-\kappa c\right) \tag{2.13}$$

where A, β, and κ are constants determined by fitting this expression to the experimental data in Fig. 2.15(a). Using a nonlinear least squares regression, we find the best-fit values to be $A = 3613.7$, $\beta = -1.0$, and $\kappa = 5.9$, for t_{gel} expressed in minutes and a expressed in micrometers. The fitted value of κ is indicative of the strong inverse relationship between gelation time and Laponite® concentration. That is, t_{gel} decreases rapidly even for slight increases in c. The discrepancy in the value of κ as compared to the result of Kroon *et al.* [129] is likely due to the different experimental conditions and sample preparation procedure. In particular, in the present study we control the ionic strength I through the use of added salt, since it is known that the gelation dynamics are sensitive to I [45, 98, 47]. The nearly integer value of β suggests that there may be a relatively simple mechanism underlying the observed scaling, though a detailed mechanistic description is reserved for future work. The ability of Eq. 2.13 to describe the experimental results is demonstrated in Fig. 2.15(b), where the gelation time data in Fig. 2.15(a) has been scaled by the exponential factor $A\exp\left(-5.9c\right)$. Data for the three different Laponite® concentrations collapses reasonably well onto a single curve with a scaling $\sim a^{-1.0}$, validating Eq. 2.13 and the values of the constants given above. The collapse also suggests a superposition between probe size and Laponite® concentration, with the product (at_{gel}) remaining essentially constant for a given Laponite® concentration over the range of probe sizes studied here.

2.5 Conclusions and Outlook

Many commercially and biologically relevant fluids exhibit different rheological properties at different length scales as a result of complex microstructure. In this chapter, we have used multiple particle tracking microrheology to explore how rheological properties vary with probe size in an aqueous dispersion of Laponite®, a discotic colloidal clay that forms an aging colloidal gel under appropriate conditions. We have shown that the microrheological properties are dependent on the probe particle size, implying that the dispersion is heterogeneous across different length scales. Probing at smaller length scales results in the observation of lower viscoelastic moduli and a delay in gelation time. We have also proposed a microstructural explanation for these phenomena: as the material ages, a porous network structure develops that traps larger probe particles, while smaller probes generally have more time to diffuse relatively unhindered through pores and more weakly gelled regions. In support of this hypothesis, we observed that the probe dynamics develop significant spatial heterogeneity as the system ages. Analysis of these heterogeneities for different probe sizes indicates a microstructural length scale in the system that is similar to the length scales measured previously by light scattering [45, 103]. In light of these results, it would be interesting to further investigate the microstructural heterogeneities and their associated length scales with two-point microrheology [130]. With this method, the viscoelastic moduli could be explored as a function of probe separation. In addition to heterogeneities, we find that as the system ages the probe particles exhibit correlations between successive displacements, which has been reported to be evidence of microstructural confinement. However, by analyzing trajectories of a Brownian particle in a continuum Kelvin–Voigt material, we find that correlations between successive probe displacements are more directly related to the apparent local elasticity. We propose that a better measure of the microstructual confinement is the length scale at which deviations from a simple linear scaling are observed in these successive correlations. An interesting problem for future work would be to determine the corresponding correlations for probes diffusing in a Newtonian fluid confined by solid walls, which provides a simple model of a porous microstructure. Finally, motivated by the observed probe-size dependence of rheological properties and the proposed microstructural description, we identify a concentration–probe-size superposition, obtaining approximate scalings for the observed gelation time as a function of probe size and Laponite® concentration. The results presented in this chapter will aid in the understanding of the structure and rheology of aqueous Laponite® dispersions. Furthermore, the methods used here may also find broader general application to other structured complex fluids and gels. The methods are particularly suitable for analyzing materials that serve different functions at different length scales, and that as a result must have different rheological properties across length scales. Possible examples include the cell cytoskeleton, which provides structural stability on the length scale of the entire cell, but must also allow macromolecules and vesicles to diffuse within the pores. Finally, the results in this chapter show that multiple particle tracking can provide insight into the structure of evolving materials, even when the system is inhomogeneous at the probe length scale.

Multiple Particle Tracking linear microrheology studies over a range of probe sizes have helped to elucidate the nature of the local gelation behavior and microstructure in dilute aqueous Laponite® dispersions. With this understanding, we now turn to the *nonlinear* microrheological behavior (i.e., high deformation and/or deformation rate) of more concentrated aqueous Laponite® dispersions, which are known to exhibit significant yield stresses on the bulk scale. Since the results from Chapter 2 demonstrate that significant insight can be gained by comparing rheological properties

measured at different length scales, we once again combine bulk rheology and microrheology in order to obtain a better understanding of the microstructure of the dispersions.

CHAPTER 3

Nonlinear Microrheology of Aqueous Laponite Dispersions

In this chapter, we extend microrheology studies to the nonlinear regime, exploring the local shear-thinning and yield stress behavior of more concentrated aqueous Laponite® dispersions using a simple magnetic tweezer device. We find that for sufficient clay concentrations, deviations between bulk and micro-scale rheological properties like those observed in Chapter 2 disappear, implying that the bulk mechanical properties are representative of the local microenvironment of probe particles and that characteristic microstructural length scales decrease as the Laponite® concentration increases. The reader should note that for the remainder of this thesis, the Greek letter τ represents stress, rather than lag time as in Chapter 2. Though this notation is unfortunate, it follows the standard conventions in the field. Beneficially, the lag time variable does not appear in remaining chapters, so this standard notation can be used without excessive confusion. The results presented in this chapter can be found in the following publication [90]: Rich, J. P.; Lammerding, J.; McKinley, G. H.; Doyle, P. S. *Soft Matter* **2011**, *7*, 9933–9943, copyright 2011 by The Royal Society of Chemistry. This work was completed in collaboration with Professor Jan Lammerding, Cardiovascular Division, Department of Medicine, Brigham and Women's Hospital and Harvard Medical School, Cambridge, MA (currently at Cornell University, Department of Biomedical Engineering).

3.1 Overview

The large deformation mechanical response of complex fluids and soft materials provides fundamental insight into their underlying microstructure and dynamics. Additionally, associated yielding and flow processes are often central to industrial processing and end-use. By probing nonlinear rheological properties at the microscopic scale, microstructural dynamics and flow mechanisms can be more directly elucidated. In this chapter, we present a simple magnetic tweezer technique for probing the nonlinear microrheology of complex fluids and soft materials. The setup is characterized in terms of the accessible stresses, the applied magnetic fields, and the measurable viscosities and shear rates. Further, we report the first use of magnetic tweezers to determine yield stresses at the microscopic scale, as well as the first comparison between bulk and micro-scale yield stress measurements. The capabilities of the technique are demonstrated on an aqueous dispersion of Laponite®: an aging, thixotropic colloidal clay of considerable scientific and practical interest. Probe trajectories in this material reflect the yield stress and strong shear-thinning behaviour observed on the bulk scale, and for sufficient clay concentrations we find good agreement for the shear yield stress obtained from bulk rheology and magnetic tweezer measurements. These unforeseeable observations illuminate the nature of the dispersion microstructure, including the characteristic size of microstructural features.

3.2 Introduction

Microrheology has become an important tool for understanding and characterizing soft materials [19]. The field encompasses various methods in which rheological properties are extracted from the motions of embedded microscopic probe particles [24]. It is especially suited for situations where bulk rheometry is not feasible, such as for rare materials or in vivo studies of biological fluids [131], and can provide insight into materials with complex microstructure, which may exhibit different rheological behaviour at bulk and microscopic length scales [21, 22]. Techniques for probing both linear (small deformation and deformation rate) and nonlinear (large deformation and/or deformation rate) microrheology have been developed, with the nonlinear case necessarily involving active techniques in which external forces are applied to probes [24, 21, 132]. While linear microrheology remains important and has received the most attention (see Chapter 2), nonlinear microrheology plays a key role in the flow properties of numerous important microstructured materials, such as colloidal glasses [133], electrorheological and magnetorheological fluids [72, 64], and polymer-colloid mixtures [2]. The bulk response and proper function of these materials is highly dependent on shear-thinning and yield stress phenomena at microscopic length scales. For example, in magnetorheological suspensions, microscopic iron-containing particles are often dispersed in viscoplastic carrier fluids, whose rheological properties prevent particle sedimentation and influence field-responsive assembly [79] (see Chapters 4 and 5).

Because of its significance in understanding the properties of structured fluids, recent work in the field has begun to investigate nonlinear microrheology for several canonical materials, and has explored relationships with bulk properties. A number of studies have examined the micro-scale viscosity of colloidal dispersions [134, 135, 136, 137], the nature of forced microstructural rearrangements and shear melting near the colloidal glass transition [133], and an active microrheological method for measuring normal stress coefficients [138]. Additionally, yield stress measurements at the microscopic length scale were first reported by Wilking and Mason, who examined gelatin

solutions using optical tweezers that were modified to exert torques on an embedded microdisk [139].

In this chpater, a magnetic tweezer technique is presented for measuring nonlinear microrheological properties of complex fluids. The motion of embedded magnetic microparticles has been used for many years to probe such phenomena as the mechanical properties of cell protoplasm [140], the elasticity of gels [141], the stretching behaviour of macromolecules [142], and the mechanotransduction of cells [143]. Here we employ the single-pole design from Lammerding [144], which can apply forces on the order of 10 nN on 4.5 μm superparamagnetic particles. The dynamic range of the instrument is characterized and probe trajectories are analyzed to extract effective viscosity measurements. Additionally, we report the first use of magnetic tweezers to determine yield stresses at the microscopic scale, affording advantages to optical tweezer techniques because of simpler design and implementation. The technique is demonstrated on a typical thixotropic, aging, yield stress material [145], an aqueous dispersion of the synthetic clay Laponite® [42]. A summary of the physical characteristics of Laponite clay particles, as well as a review of the current understanding of the microstructure and rheology of their aqueous dispersions, is provided in Chapters 1 and 2 of this thesis. Additionally, a more thorough review of the phase behavior of aqueous Laponite® dispersions can be found in [43]. Recall from earlier chapters that Laponite® clay consists of nanometric disks that undergo progressive structural arrest over time when dispersed in water at concentrations as low as about 1 wt% [45, 146, 102, 100]. The microstructural development results in complex and time-dependent rheology [106, 147, 148, 107, 59]. Previous work has addressed the bulk rheology and linear microrheology of aqueous Laponite® dispersions (see Chapter 2). We note that while the local nonlinear rheology of aqueous Laponite® dispersions has also been studied [31], only probes with sizes on the order of 1 mm were used. The current work therefore presents the first truly micro-scale nonlinear rheological study of this material, as well as the first comparison to bulk nonlinear properties. We observe that the effective viscosity is strongly shear-thinning, obeying similar power-law behaviour at both the bulk and microscopic scales. Additionally, the yield stress grows approximately logarithmically with age time, exhibiting quantitative agreement between bulk and microscopic scales for concentrations $c \geq 2$ wt%.

3.3 Experimental Methods

The magnetic tweezer device used in the present work was designed and described by Lammerding [144]. A rod of high magnetic permeability iron (CMI-C, CMI Specialty Products, Bristol, CT) is machined to a sharp tip of width ≈ 200 μm, as shown in Fig. 3.1, and subsequently annealed according to the manufacturer's specifications. The highly pointed geometry results in large magnetic field gradients, leading to relatively large forces on magnetic probe particles [32, 149]. The core metal is wrapped with about 300 turns of AWG 19 copper magnet wire over a length of 7.2 cm, leading to a wire turn density n of about $n \approx 4200$ m^{-1}. The assembly is then mounted on a manual micromanipulator (MX110, Siskiyou, Grants Pass, OR) alongside an inverted microscope (Axiovert 40 CFL, Carl Zeiss AG, Oberkochen, Germany) and the wires are connected to a DC power supply (GPS-2303, GWInstek, Taipei, Taiwan). Experiments are conducted at room temperature, $T \approx 22.5$ °C. For a current of 1.5 A, the temperature of the tip does not rise more than about 1 °C over the time scale of a measurement (~ 1 min) [144]. We therefore consider electrical resistance heating of the tip to be negligible. Gaussmeter measurements at the back of the core indicate that the magnetic field stabilizes within 1 s of applying a current.

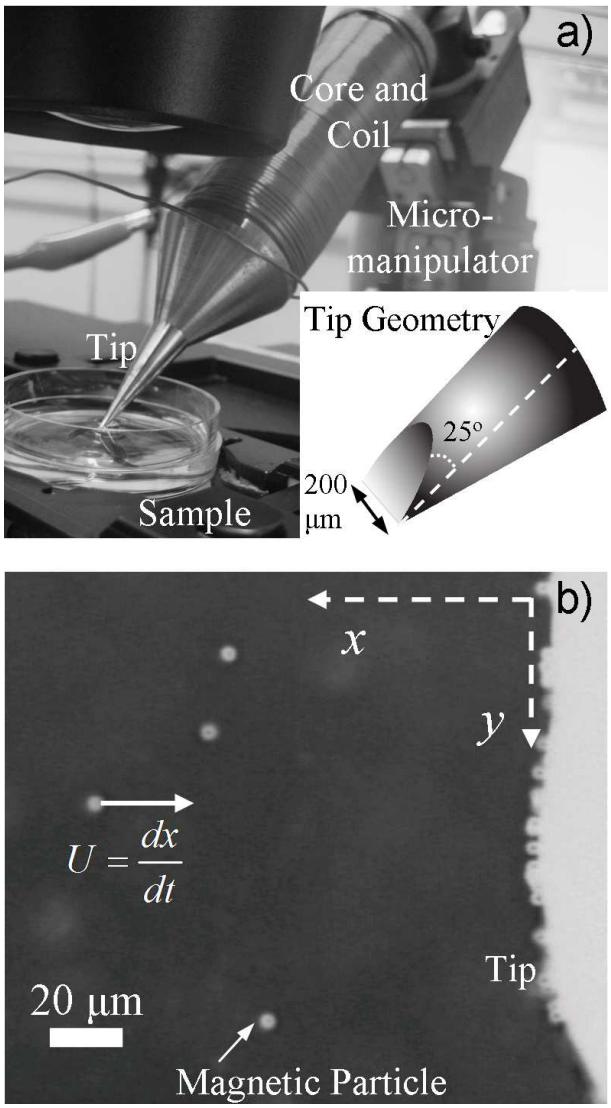

Fig. 3.1: *The magnetic tweezer setup used for nonlinear microrheology experiments. (a) The magnetic tweezer device is mounted on a micromanipulator adjacent to the stage of an inverted microscope. The iron core is machined to a sharp tip, which is dipped directly into the fluid of interest. The flattened tip design, which is shown in detail in the inset, leads to locally horizontal forces when the device is held at an angle of* 45° *to the horizontal [144]. (b) Microscope view frame of the magnetic tweezer experiment. The point of the tip is flattened to a width of about 200 µm, providing an approximately unidirectional magnetic force in the vicinity of the tip. Upon magnetization of the core, superparamagnetic probe particles (diameter* $d = 4.5$ *µm) move towards the tip with a velocity* U*. The distance from a probe to the surface is given by* x*, while* y *defines the distance along the surface of the tweezer device.*

Laponite RD® powder was obtained from Rockwood Additives. Aqueous Laponite® samples were prepared in the same way as descirbed in Section 2.3.1. Immediately following filtration of the aqueous Laponite® sample, superparamagnetic microparticles of diameter $d = 4.5$ μm (M-450 Dynabeads, Invitrogen Life Technologies, Carlsbad, CA) are added at a concentration of about $\phi \approx 0.4$ vol% (see Fig. 1.3 for magnetization properties). The magnetic particle concentration is chosen to achieve a large number of measureable particle trajectories with approximately non-interacting particles. After vortex mixing for about 15 seconds, the magnetic particles are randomly dispersed in the sample. The additional rejuvenation of the sample due to vortex mixing is minimal since it is conducted immediately after filtering. A small petri dish is filled with the dispersion and placed on the microscope stage for visualization with a 20× objective (N.A. = 0.5). By adjusting the micromanipulator, the tip of the magnetic tweezer device is dipped directly into the dispersion and brought arbitrarily close to magnetic probe particles, maximizing the accessible forces on probes [32]. The tip is machined such that approximately horizontal magnetic fields are locally obtained when the device is positioned at a 45° angle to the horizontal, as pictured in Fig. 3.1. The directionality of the force is confirmed by checking that particles remain in focus as they move towards the tip.

Movies of probe particle dynamics are captured with a CCD camera (KP-M1A, Hitachi, Tokyo, Japan) having a variable shutter speed between 1/60 s and 1/10,000 s set to frame integration mode. Scion Image software is used to record movies at a rate of 30 frames/s. Each video frame consists of two interlaced fields (the odd or even rows of the CCD matrix) that are exposed 1/60 s apart, requiring each frame to be de-interlaced during the movie analysis. The interlacing also results in a loss of spatial resolution in the direction perpendicular to the interlacing [26]; thus, particle displacements in this study are only examined in the horizontal direction (the x-direction), which is the predominant direction of motion. Movies are analyzed to obtain particle trajectories using publically available software developed by Crocker and Grier [26]. Any particles that chain or cluster together are neglected in the analysis.

Bulk rheology measurements are made using a stress-controlled rheometer (ARG-2, TA Instruments, New Castle, DE) with a 40 mm diameter aluminium plate geometry and a 0.5 mm gap [see Fig. 1.1(a)]. Adhesive-backed 600 grit sandpaper (McMaster-Carr, Elmhurst, IL, RMS roughness ≈ 6.0 μm), is attached to each surface to minimize wall-slip. The Laponite® dispersion is prepared in the same way as in the microrheology experiments, and is introduced between the plates immediately after filtering, which is again marked as the time of zero age, $t_w = 0$. To help ensure a reproducible initial condition, the sample is then pre-sheared at a shear rate of $\dot{\gamma} = 250$ s^{-1} for 30 s. Though the pre-shear may keep aggregates from forming and partially rejuvenate the fluid [36], we find this additional rejuvenating effect to be negligible when the pre-shear is performed immediately subsequent to the filtration step. After the dispersion is allowed to age at a constant temperature $T = 22.5$ °C, continuous ramp tests are performed to explore the yielding and shear-thinning behavior. Starting from a value below the static yield stress, the applied shear stress is increased continuously until the dispersion has yielded, allowing the extraction of the flow curve and viscosity behaviour during yielding. The stress is ramped linearly at a rate of about 1 Pa/s over a time of 2 min, which is small compared to the age of the dispersion. We note that this protocol estimates the static yield stress, which is the stress required to induce flow from rest, in contrast to the dynamic yield stress, which is estimated by decreasing the shear rate and extrapolating the resulting shear stresses to $\dot{\gamma} = 0$ s^{-1} [17].

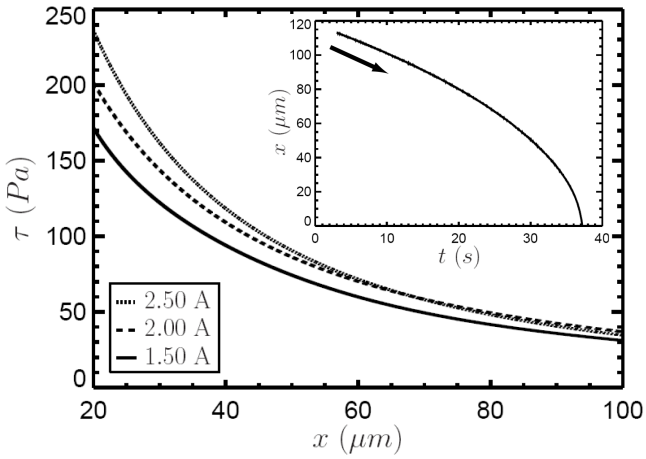

Fig. 3.2: *Calibration curves for the stress applied by the magnetic tweezers as a function of the distance from the tip. Results for $I = 1.50$ A, 2.00 A, and 2.50 A are shown. The stress increases as the tip is approached and stresses up to about 230 Pa are accessible close to the tip. For $x < 20$ μm, the computed stress values are highly sensitive to the order of the polynomial fit to trajectory data. The stress exhibits only weak dependence on current, suggesting that either the core or the probe particles are approaching magnetic saturation. The inset shows a typical probe trajectory in the Newtonian calibration fluid, which has a kinematic viscosity of $\nu = 30{,}000$ cSt ($\eta = 29.5$ Pa·s).*

3.4 Calibration of Magnetic Tweezers

The force and the stress applied by the magnetic tweezer device on probe particles are calibrated by tracking particle motion in Trimethylsiloxy-terminated Polydimethylsiloxane (DMS-T43, Gelest, Morrisville, PA), a Newtonian liquid with kinematic viscosity $\nu = 30{,}000$ cSt (dynamic viscosity $\eta = 29.5$ Pa·s). The reported viscosity was confirmed using bulk rheology measurements. The stress applied by the tweezer device is a function of both the distance from the tip surface, x, and the current in the copper wire, I. About 30 particle trajectories $x_i(t)$ are obtained at a given current and an average trajectory is calculated by applying a least-squares fit. The most suitable fit for the calibration experiments is provided by functions of the form $t_{s,i} - t = P_m(x)$, where $t_{s,i}$ is the time at which the i^{th} particle reaches the tip and P_m is a polynomial of order m ($m = 3$–6). By taking a time derivative of the fit, an expression for the average particle velocity, $U(x)$, is obtained, allowing calculation of the shear rate $\dot{\gamma}(x) = 3|U(x)|/2a$ and the stress $\tau(x) = \eta\dot{\gamma}(x) = 3\eta|U(x)|/2a$, where a is the probe radius. The resulting stress calibration curves for three different values of the current are plotted in Fig. 3.2. Here it is seen that the instrument can impose stresses on probe particles up to about 230 Pa, which provides an upper limit for measureable yield stress values. Additionally, the stress depends only weakly on I over the range explored in the present work, increasing by 10–27% (depending on x) from $I = 1.50$ A to $I = 2.50$ A. The inset of Fig. 3.2 shows a typical probe trajectory in the Newtonian calibration fluid at a current of 2.00 A. A smooth acceleration towards the surface is observed, with $d^2x/dt^2 < 0$ for all x, as a result of

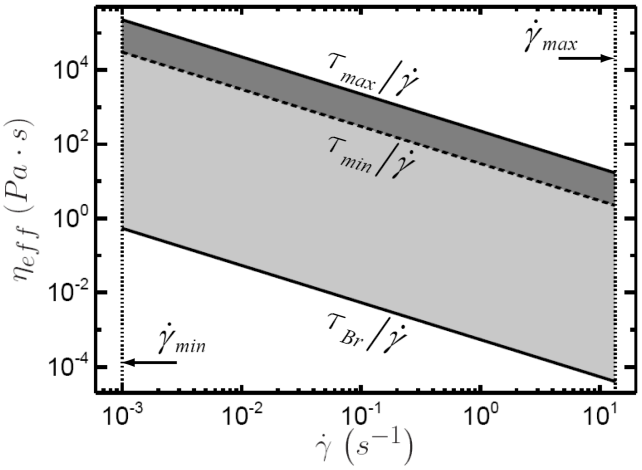

Fig. 3.3: *Operating diagram for the magnetic tweezer setup showing the range of accessible shear rates and viscosities. The maximum shear rate* $\dot{\gamma}_{max} = 3\,|U_{max}|\,/2a$ *is limited primarily by the frame rate of the camera (30 frames/s or 60 interlaced fields/s), which enables particles with diameter* $2a = 4.5\ \mu m$ *to be tracked at velocities up to about* $|U_{max}| \approx 20\ \mu m/s$ *under 20× magnification. The minimum shear rate* $\dot{\gamma}_{min}$ *is given by dividing the spatial resolution (here about 90 nm) by the time over which the magnetic field is applied (here 1 min). The stress calibration in Fig. 3.2 allows calculation of the corresponding accessible viscosities. The dynamic range demonstrated in the present work is given by the dark shaded region, with* $\tau_{max} = 225\ Pa$ *and* $\tau_{min} = 30\ Pa$*, while the lighter region is accessible at lower currents than used here. Eventually, Brownian stresses become significant, providing an ultimate lower limit to the measurable viscosities. Here this limit is calculated using the characteristic Brownian stress* $\tau_{Br} = k_B T/a^3$ *at* $T = 22.5\ ^\circ C$ *on a particle with radius* $a = 2.25\ \mu m$*.*

the constant viscosity and the continually increasing stress on the particle. The magnetic tweezer technique therefore provides a micro-scale analogy to the bulk continuous stress ramp described in the previous section. In Section 3.5.1, we contrast the shape of this trajectory with that in the non-Newtonian case, where effects of shear-thinning behaviour become apparent.

By combining the stress calibration with the limitations of the optical and particle-tracking setup, we construct an operating diagram of the accessible shear rates and viscosities that can be measured by the magnetic tweezer technique. This diagram is shown in Fig. 3.3, in which the range of accessible shear rates is bounded by the dotted lines. Assuming thermal forces are negligible compared to magnetic forces, the lower bound $\dot{\gamma}_{min}$ is given by the spatial resolution (here about 90 nm, as determined from the apparent displacement of immobilized particles at 20× magnification [28]) divided by the duration of the experiment, which in the present work is 1 min. The upper bound $\dot{\gamma}_{max} = 3\,|U_{max}|\,|\,/2a$ is limited by the maximum frame rate of the camera (30 frames/s, or 60 interlaced fields/s), which allows particles to be accurately tracked at velocities up

to about $|U_{max}|| \approx 20$ μm/s under 20× magnification. This highlights a potential modification that could extend the dynamic range of future realizations of the technique through the use of a high-speed camera. The range of measurable viscosities is given by the stress calibration in Fig. 3.2, using the relation $\eta(\dot{\gamma}) = \tau/\dot{\gamma}$. The dark gray area shows the dynamic range demonstrated in the present work, while the lighter region, which corresponds to smaller shear stresses, is accessible at lower currents than used here. At very low currents, the applied stress becomes comparable to the characteristic Brownian stress $\tau_{Br} = k_B T/a^3$. In this limit, particle diffusion out of the area of focus generally makes continual tracking of particle trajectories impossible, so that $\tau_{Br}/\dot{\gamma}$ corresponds to an ultimate lower limit to the measurable viscosities.

Further insight into the capabilities of the technique can be gained by considering the magnetic field applied by the tweezers and the resulting magnetization of the probe particles. While it is difficult to accurately measure the magnetic field, B, at distances of 10–100 μm away from the tip, it can be estimated by combining the calibration data with a suitable model for the particle magnetization, M. We use the Fröhlich–Kennelly equation [150]:

$$M(H) = H\left(\frac{1}{\chi_0} + \frac{H}{M_{sat}}\right)^{-1} \tag{3.1}$$

Here $\chi_0 = 1.6$ is the linear magnetic susceptibility and $M_{sat} = 30$ kA/m $= 19$ emu/g is the saturation magnetization of the particles, both provided by the manufacturer (see Fig. 1.9). H is the magnetizing field. To proceed with analysis, a more manageable functional form for the average trajectory is required. In place of the polynomial form mentioned above, we take a simpler power law form: $x = A(t_{s,i} - t)^{\alpha}$. For $I = 1.5$ A, least-squares fitting gives $A = 23.1$ μm and $\alpha = 0.43$. The particle velocity is then

$$U(x) = -\frac{dx}{d(t_{s,i} - t)} = -A\alpha(t_{s,i} - t)^{\alpha-1} = -A^{1/\alpha}\alpha x^{(\alpha-1)/\alpha} \tag{3.2}$$

where the final equality is in terms of the distance from the tip, x. The drag force is then calculated from Stokes' Law for steady viscous drag on a sphere

$$F_{drag}(x) = -6\pi\eta a U(x) = 6\pi\eta a A^{1/\alpha}\alpha x^{(\alpha-1)/\alpha} \tag{3.3}$$

and the magnetic force is given by Equations 1.7 and 3.1:

$$F_{mag}(x) = \mu_0 V M\frac{dH}{dx} = \mu_0 V H\left(\frac{1}{\chi_0} + \frac{H}{M_{sat}}\right)^{-1}\frac{dH}{dx} \tag{3.4}$$

where μ_0 is the magnetic permeability of free space and V is the particle volume. By summing the drag force and the magnetic force and assuming inertial acceleration is negligible, we obtain a differential equation that can be solved for the magnetizing field H as a function of x.

$$\mu_0 V H\left(\frac{1}{\chi_0} + \frac{H}{M_{sat}}\right)^{-1}\frac{dH}{dx} = -6\pi\eta a A^{1/\alpha}\alpha x^{(\alpha-1)/\alpha} \tag{3.5}$$

Using the condition that $H \to 0$ as $x \to \infty$, Equation 3.5 can be integrated to obtain an expression

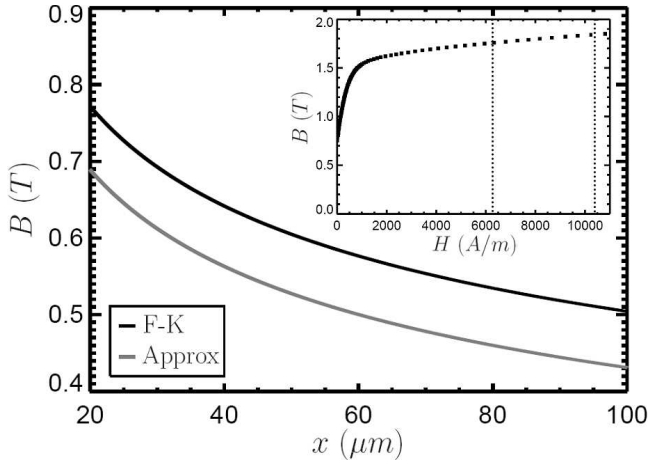

Fig. 3.4: *Calculation of the magnetic field as a function of distance from the tip at a current of $I = 1.50$ A. The black line presents the result obtained from Equation 3.6, which uses the Fröhlich–Kennelly relation in Equation 3.1 to model the particle magnetization. The strength of the field is attributed to the magnetization properties of the CMI-C core metal, shown in the inset with data provided by the manufacturer. The dotted lines bound the range of H values in our experiment, where $H = nI$ and $n \approx 4200$ m^{-1} is the wire turn density of the coil. As a result of the field strengths on the order ~ 1 T, the magnetization of probe particles is calculated via Equation 3.1 to be 28.6–29.1 kA/m, which is very close to saturation. The gray line shows the calculation of the field using the approximation of probe particle saturation $M = M_{sat}$ from Equation 3.7. The result is about 15–20% lower than the values obtained using the Fröhlich–Kennelly relation, though the trend is the same.*

that is explicit in x but implicit in H.

$$x = \left(\frac{M_{sat}^2 \mu_0 V \left(2 - \frac{1}{\alpha}\right)}{6\pi\eta a A^{1/\alpha} \alpha} \right)^{\frac{\alpha}{2\alpha-1}} \left[\frac{1}{\chi_0} \ln\left(1 + \frac{\chi_0 H}{M_{sat}}\right) - \frac{H}{M_{sat}} \right]^{\frac{\alpha}{2\alpha-1}} \tag{3.6}$$

This expression is plotted in Fig. 3.4 (black line) in terms of the magnetic field $B(x) = \mu_0 H(x)$ for $I = 1.50$ A. Within 100 μm of the tip, the magnetic field acting on magnetizable probe particles is of the order ~ 1 T, which is consistent with the magnetization properties of the CMI-C core metal shown in the inset. The magnetic field decays with increasing distance from the tip, dropping by about 35% over a distance from $x = 20$ μm to $x = 100$ μm. This field gradient leads to a magnetic force on the probe particles according to Equation 3.4. The resulting probe particle magnetization values, calculated from Equation 3.1, are 28.6–29.1 kA/m, so that $M \approx M_{sat} = 30$ kA/m. This near-saturation provides an explanation for the marginal difference between stress calibration curves at different currents shown in Fig. 3.2. If $M \to M_{sat}$, the particle force balance

results in a simpler relation between H and x.

$$H = \frac{6\pi\eta a\alpha^2 A^{1/\alpha}}{\mu_0 V M_{sat}\left(1-2\alpha\right)} x^{\frac{2\alpha-1}{\alpha}} \tag{3.7}$$

Equation 3.7 is shown by the gray line in Fig. 3.4. Though this expression provides physical insight, Fig. 3.4 shows that it is not as suitable for quantitative analysis since it underestimates the field by about 15–20% compared to Equation 3.6. These calculations imply that larger stresses could be achieved by using probe particles with a higher saturation magnetization.

A final important consideration is the variation in the applied stress across the lateral plane of the tip [see Fig. 3.1(b)]. Roughness and edge effects on the microscopic scale could lead to significant deviations at different values of y, especially when the probes are very close to the tip at small values of x. Because the coefficient of variation for the probe size is less than 5% (manufacturer information), and it has been claimed that deviations in magnetic properties are largely due to size polydispersity [151], these irregularities in tip geometry are expected to be the primary source of variations in the applied stress. To explore this effect, probe particles are binned according to their position along the y-axis, as shown in the inset in Fig. 3.5(a). For each bin j, an average trajectory is obtained by applying a least-squares fit to a polynomial as described above, allowing calculation of an average velocity function $U_j\left(x\right)$ and a shear stress-distance calibration curve, $\tau_j\left(x\right) = \eta\dot{\gamma}\left(x\right) = \eta\left|U_j\left(x\right)\right|/a$. At least 5 individual trajectories are averaged per bin. The calibration curves for $I = 2.00$ A are shown in Fig. 3.5(a), and we find that the variation across the lateral plane of the tip becomes increasingly significant at closer distances. This is also seen in Fig. 3.5(b), where the applied stress is plotted as a function of y at various values of x. Beyond a distance of $x \approx 40$ μm, the applied shear stress is essentially constant across the tip. In particular, the coefficient of variation at $x = 20$ μm is about 10%, and so we limit our quantitative experiments to distances beyond this value. This calibration indicates that improvements on this technique could be achieved by decreasing the variation across the tip through more precise micromachining. This would increase the upper bound of practically accessible stresses while maintaining the experimental error within reasonable limits.

3.5 Nonlinear Microrheology Results and Discussion

Having discussed the instrument calibration and associated considerations, we now apply this magnetic tweezer device to the examination of the nonlinear microrheology of an aging, thixotropic, microstructured yield stress material: a colloidal clay composed of an aqueous dispersion of Laponite®. The nonlinear rheology of aqueous Laponite® dispersions has been studied at the bulk scale [148, 107], but has never been examined at scales below $\sim$ 1 mm [31]. In addition to shear-thinning behaviour, we present the first magnetic tweezer measurements of yield stresses at the microscopic scale. Since microstructural length scales are expected to be on the order of the probe size [103], it is unclear a priori whether micro-scale yield stress results will match those obtained from bulk rheology [22, 110].

3.5.1 Probe Trajectories

Bulk rheology experiments on aqueous Laponite® dispersions have showed a sharp decrease in viscosity at a critical applied stress (i.e., the static yield stress), providing clues as to the expected

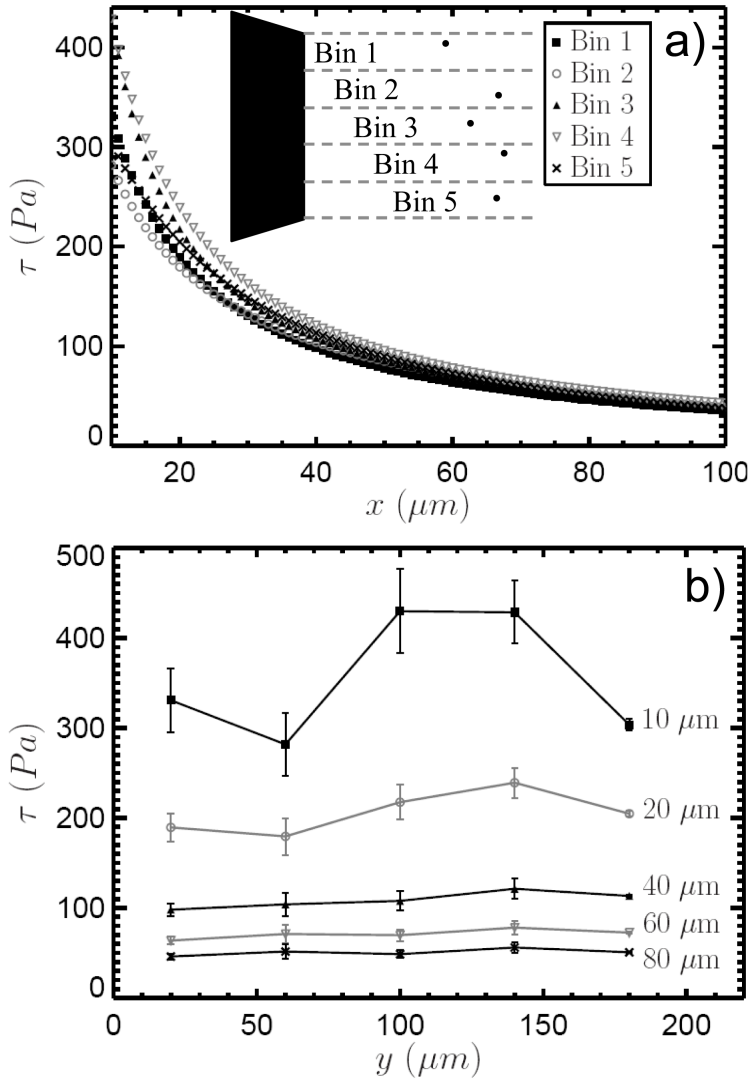

Fig. 3.5: *Lateral variation in the applied stress across the surface of the tweezer device. (a) Stress calibration data is plotted at $I = 2.00$ A with particle trajectories partitioned into five bins according to their positions along the y-axis, as shown in the inset. Though the applied stress becomes approximately uniform far from the tip, local variations in the tip geometry lead to deviations in the stress as the tip is approached. This is clarified in (b), where the applied stress is re-plotted as a function of y at five distances from the tip. Error bars represent the standard error between individual trajectories. In order to neglect non-uniformities in the stress across the surface, we limit our analysis to distances beyond $x = 20$ μm, where the coefficient of variation is less than 10%.*

shape of probe particle trajectories in our experiment [36, 35]. If a probe particle is close enough to the tip to exceed the yield stress, we expect the viscosity in the vicinity of the particle to decrease significantly as a result of the disruption of the microstructure due to the applied stress (i.e., local rejuvenation, or shear melting). This would lead to even greater mobility of the particle so that it moves more easily towards the tip to a region of even higher stress, causing an even further decrease in the local viscosity. The resulting trajectories will exhibit rapid acceleration towards the tip surface, reflecting the avalanche behavior of thixotropic yield stress fluids described by previous authors [152]. In contrast, the stress on particles farther from the tip will not be sufficient to break the yield stress of the surrounding fluid, so those particles are expected to remain stationary. Fig. 3.6(a) shows five typical probe trajectories in a 2.0 wt% Laponite® dispersion at an age time of $t_w = 2$ h. The current is $I = 2.00$ A. The trajectories are generally consistent with the expectations described above, with a few additional features that merit explanation. We first note that the bottom three trajectories do reach the tip surface ($x = 0$); however, some data is lost because for $x \leq 22$ μm, the particles move too fast to be tracked at 30 frames/s. Therefore, some probe particles reach the tip surface during the experiment and others, which generally begin farther away, do not. The most prominent feature of the 'mobile' trajectories is their rapid acceleration toward the tip upon reaching a critical separation (or stress), which in this case is about $x = 32$ μm (corresponding to a stress of about $\tau = 135$ Pa). This observation is in agreement with our expectations as described above, and is in contrast to the smooth trajectories observed in the Newtonian calibration fluid. Prior to this rapid acceleration there is a region in which $d^2x/dt^2 > 0$, indicating a slight slowing of the probe velocity. Though this behaviour is not explored in detail in this communication, our present contention is that it is a result of effective 'jamming' of the dispersion microstructure, while $d^2x/dt^2 < 0$ indicates a Newtonian or shear-thinning response. The 'immobile' trajectories, while never reaching the tip surface, do exhibit measurable displacement. This slow creep and eventual plateau toward the end of the experiment, indicates an elastic response and may also be a result of microstructural jamming. Whether or not creeping probes eventually break the yield stress and accelerate rapidly toward the tip depends on the balance between the stress on the particle, which slowly increases as the particle creeps, and the rheological aging process, which results in a continual increase in the static yield stress and the effective viscosity of the unyielded state [36, 153]. Spatial heterogeneity in the dispersion rheological properties may also play a role [89] (See Chapter 2). Since the material properties of the dispersion evolve with age time, it is expected that changes will be observed in the probe trajectories as the material undergoes aging. This is demonstrated in Fig. 3.6b, where typical trajectories of mobile particles are shown for a 1.5 wt% Laponite® dispersion at four different age times and a current of $I = 2.00$ A. As the material ages and the microstructure develops, the static yield stress is expected to increase. As a result, we observe that the separation distance at which probes accelerate rapidly towards the surface decreases with age. Or equivalently, the critical stress of rapid acceleration *increases* with age, here going from about 30 Pa at $t_w = 30$ min to about 60 Pa at $t_w = 1.5$ h.

3.5.2 Shear-thinning Viscosity

In order to extract nonlinear rheological information from the trajectories in Fig. 3.6 it is necessary to calculate particle velocities. Because the trajectories in Laponite® dispersions exhibit sharp features not observed in the Newtonian case, a global polynomial or power law fit as described for the calibration is insufficient for an accurate determination of the velocity at each value of x.

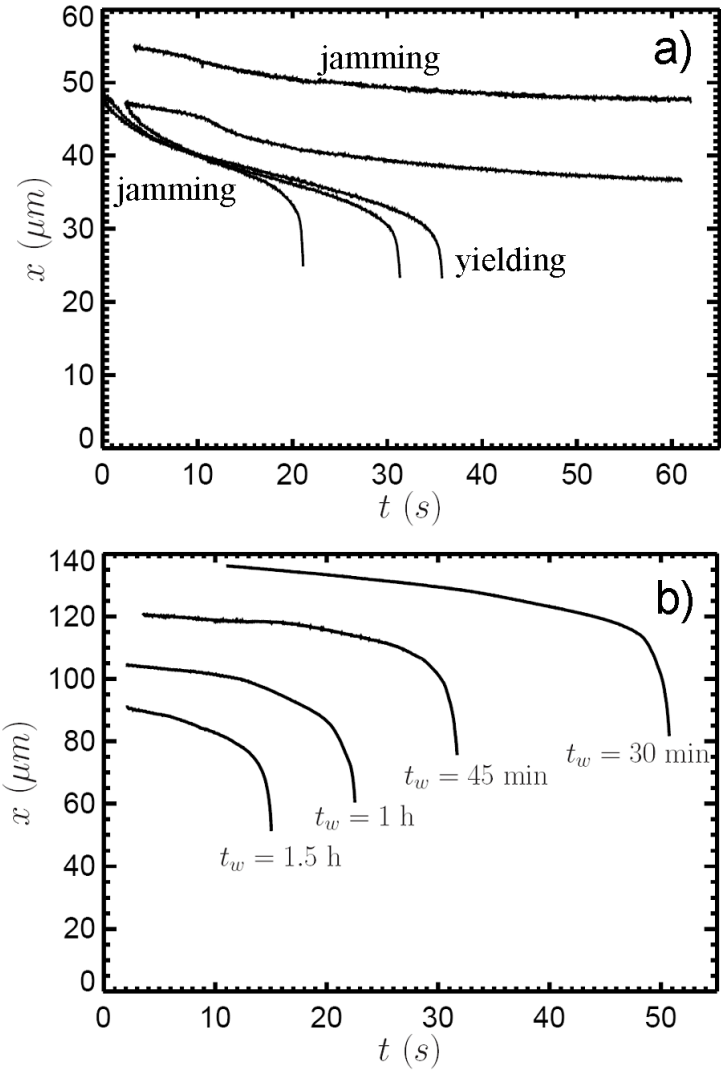

Fig. 3.6: *Probe trajectories in Laponite® dispersions. (a) Five typical trajectories are shown in 2.0 wt% Laponite® at an age time of $t_w = 2$ h with current $I = 2.00$ A. Some particles, generally those beginning closer to the tip, accelerate rapidly toward the surface ('mobile' particles), moving too fast to be tracked for small x. Others remain at a finite separation over the course of the experiment ('immobile' particles). The initial slowing of both populations of probes is suggested to be a result of 'jamming' of the dispersion microstructure, while the eventual rapid acceleration of mobile particles is a result of strong shear-thinning behavior upon yielding. (b) Typical trajectories of mobile particles are shown for different age times in 1.5 wt% Laponite®. As the material ages and undergoes structural arrest, the critical separation at which the particles accelerate rapidly towards the surface decreases, indicating that the critical value of the local stress required to induce flow increases with age.*

Instead, a piecewise cubic spline is used to interpolate the data with a differentiable function. To decrease the noise in the trajectories, a smoothing algorithm is first applied using the MATLAB 'smooth' function with a local weighted linear least squares regression and a 1st degree polynomial model (i.e., the 'lowess' method). Sufficient smoothing is attained by setting the span of the local regression to about 2% of the data. Subsequently, a cubic spline is applied and differentiated to obtain the particle velocity $U(x)$, which is related to the shear rate $\dot{\gamma}(x) = 3|U(x)|/2a$. Combining this with the calibration for the stress $\tau(x)$ allows calculation of an effective micro-scale viscosity, η_{micro}:

$$\eta_{micro} = \frac{\tau}{\dot{\gamma}} = \frac{2a\tau}{3|U|} \tag{3.8}$$

The shear rate dependence of the effective viscosity for a 1.5 wt% dispersion is shown at three different age times in Fig. 3.7. The applied current is $I = 2.00$ A. Here magnetic tweezer microrheology results (solid symbols) are compared directly with bulk rheology data (open symbols) obtained from continuous stress ramp tests. At both bulk and microscopic length scales, the effective viscosity exhibits a power law dependence on the shear rate, $\eta_{eff}(\dot{\gamma}) \propto \dot{\gamma}^p$. The material is very strongly shear-thinning, with $p_{micro} \approx -0.89$ and $p_{bulk} \approx -0.95$. This result may reflect the open microstructure of the dispersion. At 1.5 wt% (≈ 0.6 vol%), the dispersion is mostly water, so that when the microstructure is disrupted and the material begins to flow, the viscosity is expected to decrease sharply and approach that of water. The power law exponents at both length scales are essentially independent of age time, an observation we attribute to the common microstructural states realized during the aging-rejuvenation process and the (age time)–(shear stress) superposition described by Joshi and Reddy [148]. That is, when a dispersion at long age times undergoes shear melting, it passes through many of the same states during rejuvenation as a dispersion at shorter age times.

The correspondence between the power law exponents for bulk and micro-scale measurements is consistent with calculations that reveal similar shear-thinning behavior between the micro- and macroviscosity in colloidal dispersions of spherical particles [134]. Additionally, it indicates that the nature of the shear melting process in Laponite® dispersions is similar at bulk and microscopic length scales. In both cases, the interactions between Laponite® platelets result in an arrested microstructure that must be disrupted, either locally or globally, for the material to flow. The observation that $p_{micro} \approx p_{bulk}$ is in spite of fundamental differences between the character of the two flows. The bulk viscosity measurement is extracted from a viscometric shear flow between parallel plates, whereas the micro-scale viscosity is obtained from flow past a sphere. Despite the similarity between p values across length scales, the magnitude of the effective bulk scale viscosity, η_{bulk}, is about 2–6 times η_{micro} for all shear rates and age times. This observation is qualitatively consistent with linear rheological measurements in aqueous Laponite® dispersions, which indicate a weaker gel (lower viscoelastic moduli and longer gelation times) at microscopic length scales [59, 89] (See Chapter 2). As in the linear case, the discrepancy is likely due to microstructural features in the dispersion, such as pores or clay particle clusters, that exhibit characteristic sizes similar to the probe size, so that microrheology reflects the mechanical properties of a slightly different structure than bulk measurements.

Before leaving this discussion, it is important to address the unsteady nature of the flows from which the viscosity data in Fig. 3.7 is extracted. Because the stress is continually increasing in both the bulk and micro-scale experiments, it may be inappropriate to consider the viscosity values as steady-state measurements. For similar Laponite® systems, the stress relaxation time scale, λ,

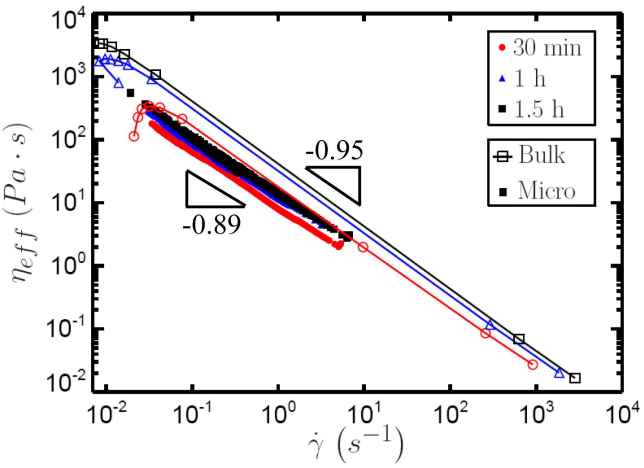

Fig. 3.7: *Effective viscosity as a function of shear rate for 1.5 w% Laponite® at three age times. Results from bulk stress ramp tests (open symbols, with lines added to guide the eye) and microrheology (solid symbols) are shown, with both exhibiting strong shear-thinning behavior. A current of* $I = 2.00$ *A is used for the magnetic tweezer experiments. The effective viscosity follows approximately a power law dependence on shear rate,* $\eta_{eff}(\dot{\gamma}) \propto \dot{\gamma}^p$*, and the observed power law exponents are essentially independent of age time, having values of* $p_{micro} \approx -0.89$ *and* $p_{bulk} \approx -0.95$*. The correspondence between the power law exponents at bulk and microscopic scales suggests commonality in the nature of the shear melting process. The magnitude of the viscosity increases with age time, but is consistently 2 to 6 times smaller on the microscopic scale, in qualitative agreement with previous work comparing the linear viscoelastic moduli of Laponite® dispersions from bulk- and micro-rheology measurements [59, 89].*

was measured to be on the order of ~ 100 s [154], which is large compared to the current shearing time scale $1/\dot{\gamma}$. In other words, the Deborah number, De, is large for the experiments in Fig. 3.7: $\mathrm{De} = \lambda\dot{\gamma} \gg 1$. For this aging system with continually evolving microstructure and rheological properties, however, it is unclear how to measure bulk steady-state viscosity values in the traditional sense. In particular, if such an experiment could even reach steady-state it would likely take significant time, prohibiting the study of age-time dependence. This was demonstrated by Abou *et al.* [107], who performed bulk creep tests on Laponite® dispersions of similar concentration and ionic strength as in the present study. They found that reaching steady state requires exceeding a critical shear stress and shearing for times on the order of hours. With this method, they measured steady-state viscosities over the range of shear rates $50\ \mathrm{s}^{-1} \leq \dot{\gamma} \leq 5000\ \mathrm{s}^{-1}$ and found a shear-thinning power law of $p \approx -0.6$, which is clearly not as strongly shear-thinning as the data in Fig. 3.7. This discrepancy further suggests that effects of the unsteady nature of the flows may be present, and so we qualify our results as 'effective' viscosities. However, because of the continuous ramping of the shear stress in both cases, the bulk and micro-scale measurements reported in Fig. 3.7 are still considered to be analogous to each other.

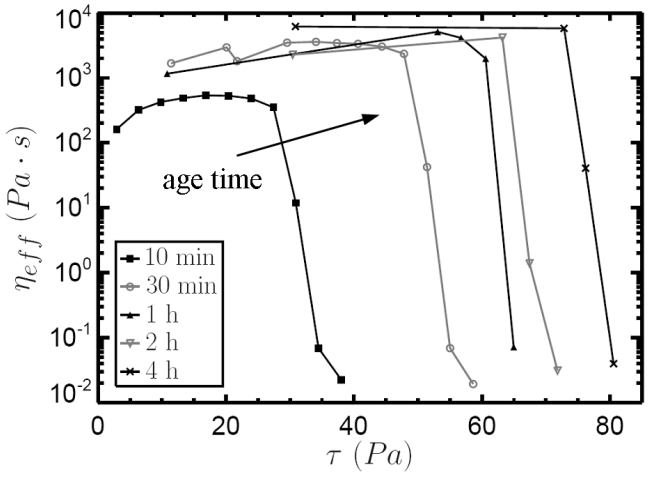

Fig. 3.8: *Effective viscosity as a function of applied shear stress from bulk continuous stress ramp tests on 2 w% Laponite®. Results are shown at five different age times. At a critical stress, the viscosity exhibits a sharp drop over several orders of magnitude, a phenomena associated with a yield stress on the bulk scale. This critical stress increases with the age time. We note that because the stress in each test is ramped continuously over 2 min, the reported viscosity values do not correspond directly to steady-state measurements.*

3.5.3 Yield Stress

At higher Laponite® concentrations, the yield stress becomes a very prominent rheological feature. For example, after aging for about 1 hour, dispersions with concentrations of about 2.5 wt% or more do not flow when the recipient is overturned. Bulk stress ramp tests performed on a 2.0 wt% Laponite® dispersion support the notion of a significant yield stress. Effective viscosity data for these experiments as a function of the applied shear stress is shown in Fig. 3.8 at five different age times. The sharp decrease in viscosity at a critical stress is indicative of a yield stress, which we estimate as the stress at which the viscosity exhibits an intermediate value between its pre- and post-yielded viscosities. We note that the viscosity values reported in the pre-yielded state ($\sim$ 1000 Pa·s) may be somewhat artificial and may depend strongly on the experimental protocol, so that they do not necessarily reflect a true, high-viscosity, fluid state [16].

Magnetic tweezer measurements of the yield stress at the microscopic scale are based upon the distinction between 'mobile' and 'immobile' probe particles as described in Section 3.5.1. Mobile particles break the yield stress and cause shear-thinning of the surrounding fluid, eventually reaching the tip. Immobile particles exhibit a slow creep, but their trajectories plateau and they remain separated from the tip. The x value that separates the shear-thinning region from the creep region can be considered a yield surface. More specifically, the yield stress, τ_y, is bounded by the minimum stress on mobile particles and the maximum stress on immobile particles. That is, if x_{mobile} is the farthest distance from the tip for mobile particles and $x_{immobile}$ is the shortest distance from the tip for immobile particles, then $\tau\left(x_{mobile}\right)$ and $\tau\left(x_{immobile}\right)$ are bounds on τ_y and we take τ_y as

the average of $\tau(x_{mobile})$ and $\tau(x_{immobile})$. One would expect that $x_{mobile} < x_{immobile}$, so that based on the calibration in Fig. 3.2, $\tau(x_{mobile}) > \tau(x_{immobile})$. However, we typically observe $x_{mobile} > x_{immobile}$ as a result of the creeping of immobile particles over the course of a measurement. This is demonstrated in Fig. 3.6(a), in which one of the immobile particles eventually creeps past the initial position of a mobile particle, and yet remains far from the tip. This observation is likely a result of a small amount of aging during a single measurement, as well as spatial heterogeneity in the dispersion rheological properties. Another consequence of the creep behaviour is that the experimental time (i.e., the time over which the current is applied) must be kept constant; otherwise immobile particles may creep varying distances for different experiments, resulting in inconsistent calculations of τ_y. We maintain the experimental time at 1 min.

Yield stress measurements as a function of age time are plotted in Fig. 3.9 for three Laponite® concentrations. Bulk rheology data (gray open symbols) and magnetic tweezer measurements (black solid symbols) are directly compared. The reproducibility of the data is demonstrated by the error bars, which represent the standard error of measurements on three different samples at each age time. In agreement with previous work on the rheology of Laponite® dispersions [147, 31], as well as other microstructured aging materials [155, 156], the yield stress grows approximately logarithmically with age time according to the function

$$\tau_y = \beta \ln\left(\frac{t_w}{t_m}\right) \tag{3.9}$$

where β is a constant (assumed to be independent of Laponite® concentration) and t_m is interpreted as a time scale for microstructural development that can be concentration-dependent. Gray and black solid lines in Fig. 3.9 show least-squares fits to Equation 3.9 at bulk and microscopic scales, respectively, for each concentration. Equation 3.9 generally provides a good fit to the experimental data, although it is a somewhat poor approximation (with coefficient of determination $R^2 = 0.72$) for the magnetic tweezer data at 1.5 wt%. A power law fit was also examined, with a power law exponent that is independent of length scale and concentration, but only marginal improvement in the overall quality of the fit is observed when the additional adjustable parameter is taken into account. That is, we find $R^2_{adj} = 0.95$ for the power law fit and $R^2_{adj} = 0.93$ for the logarithmic fit, where R^2_{adj} is an adjusted R^2 value that corrects for the number of model parameters [157]. The logarithmic fits yield β values of $\beta_{bulk} = 15.3$ Pa and $\beta_{micro} = 23.2$ Pa. The fitted t_m values are plotted as a function of Laponite® concentration, c, in Fig. 3.9(d). We observe that t_m decreases exponentially with c (i.e., linearly on semi-log scale), indicating that dispersions of higher concentration undergo faster structural arrest. Additionally, as the Laponite® concentration increases, bulk and micro-scale t_m values converge.

While quantitative agreement between bulk and micro-scale yield stress data is observed for the lowest Laponite® concentration of 1.5 wt% up to $t_w = 200$ min, the micro-scale data systematically provides higher values for the yield stress compared to measurements from bulk shear for higher concentrations. To interpret these results, it is important to consider the differences between the flow kinematics for the bulk and micro-scale experiments [158]. Only shear stresses are applied in the bulk plate-plate experiment, while the fluid experiences both shear and normal stresses at the surface of magnetic probe particles. Since yield stress materials generally exhibit resistance to both shear and normal stresses, it is reasonable that an elevated yield stress might be observed from magnetic tweezer measurements. A more appropriate comparison of the data can be achieved

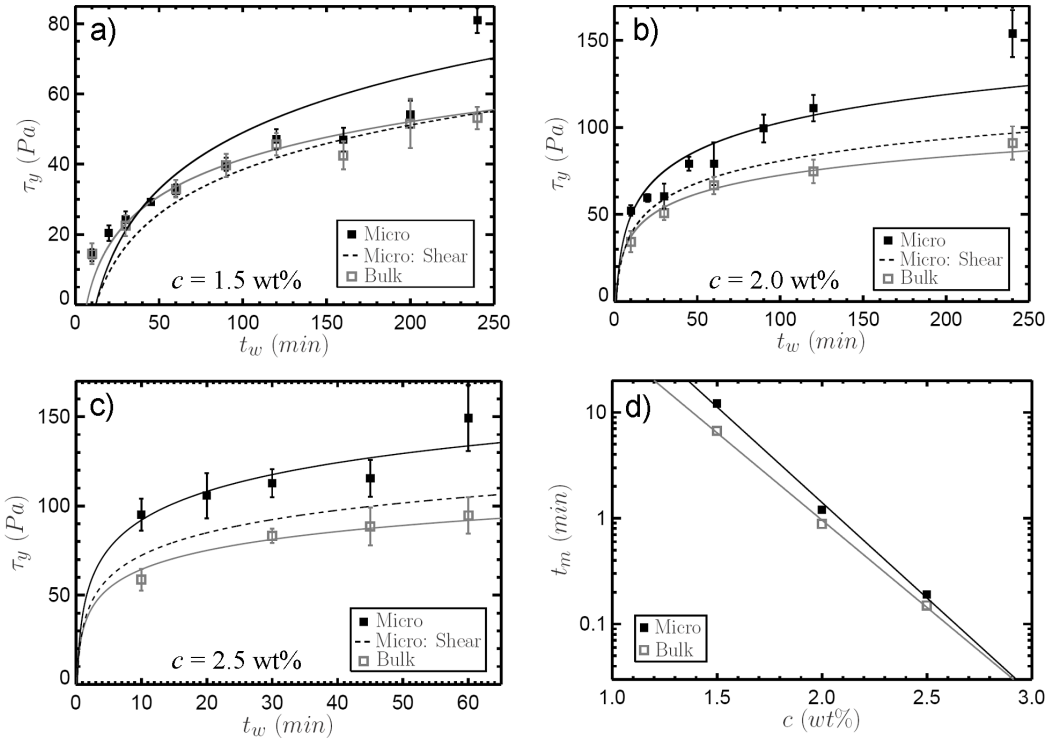

Fig. 3.9: *Comparison of yield stress measurements at bulk and microscopic scales. The age-time dependence of the observed yield stress is shown for Laponite® concentrations of (a) 1.5 wt%, (b) 2.0 wt%, and (c) 2.5 wt%. Error bars represent the standard error of measurements on three different samples at each age time. For all concentrations, the yield stress measured at both length scales grows approximately logarithmically with age time according to Equation 3.9, although this is a somewhat poor approximation for the micro-scale data at 1.5 wt% ($R^2 = 0.72$ for 1.5 wt% micro-scale data). Fits to this functional form are shown by lines in black (micro) and gray (bulk). While there is good agreement between the bulk and raw microrheology data for the lowest concentration up to $t_w = 200$ min, the raw micro-scale data provides higher values for the yield stress compared to measurements from bulk shear for 2.0 and 2.5 wt% Laponite®. However, by treating the pre-yielded material as a linear elastic solid and approximating the shear contribution to the applied stress for the microrheology experiments, quantitative agreement with the bulk yield stress measured in shear can be recovered for concentrations $c \geq 2.0$ wt%. This approximate shear component of the micro-scale applied stress is $\pi/4$ times (78.5%) the measured average stress based on the total force and the probe surface area in the magnetic tweezer experiment and is given by the dashed black line. The characteristic time scales t_m, which are related to microstructural development and are extracted by fitting the bulk and micro-scale data to Equation 3.9, decrease exponentially with Laponite® concentration, as shown in (d).*

by considering only the shear component of the stress. Without knowledge of the flow kinematics, however, an exact expression for the shear stress in the micro-scale experiment is unavailable. As an approximation, we treat the pre-yielded fluid as a linear elastic medium. In this case, the Rayleigh analogy between viscous flow and the linear elastostatics of isotropic, incompressible solids dictates that the stress distribution around the probe sphere is the same as that for Newtonian creeping flow past a sphere [159, 160], for which the shear stress distribution is

$$\tau_{shear}(\theta) = \left(\frac{3\eta U}{2a}\right)\sin\theta \tag{3.10}$$

where θ is the inclination angle measured from the axis of the sphere velocity U [161]. By integrating Equation 3.10, the average shear stress at the surface of the sphere is found to be $\tau_{shear} = 3\pi\eta U/8a$, which is $\pi/4$ times (78.5%) the average stress based on the total force (Stokes drag, $|F| = 6\pi\eta a\,|U|$) divided by the sphere surface area, $\tau = 3\eta U/2a$. Using this result from linear elastic kinematics to approximate the contribution of shear stresses, we therefore shift the logarithmic fits to the micro-scale data down by a factor of $\pi/4$. These shifted results, shown as black dashed lines in Fig. 3.9, exhibit closer agreement with bulk shear yield stress data and a β value of $\beta_{shear} = 18.2$ Pa. However, the correspondence between bulk and micro-scale data at 1.5 wt% Laponite® breaks down when considering only the shear contribution to the stress; the apparent agreement of the black dotted line with the bulk measurements is an artefact of the questionable fit of the magnetic tweezer data to Equation 3.9 at this concentration.

We note briefly that the problem of a sphere moving through the simplest model yield stress fluid, a Bingham plastic, was previously considered by Beris *et al.* using finite element analysis [162]. In this work, an expression is proposed that relates the yield stress to the critical applied force, F, necessary to induce flow: $\tau_y = 0.143F/\left(2\pi a^2\right)$. Applying this expression to our magnetic tweezer data results in micro-scale yield stresses that are about 40-50% of bulk measurements. This discrepancy is not necessarily surprising, however, since the Laponite® dispersion does not strictly obey the Bingham model, but exhibits both pre-yield elastic deformation and post-yield shear-thinning and 'rejuvenation' (see Figs. 3.6 and 3.7).

The correspondence, or lack thereof at low concentrations, between bulk and micro-scale rheology is related to the characteristic size of microstructural features in the dispersions, such as pores and other microstructural heterogeneities, as compared to the length scale that is probed. For dispersions of similar concentration and ionic strength, Pignon *et al.* studied the physical structure of Laponite® dispersions by combining small-angle X-ray and neutron scattering with static light scattering [103, 104]. With this method, they obtained the scattering curve over five orders of magnitude in length scale. Their results indicate that the microstructure consists of a fractal network of loosely-connected clusters having a characteristic size of about 5 μm. At larger length scales, the dispersion appears homogeneous. We therefore expect that probing at length scales significantly larger than 5 μm would result in data that match bulk measurements. Results for smaller probes will primarily reflect the rheological properties on the length scale of the probe size. Since the largest microstructural length scale is on the same order of magnitude as the probe size in the present work, we do not necessarily anticipate that bulk rheology and microrheology results will match, though we might expect them to be close. It is reasonable to expect that the characteristic pore size will shrink as the dispersion concentration is increased. Such a trend in the size of microstrucutral features may account for the fact that better agreement is observed be-

tween the bulk and the appropriately shear-corrected magnetic tweezer measurements for the more concentrated dispersions of 2.0 wt% and 2.5 wt%. Multiple particle tracking linear microrheology experiments in aqueous Laponite® dispersions have also suggested that the characteristic pore size decreases with age time, based on the delay in the apparent gelation time observed with decreasing probe particle size [89] (see also Chapter 2). This could provide an explanation for the eventual increase in the micro-scale yield stress for the 1.5 wt% dispersion at the longest age time, at which point the shear contribution to the stress corresponds reasonably well with the bulk measurement.

3.6 Conclusions and Outlook

Nonlinear rheology is critical to the processing and end-use of many industrially relevant materials, as well as in numerous settings in nature and biology. In many of these situations, micro-scale dynamics play a key role; however, methods for quantitatively probing nonlinear microrheology are only recently being developed. In this chapter, we have discussed a simple magnetic tweezer technique for studying the nonlinear microrheology of complex fluids. The instrument can apply magnetic fields on the order of ~ 1 T, leading to stresses up to about 230 Pa on 4.5 μm superparamagnetic probe particles. Shear rates up to about 10 s^{-1} and viscosities up to about 105 Pa·s can be measured. The experimental error is controlled by limiting measurements to probe separations beyond 20 μm, where the variability in the magnetic force across the tip of the tweezer device is less than 10%. Improvements to the technique and the experimental setup could be achieved through more precise machining and the use of a high-speed camera.

The technique has been demonstrated on an industrially and scientifically relevant aging and thixotropic yield stress fluid: an aqueous dispersion of the synthetic clay Laponite®. 'Mobile' and 'immobile' probe trajectories were observed, reflecting a distinction between probes that overcome the yield stress of the material and those that experience insufficient stress to cause flow. By analyzing 'mobile' probe trajectories, the effective micro-scale viscosity was determined as a function of the shear rate. The Laponite® dispersion was found to exhibit strong shear-thinning behavior, a feature extracted from the rapid acceleration of probes towards the tip and associated with microstructural disruption and shear melting. The shear-thinning behavior was corroborated by bulk measurements, which exhibited similar power law results despite differences in viscosity values by a factor of about 2 to 6. Furthermore, the distinction between 'mobile' and 'immobile' probe trajectories has provided a basis for the first use of magnetic tweezers to directly and quantitatively measure yield stresses at the microscopic scale. When the approximate shear contribution to microrheology results was isolated, bulk and micro-scale yield stress measurements were found to agree quantitatively for Laponite® concentrations of 2.0 wt% or higher, with both exhibiting an approximately logarithmic growth with age time. The age-time dependence of the yield stress has revealed a time scale associated with microstructural development, which we have found to decrease with Laponite® concentration.

It is expected that nonlinear bulk and micro-scale rheology results will agree if probe particles are large compared to the characteristic length scale of microstructural features in the dispersion [22]. An interesting problem for future work would be to determine the probe size at which the bulk-micro agreement observed in Figs. 3.9(b) and 3.9(c) breaks down. This would provide insight into the microstrucural length scales in those dispersions. Further, does agreement break down at all age times, or might the measurements coincide at long enough age times? Our current contention is that measurements with smaller probes in 2.0 or 2.5 wt% Laponite® would likely follow similar

behaviour as the data in Fig. 3.9(a), and that a concentration–(probe-size) superposition would exist, as in the linear rheology case [89] (see Section 2.4.5).

The methods and tools presented here will aid in the micro-scale characterization of complex fluids and soft materials, providing new insight into the microstructure and mechanical response of such materials as polymer gels, colloidal glasses, and biological tissues. Additionally, this work will enable a more complete rheological characterization of materials that are difficult to obtain in large quantities, like certain biofluids. Finally, the results of this chapter will further the understanding of aqueous Laponite® dispersions, which have become important model thixotropic materials in industry and in academic studies.

Chapters 2 and 3 represent a thorough characterization of the time-evolution of the micro-scale rheological properties of aqueous Laponite® dispersions at dilute and moderate concentrations in the linear and nonlinear regimes. In the following chapter, we examine magnetorheological suspensions in a yield stress matrix fluid consisting of an aqueous Laponite® dispersion. The microrheology results from Chapters 2 and 3 provide insight into the local microenvironment of magnetic particles in this composite magnetorheological suspension.

CHAPTER 4

Magnetorheology in an Aqueous Laponite Matrix Fluid

With an understanding of the rheology of aqueous Laponite® dispersions on bulk and microscopic scales, we now explore the use of these materials as novel matrix fluids in magnetorheological (MR) suspensions. The benefit of using aqueous Laponite® dispersions in this setting is that the micro-scale yield stress behavior of the matrix fluid serves to prevent sedimentation of suspended magnetic particles, which is an important concern in numerous commercial applications of MR fluids. Our studies focus on the effect of this yield stress on the field-responsive magnetorheology. An article describing this work has been submitted to the journal *Rheologica Acta* [91].

4.1 Overview

Field-induced static and dynamic yield stresses are explored for MR suspensions in an aging, yield stress matrix fluid composed of an aqueous dispersion of Laponite® clay. Using a custom-built magnetorheometry fixture, the MR response is studied for magnetic field strengths up to 1 T and magnetic particle concentrations up to 30 v%. The yield stress of the matrix fluid, which serves to inhibit sedimentation of dispersed carbonyl iron magnetic microparticles, is found to have a negligible effect on the field-induced static yield stress for sufficient applied fields, and good agreement is observed between field-induced static and dynamic yield stresses for all but the lowest

field strengths and particle concentrations. These results, which generally imply a dominance of inter-particle dipolar interactions over the matrix fluid yield stress, are analyzed by considering a dimensionless magnetic yield parameter that quantifies the balance of stresses on particles. By characterizing the applied magnetic field in terms of the average particle magnetization, a rheological master curve is generated for the field-induced static yield stress that indicates a concentration–magnetization superposition. The results presented herein will provide guidance to formulators of MR fluids and designers of MR devices who require a field-induced static yield stress and a dispersion that is essentially indefinitely stable to sedimentation.

4.2 Introduction

Magnetorheological (MR) fluids are field-responsive materials that exhibit fast, dramatic, and reversible changes in properties when subjected to a magnetic field. First introduced by Rabinow [65], MR fluids are composed of microscopic iron-containing particles suspended in a matrix fluid. Upon application of a magnetic field, the particles acquire a dipole moment and align to form domain-spanning chains (see the schematic in Fig. 1.8). This field-induced structuring of the suspension leads to significant changes in rheological properties, including order-of-magnitude growth in the steady-shear viscosity and the emergence of field-dependent yield stress and viscoelastic behavior [64]. The tunability of rheological properties with the applied magnetic field provides the basis for a wide variety of commercial applications of MR fluids, including automobile clutches [65], active dampers [66], seismic vibration control [67], prosthetics [68], precision polishing [69], and drilling fluids [70]. MR fluid research and technology has been reviewed numerous times, with articles focusing on rheology and flow properties [64], models and mechanisms of chain-formation [72, 73], MR fluid formulation [163], and applications [71, 164].

Matrix fluids in MR suspensions have traditionally been aqueous or oil-based Newtonian fluids of moderate viscosity. While this type of formulation maximizes the rheological differences between the activated material and the off-state, particle sedimentation is a major concern in Newtonian matrix fluids due to the (typically) large density difference between iron-containing particles and the surrounding fluid. To address this problem, modifications to both the suspended particles and the matrix fluid have been proposed. For example, according to the Stokes' drag law, sedimentation can be slowed by decreasing the particle size. Experiments have shown, however, that smaller particles generally lead to lower field-induced yield stresses [165]. Additionally, when particle sizes approach nanometer length scales, Brownian effects limit the length and strength of the chain structures that form under an applied field [81]. Composite particles with lower iron content also exhibit slower sedimentation, but the accompanying decrease in magnetization again results in diminished field-induced rheological properties [166]. Reasonable success has been achieved through the use of stabilizing additives that provide a steric hindrance to particle aggregation. Additives such as ferromagnetic nanoparticles [167, 168], fumed silica [169], organoclays [170], and magnetizable nanofibers [171] have been used for this purpose. Arguably the most robust methods for inhibiting sedimentation involve modifying the matrix fluid rheological properties. By employing viscoplastic matrix fluids [79, 83] or thixotropic gel-forming agents such as silica nanoparticles [84, 85], sedimentation can be prevented essentially indefinitely in quiescent dispersions as long as the yield stress of the matrix fluid exceeds the net stress acting on the particles due to gravity and buoyancy [172].

For the set of experimental conditions considered by Rankin *et al.* [79], results indicate that

the matrix fluid yield stress has minimal effect on the field-induced dynamic yield stress. The field-induced *static* yield stress, however, is also an important property in many MR fluid applications and is a more direct measure of the 'strength' of an MR fluid [86]. The dynamic yield stress is typically measured by imposing a set of decreasing steady-state shear rates, $\dot{\gamma}$, and extrapolating the resulting shear stresses to $\dot{\gamma} = 0\ \mathrm{s}^{-1}$. In contrast, the static yield stress is defined as the stress required to induce flow from rest [17]. For materials that exhibit thixotropy or require a finite time to reform microstructure after being sheared, these two yield stress measures are generally not equal [18, 173, 174]. Additionally, in the case of MR fluids, it is reasonable to expect that the effects of a matrix fluid yield stress on field-induced structure and rheology will be more apparent in static yield stress measurements. The externally-applied shear rate in dynamic measurements increases the probability that particles will encounter each other and aggregate despite the matrix fluid yield stress, whereas in static measurements magnetic particles must directly overcome the matrix fluid yield stress in order to form structure and provide an MR response. Because of these complications arising from differences in measuring techniques, and because of the practical utility of yield stress matrix fluids in inhibiting sedimentation, the need remains to develop a more thorough understanding of the effect of matrix fluid yield stresses on field-induced properties in MR fluids.

The yield stress matrix fluid for the work described in this chapter is an aqueous dispersion of the synthetic clay Laponite®. As discussed in greater detail in Chapter 2, Laponite® clay consists of nanometric disks that undergo progressive structural arrest over time when dispersed in water at concentrations as low as about 1 wt% [45, 146, 102, 100]. This continual microstructural development, known as aging, results in complex and time-dependent rheology [106, 148, 147]. Furthermore, the competition between aging and microstructural disruption due to shear (i.e. shear 'rejuvenation') leads to thixotropic behavior [107]. Previous work has addressed the bulk rheology and microrheology of aqueous Laponite® dispersions; for a more thorough description of the current understanding of reviews of the rheology of aqueous Laponite® dispersions, see Chapter 2 and Rich *et al.* [89]. Also, a review of the phase behavior and microstructure of aqueous Laponite® dispersions has been provided by Ruzicka and Zaccarelli [43]. For the purposes of this chapter, the significance of the aging behavior of Laponite® dispersions is that it results in continual growth of the static yield stress of the matrix fluid (see for example Section 3.5.3). Therefore, different matrix fluid yield stresses can be examined simply by allowing the MR composite system to age for different periods of time.

Using a custom-built magnetorheometry fixture [175], the current work explores the field-induced static yield stress of MR suspensions in an aging, yield stress matrix fluid composed of an aqueous dispersion of Laponite®. The MR response is studied as a function of both the magnetic field strength and the age time. Our results indicate that the field-induced static yield stress grows with the applied field in a manner similar to that in a Newtonian matrix fluid, and that, for sufficient magnetic fields, the field-induced yield stress is approximately independent of the age time (or, equivalently, of the matrix fluid yield stress). These observations are explained by considering a dimensionless magnetic yield parameter that characterizes the relative magnitudes of stresses acting on the dispersed magnetic particles. The effect of particle concentration on the magnetorheological response is also examined, and at a given field strength a power law relationship is observed between the field-induced static yield stress and the particle volume fraction. Despite the thixotropic properties of the matrix fluid, good agreement is observed between the field-induced static and dynamic yield stresses for all but the lowest concentrations and magnetic field strengths.

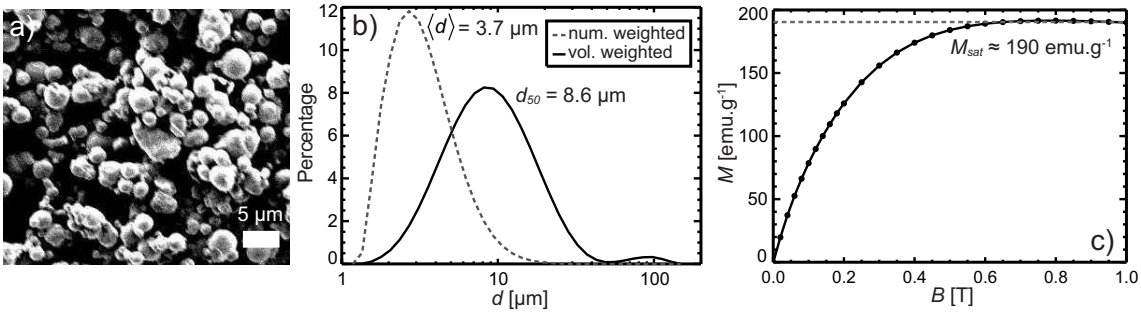

Fig. 4.1: *The magnetic component of the magnetorheological fluid in the present study is CM grade Carbonyl Iron Powder (CIP) (BASF, Ludwigshafen, Germany). (a) Scanning Electron Microscopy (SEM) image of CIP. The powder consists of approximately spherical particles exhibiting some polydispersity and irregularity. (b) Volume-weighted and number-weighted size distributions of CIP particles in the present study. Treating CIP particles as spherical, an average particle diameter of about 3.7 µm is extracted from the number-weighted distribution. Additionally, the volume-weighted distribution indicates that 50% of the powder volume consists of particles with effective diameter* $d \leq d_{50} = 8.6$ *µm, in agreement with data provided by the manufacturer. (c) CIP magnetization curve. Solid lines connect data points and serve to guide the eye. According to the manufacturer's specifications, the particles are* $\geq 99.5\%$ *Fe, leading to large values of the magnetization* M *at moderate applied fields. The particles exhibit linear magnetization for small applied fields (*$B \leq 0.1$ *T) and reach a saturation magnetization of about* $M_{sat} \approx 190$ *emu/g, denoted by the dashed gray line, above about* $B \approx 0.6$ *T.*

By expressing the applied fields in terms of the average particle magnetization, a master curve is generated that indicates a superposition of particle concentration and magnetization.

4.3 Materials and Methods

4.3.1 Carbonyl Iron Magnetic Particles

The magnetic particles providing the MR response in the present study are CM grade carbonyl iron powder (CIP) (BASF, Ludwigshafen, Germany). CM is a 'soft grade' consisting of mechanically soft, approximately spherical particles with an iron content of about 99.5% by weight. Though the CM grade exhibits a wider size distribution than other CIP grades, it is also relatively economical. Fig. 4.1(a) shows a Scanning Electron Microscopy (SEM) image of CIP, providing a sense for the polydispersity and irregularity of the particles. The scale bar corresponds to 5 μm. Particle size distributions of CIP, as measured with a Mastersizer 2000 particle size analyzer (Malvern Instruments, Worcestershire, UK), are shown in Fig. 4.1(b). Both volume-weighted and number-weighted distributions are shown. The number-weighted distribution gives an average particle diameter of $\langle d \rangle \approx 3.7$ μm with a standard deviation of about 2 μm. Additionally, from the volume-

weighted distribution it is found that 50% of the powder volume consists of particles with diameter $d \leq d_{50} \approx 8.6$ μm, in quantitative agreement with data provided by the manufacturer.

Although the increased polydispersity and eccentricity of CIP particles can complicate analysis, the use of CIP in MR fluids provides functional advantages over polymer-magnetite composite superparamagnetic particles because of its stronger magnetic properties, which result from the high iron content. Fig. 4.1(c) shows magnetization data for CIP, obtained using a Vibrating Sample Magnetometer. The particles exhibit linear magnetization up to an applied magnetic field of about $B \approx 0.1$ T. Beyond about $B \approx 0.6$ T, the particles exhibit a constant saturation magnetization of about $M_{sat} \approx 190$ emu/g $= 190$ A·m^2/kg, which is about 10 times greater than that of similar-sized polymer-magnetite superparamagnetic particles (based on data from manufacturer, Invitrogen). Negligible magnetic hysteresis is observed.

In the present study, CIP is suspended in an aging, yield stress matrix fluid, and the MR response of the composite is explored. The matrix fluid consists of a 3.0 w% aqueous dispersion of the synthetic colloidal clay Laponite® (RD grade, Southern Clay Products, Gonzales, TX). The aqueous Laponite® dispersion is prepared in the same way as described in Section 2.3.1. Immediately after mixing and filtering the Laponite® dispersion, CIP is added to the desired concentration and the sample is subjected to vortex mixing for about 30 seconds, resulting in approximately homogeneous dispersion of the CIP particles. The composite suspension is then deposited onto the sample plate of the custom MR cell described below.

4.3.2 Bulk Magnetorheology

The bulk rheology of CIP suspended in aqueous Laponite® dispersions is studied under applied magnetic fields using the custom-built magnetorheology fixture designed by Ocalan [175] that is shown in Fig. 4.2. The magnetic field is generated by passing electrical current (up to 5 Amps) through a coil of copper magnet wire, which is wrapped around a cylindrical core of 1018 carbon steel. The fluid sample is placed between a non-magnetic aluminum sample plate, which is fixed directly above the cylindrical core, and a 20 mm diameter non-magnetic titanium plate geometry that is attached to the spindle rod of the rheometer. To minimize wall-slip, the aluminum sample plate is sandblasted to an RMS roughness of about 3.8 μm, and adhesive-backed 600 grit sandpaper disks (McMaster-Carr, Elmhurst, IL, RMS roughness ≈ 6.0 μm) are attached to the 20 mm top plate. An elastomeric ring on the outer edge of the top plate helps to prevent the sample from escaping from the gap and climbing the spindle rod in response to strong magnetic fields. A thin slot in the bottom of the sample plate provides access for a Gauss probe to measure the magnetic field directly beneath the sample. The entire fixture is housed in a casing of 1018 carbon steel, including a top cover that serves to complete the magnetic circuit and direct the magnetic field through the sample, and then mounted on a stress-controlled rheometer (ARG-2, TA Instruments, New Castle, DE). The casing and cover design prevent the applied magnetic fields from interfering with the magnetic bearing of the rheometer. Temperature control is achieved by flowing silicone oil through channels machined within the casing. Using the fixture, highly uniform magnetic fields up to $B \approx 1$ T can be applied to the sample. For more detailed information about the design of the fixture, its capabilities, and analysis of the applied fields, see [175].

After preparing the sample as described above, the fluid is introduced between the rheometer plates and the gap height is set to 0.5 mm. Because of the thixotropic nature of the Laponite® matrix fluid, steps are taken to ensure consistent initial conditions and promote reproducibility of

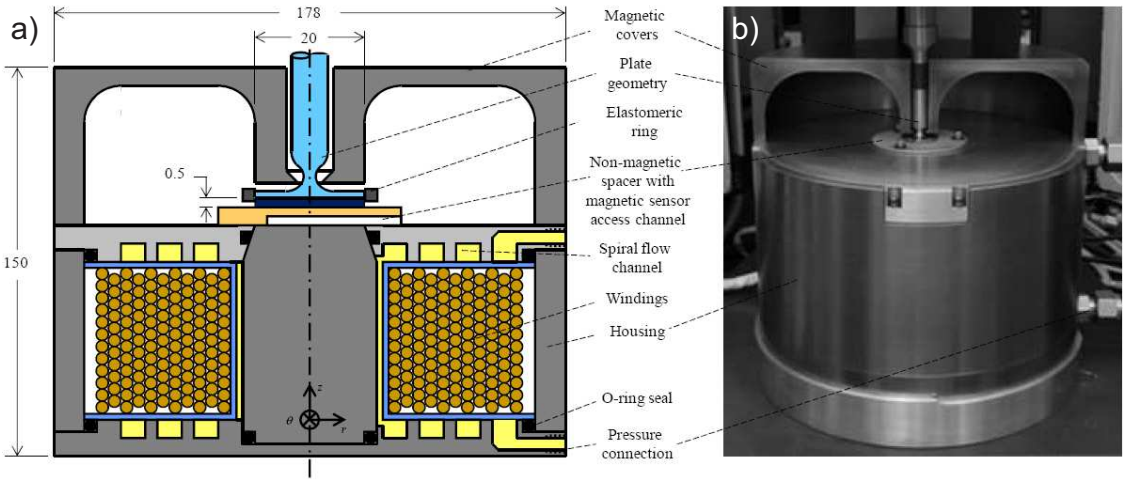

Fig. 4.2: *The custom-built fixture used for magnetorheology experiments shown (a) as a cross-sectional schematic and (b) mounted on a stress-controlled rheometer (images reproduced with permission from [175]). Dimensions are given in millimeters. The magnetorheometry fixture consists of copper magnet wire wrapped around a cylindrical core of 1018 carbon steel. The fluid sample fills the space between a non-magnetic aluminum sample plate and a 20 mm diameter non-magnetic plate of titanium alloy that is attached to the spindle rod of the rheometer. Silicone oil flows through channels surrounding the coil, providing temperature control. Two cover plates of 1018 carbon steel complete the magnetic circuit, helping to direct the field uniformly through the sample. A thin slot in the bottom of the sample plate allows access for a Gauss probe to measure the magnitude of the applied magnetic field. When a current of about 3.5 A passes through the coil, the setup can apply magnetic fields up to $B \approx 1$ T with high spatial uniformity.*

results. Initially, the sample is pre-sheared at a rate of $\dot{\gamma} = 600$ s^{-1} for 10 s, effectively erasing the shear history and resetting the age time, t_w, to zero [62, 37]. Though it has been shown that even a strong shear cannot completely 'rejuvenate' the aging process in aqueous Laponite® dispersions [176], this small amount of irreversibility is found to have a negligible effect on the rheological response of the composite to magnetic fields. Subsequent to the pre-shear at $\dot{\gamma} = 600$ s^{-1} the magnetic component of the suspension is structured by applying a relatively high magnetic field of 0.8 T for 30 s, after which the field is switched off and the material is pre-sheared again at $\dot{\gamma} = 250$ s^{-1} for 20 s. This protocol provides consistent magnetic and shear histories and imposes reproducible initial conditions for magnetorheology experiments [12]. The suspension is allowed to age at a constant temperature $T = 22.5$ °C, and the desired magnetic field is applied starting 30 s before performing rheometric tests to probe the yielding behavior. The primary focus of the present work is the static yield stress, which is measured using continuous ramp tests; starting from a value below the static yield stress, the applied shear stress is increased continuously until the dispersion has yielded, allowing the extraction of the flow curve during yielding. The stress is ramped linearly over a test time of $\Delta t_{test} = 2$ min ($\Delta t_{test} = 1$ min for 10 min age samples), which is small compared to the age of the dispersion t_w. Though attempts are generally made to minimize the rate of stress increase, as long as the initial stress is sufficiently below the static yield stress and $\Delta t_{test} \ll t_w$ the exact rate of stress increase has minimal effect on the results. We note that because the stress is ramped continuously, the measured flow curves do not necessarily correspond precisely to steady-state measurements. However, steady-state measurements would generally be complicated by the aging behavior of the Laponite® matrix fluid [62], so that in this case the continuous ramp tests provide a consistent and meaningful measure of the static yield stress at a particular age time when $\Delta t_{test}/t_w \ll 1$. To measure the dynamic yield stress, steady-state flow tests are performed in which the shear rate is decreased logarithmically in discrete steps from $\dot{\gamma} = 100$ s^{-1} to $\dot{\gamma} = 0.05$ s^{-1}. Starting from higher shear rates has negligible effect on the extracted values of the dynamic yield stress. Because the aging behavior of the matrix fluid can lead to continually evolving properties, a relatively lenient criteria for reaching steady state is used (two consecutive 3-second measurements giving results within 5% of each other), so that the time required for a test remains small compared to the age time (about 1 min). The dynamic yield stress is obtained by extrapolating the measured stress values to $\dot{\gamma} = 0$ s^{-1} [17].

4.4 Results and Discussion

4.4.1 Effects of Magnetic Field and Aging

In Newtonian matrix fluids, chain models for electro- and magneto-rheology predict that the yield stress will increase quadratically with the magnetic field B for low field strengths when the magnetic particles are in the linear magnetization regime [177]. As the magnetic field increases and the particles exhibit nonlinear magnetization, the yield stress is predicted to scale as $B^{3/2}$ and eventually become independent of B as the particle magnetization saturates [178]. These scalings have been confirmed experimentally for spherical particles [167, 179], though some studies have reported a somewhat weaker dependence on B [180, 181]. In matrix fluids composed of viscoplastic grease, Rankin *et al.* [79] reported that the field-induced dynamic yield stress scales with B^x, where x decreases from about 1.5 to 0 as the magnetic field increases and the magnetization of the particles saturates. The value of $x = 1.5$ in grease-based matrix fluids for magnetic fields below the saturation

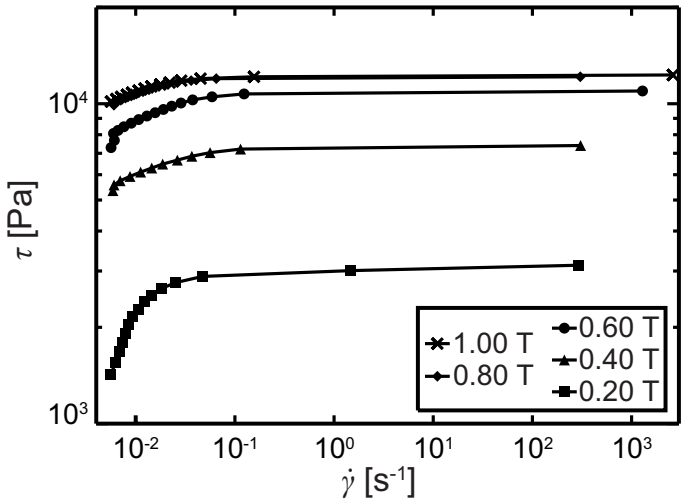

Fig. 4.3: *Typical flow curves from continuous stress ramp tests at various applied magnetic fields. Lines connect data points to guide the eye. The qualitative trends in the data above, which corresponds to a 10 v% CIP suspension in a 3.0 w% aqueous Laponite® dispersion at an age time of 10 min, are representative of all CIP concentrations and age times. At a given magnetic field, the shear rate is negligibly small up to a critical shear stress that corresponds to the field-induced static yield stress, τ_{ys}. Further increasing the applied stress results in the shear rate increasing by several orders of magnitude. Note that since the stress is ramped continuously, the data above do not necessarily correspond directly to steady-state measurements.*

regime (about 0.05 T to 0.35 T) has also been reported by other authors [182, 83].

Flow curves from continuous stress ramp tests under magnetic fields are shown in Fig. 4.3. The sample consists of 10 v% CIP (47 w% CIP) in a 3.0 w% aqueous Laponite® dispersion at an age time of $t_w = 10$ min. The constant age time ensures consistent matrix fluid properties for each measurement. For each value of the magnetic field, very small shear rates are observed until a critical shear stress is exceeded, after which the shear rate abruptly increases by several orders of magnitude. This behavior is a definitive characteristic of field-activated yield stress fluids, and indicates a breaking of the field-induced microstructure at the critical applied stress, which corresponds to the static yield stress, τ_{ys}. Larger values of this critical stress are observed as the magnetic field is increased; at $B = 1.0$ T, the material can support stresses about 4 to 5 times higher than at $B = 0.2$ T without yielding. Beyond about $B = 0.6$ T, the response of the material to applied stress changes minimally, which is a result of the magnetic saturation of the particles at these higher field strengths. While the measured shear rates in these experiments may not necessarily correspond precisely to steady-state measurements, as described above, by maintaining consistent experimental conditions it is possible to extract meaningful and repeatable values of the field-induced static yield stress, τ_{ys}, which is determined as the critical stress above which an abrupt increase in the shear rate is observed [17].

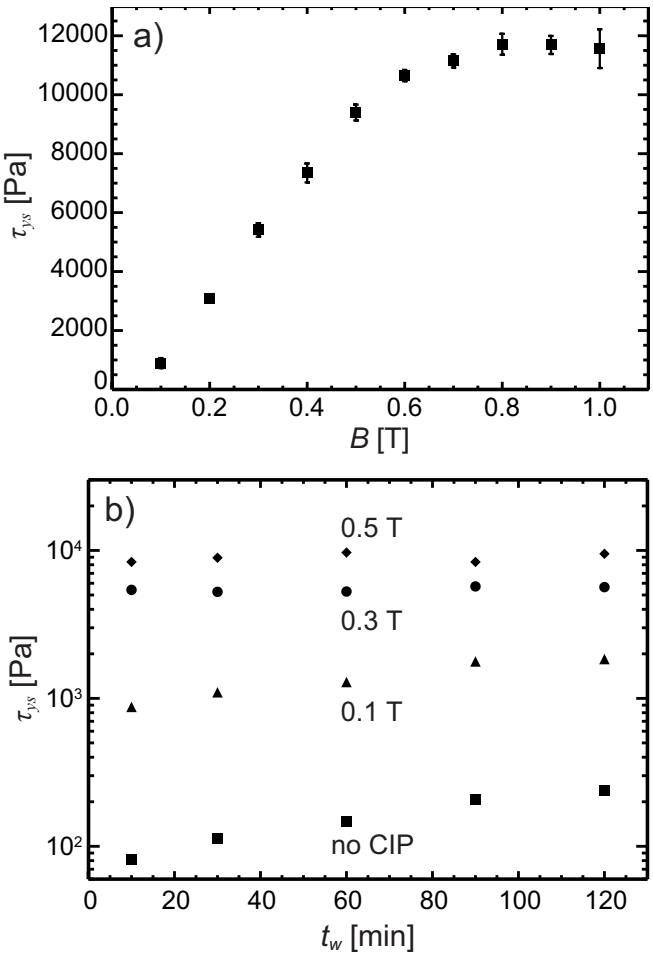

Fig. 4.4: *Field-induced static yield stress, τ_{ys}, of a 10 v% CIP suspension in a 3.0 w% aqueous Laponite® dispersion. (a) Field-induced static yield stress as a function of the applied magnetic field, B, at an age time of $t_w = 10$ min (matrix fluid static yield stress, $\tau_{ys,0} \approx 85$ Pa). Error bars represent the standard deviation of measurements on three different samples. At low field strengths, τ_{ys} increases with the applied magnetic field, B. Saturation of the yield stress is observed for B greater than about 0.6 T, due primarily to the saturation of the particle magnetization [see Fig. 4.1(c)]. τ_{ys} grows by more than an order of magnitude from $B = 0.1$ T to $B = 1.0$ T. (b) Static yield stress as a function of age time, t_w, for 3.0 w% aqueous Laponite® dispersions with no added CIP and with 10 v% CIP at $B = 0.1$, 0.3, and 0.5 T. While the matrix fluid yield stress increases with age time, the yield stress of the composite is essentially independent of age time (i.e, independent of the matrix fluid yield stress) for all but the lowest magnetic field. The addition of CIP and magnetic fields as low as $B = 0.1$ T results in an order of magnitude increase in the static yield stress over that of the matrix fluid alone.*

The field-induced static yield stress for 10 v% CIP is shown as a function of the magnetic field strength, B, in Fig. 4.4(a). The age time for the 3.0 w% aqueous Laponite® matrix fluid is again kept constant at $t_w = 10$ min. Error bars represent the standard deviation between measurements on three different samples, providing an indication of the reproducibility of the measurements. For applied fields of 0.1 T to 0.5 T, τ_{ys} grows approximately linearly with B. As the magnetic field is increased further, a plateau is observed so that for fields above about $B \approx 0.6$ T, τ_{ys} is approximately independent of the magnetic field. This regime is again indicative of the magnetic saturation of CIP particles. Before the onset of magnetic saturation, the magnetic field has a strong effect on the rheology; τ_{ys} increases by about an order of magnitude from $B = 0.1$ T to $B = 1.0$ T. These trends are qualitatively similar to those reported in Newtonian matrix fluids [178]. Though the regime of quadratic dependence on B predicted for Newtonian matrix fluids has not been observed, this is likely because the particles already begin to exhibit nonlinear magnetization effects at $B = 0.1$ T [see Fig. 4.1(c)].

A unique aspect of the aqueous Laponite® matrix fluid used in the present study is its aging behavior. Left quiescent, the rheological properties of the Laponite® dispersion evolve with time as individual clay particles coordinate and an arrested microstructure develops in the material [43]. Aging results in growth of both the yield stress and the matrix viscoelasticity [89, 90] (see also Sections 2.4.1 and 3.5.3), and generally leads to a more solid-like material. Fig. 4.4(b) shows the effect of this aging in the matrix fluid on the magnetorheology of the 10 v% CIP suspension. Squares represent the static yield stress of the 3.0 w% Laponite® matrix fluid with no added CIP, which grows steadily with age time as expected. Without a magnetic field, adding CIP to the matrix fluid raises the static yield stress by at most 60% (at 30 v% CIP), which is small compared to the field-induced gain in the yield stress. For an applied field of $B = 0.1$ T, a small increase in the field-induced static yield stress is observed between $t_w = 10$ min and $t_w = 120$ min. For larger magnetic fields, however, τ_{ys} becomes essentially independent of age time, indicating an insensitivity to matrix fluid properties. Two orders of magnitude separate the values of τ_{ys} for the pure matrix fluid and data for a 10 v% dispersion at $B = 0.5$ T, which again highlights the strong effect of the magnetic field on the rheology.

The independence of τ_{ys} on the matrix fluid rheological properties for moderate to high magnetic field strengths can be understood by considering the relative magnitude of the different stresses acting on the CIP particles. Specifically, the matrix fluid yield stress can be compared to the inter-particle dipolar stress resulting from the applied magnetic field. If mutual magnetic induction is neglected so that all the particles are assumed to have the same constant dipole moment, the interaction energy U_{ij} between two spherical point dipoles with centers separated by a distance r_{ij} and subject to a uniform external magnetic field is given by Equation 1.11, which is repeated here for clarity:

$$U_{ij} = \frac{m^2 \mu_0}{4\pi} \left(\frac{1 - 3\cos\theta_{ij}}{r_{ij}^3} \right) \tag{4.1}$$

Here m is the magnitude of the dipole moment, μ_0 is the magnetic permeability of the medium (assumed to be equal to the permeability of free space), and θ_{ij} is the angle that the line connecting the particle centers makes with the direction of the applied magnetic field, as shown in Fig. 1.9. The attraction force between the particles is maximum when their centers are aligned with the field

($\theta_{ij} = 0$). In this case, the magnitude of the force is

$$F_{ij}|_{\theta_{ij}=0} = \left| -\frac{dU_{ij}\left(\theta = 0\right)}{dr_{ij}} \right| = \frac{3m^2\mu_0}{2\pi r_{ij}^4} \tag{4.2}$$

This expression can be used to find a characteristic force by setting r_{ij} to the particle diameter, d, which is the minimum distance between particle centers. A characteristic magnetic force between particles is therefore

$$F_{char} = \frac{\pi}{24} d^2 \mu_0 \left(\rho M\right)^2 \tag{4.3}$$

Here the dipole moment has been expressed as $m = (\pi/6)\, d^3 \rho M$ where ρ is the particle density and M is the magnetization per unit mass. A characteristic magnetic stress can be found by dividing Equation 4.3 by the surface area of a spherical particle πd^2

$$\tau_{char} = \frac{\mu_0 \left(\rho M\right)^2}{24} \tag{4.4}$$

Comparing the characteristic values obtained from Equation 4.4 to the static yield stress of the matrix fluid, $\tau_{ys,0}$, which must be overcome for the particles to move and form a chain-like structure in response to the imposed field, provides insight into the effect of the matrix fluid on the MR response. This balance of stresses is characterized by the following dimensionless group

$$\mathrm{Y}_{\mathrm{M}}^{*} = \frac{\mu_0 \left(\rho M\right)^2}{24\tau_{ys,0}} \tag{4.5}$$

This parameter is similar to the so-called 'magnetic yield parameter' introduced by previous authors [79]. Generally, if $\mathrm{Y}_{\mathrm{M}}^{*} > 1$ chain-like structures will form under the action of an external magnetic field and a bulk MR response will be observed, whereas if $\mathrm{Y}_{\mathrm{M}}^{*} \ll 1$, the yield stress of the matrix fluid prevents structure formation. For the magnetic CIP particles used in the present experiments, the density of iron is $\rho \approx 7.8$ g/cm^3, and the magnetization data in Fig. 4.1(c) shows that for $B \geq 0.2$ T, $M \sim 100$ emu/g $= 100$ A·m^2/kg. Fig. 4.4(b) shows that the static yield stress of the matrix fluid is on the order of 100 Pa. Using these numerical values in Equation 4.5 gives $\mathrm{Y}_{\mathrm{M}}^{*} \approx 320 \gg 1$. Therefore, the characteristic magnetic stress between particles is much greater than the matrix fluid yield stress. As a result, it is reasonable to expect that moderate changes in the matrix fluid yield stress during aging will have minimal effect on the magnetorheological response. For the case of $B = 0.1$ T, it is helpful to return to Equation 4.2 and recognize that the average distance between particle centers is dependent on the volume fraction of CIP, ϕ_{CIP}. Treating the CIP suspension as a homogeneous dispersion of monodisperse spheres, this volume fraction dependence can be accounted for in an approximate way by replacing r_{ij} with $d\phi_{CIP}^{-1/3}$ rather than simply d. Carrying this change through Equations 4.3–4.5 results in a modification to $\mathrm{Y}_{\mathrm{M}}^{*}$

$$\mathrm{Y}_{\mathrm{M},\phi}^{*} = \frac{\mu_0 \left(\rho M\right)^2}{24\tau_{ys,0}} \phi_{CIP}^{4/3} \tag{4.6}$$

Equation 4.6 matches the expression given for the 'Magnetic Yield Parameter' in Table 1.2. Applying data from Figs. 4.1(c) and 4.4(b) for a 10 v% CIP dispersion at $B = 0.1$ T and a matrix fluid age time of $t_w = 120$ min results in a value of $\mathrm{Y}_{\mathrm{M},\phi}^{*} \approx 4$. The fact that $\mathrm{Y}_{\mathrm{M},\phi}^{*}$ is close to 1

in this case implies that the characteristic magnetic stress on particles exceeds the matrix fluid yield stress by only a small amount. The magnetorheological response of the composite is therefore expected to reflect a combination of the structures formed by magnetic particles as well as the matrix fluid rheology. This is consistent with the observation that the matrix fluid and the 10 v% CIP composite at $B = 0.1$ T exhibit similar rates of growth in the static yield stress during aging. For reference, in the case of a 10 v% CIP dispersion and a matrix fluid age time of $t_w = 120$ min, $\mathrm{Y}^*_{\mathrm{M},\phi} \approx 15$ at $B = 0.3$ T, so that matrix fluid effects are again expected to be minimal for this higher magnetic field strength.

An important complication in microstructured fluids is that rheological properties measured at the bulk scale often do not entirely reflect behavior and properties at the microscopic scale [21, 22]. In the present experiment, suspended CIP particles have an average diameter of about 3.7 μm [see Fig. 4.1(b)], so the yield stress of the matrix fluid measured via bulk rheology may not be representative of the matrix fluid yield stress at the length scale of the magnetic microparticles. This effect could result from pores or other microstructures in the matrix fluid that have similar length scales as the CIP particles. This question was addressed in the previous chapter in Section 3.5.3 [90] in which bulk yield stress values were compared to nonlinear microrheology magnetic tweezer measurements in aqueous Laponite® dispersions. Recall that the probes for microrheology experiments were superparamagnetic spheres of diameter 4.5 μm, which is similar to the average size of CIP particles in this work. For Laponite® concentrations greater than or equal to about 2.0 w%, bulk and micro-scale yield stress measurements were found to agree quantitatively so long as differences in the flow kinematics for the two experiments are correctly taken into account. This kinematic correction consists of an order one factor that approximately captures the shear contribution to the applied stress in the micro-scale experiment involving spherical probe particles. Since the Laponite® concentration in the present work is 3.0 w%, and since the CIP particles are irregular in shape [see Fig. 4.1(a)], we neglect this correction factor and consider the matrix fluid yield stress measured via bulk experiments also representative of that on the length scale of the CIP particles. Further, since the value of the matrix fluid yield stress is used primarily to gain physical insight by evaluating the dimensionless yield parameters defined in Equations 4.5 and 4.6, an order one correction factor will have negligible effect on conclusions.

The observation that the field-induced static yield stress is largely independent of the matrix fluid static yield stress is consistent with the results of Rankin *et al.* [79], who showed similar behavior for the field-induced dynamic yield stress of CIP suspensions in viscoplastic greases. Because of the nature of dynamic yield stress measurements, in which an initial applied shear rate increases the probability that magnetic particles will encounter each other and form chains, and because the measured field-induced dynamic yield stresses exceeded the matrix fluid yield stresses by 2 to 3 orders of magnitude, it is to be expected that the MR dynamic yield stresses measured in the work of Rankin *et al.* [79] would be relatively independent of matrix fluid properties. For field-induced static yield stress measurements, however, the matrix fluid properties can play a more significant role because the magnetic particles must overcome the matrix fluid yield stress in order to form the chain-like structure and provide an MR response. It is therefore unclear *a priori* whether field-induced static yield stress measurements in yield stress matrix fluids would exhibit a similar insensitivity to matrix fluid properties as in the case of dynamic measurements. From the perspective of formulators of MR fluids, independence of the field-induced yield stress on matrix fluid rheology is likely to be an attractive and advantageous property. As long as the matrix fluid yield stress is sufficient to prevent magnetic particle sedimentation, the exact rheological properties

of the matrix fluid have little bearing on the field-responsive rheology. Therefore, the matrix fluid rheology can be optimized to meet various off-state needs or designed for other functionalities with little concern for how the activated material will behave. Care must be taken to account for matrix fluid rheological properties, however, at low field strengths and large matrix fluid yield stresses, as has been discussed. The following section, which examines the role of magnetic particle concentration, shows that effects of the matrix fluid yield stress must also be taken into consideration at low volume fractions of magnetic particles, as implied by Equation 4.6.

4.4.2 Effect of Magnetic Particle Concentration

Increasing the concentration of magnetic particles generally enhances the rheological response of MR fluids to an applied magnetic field [73]. For this reason, volume fractions in commercial applications are often as high as 40 to 50 v% [183], despite the fact that increased concentrations of magnetic particles also result in an elevated off-state viscosity. Established models predict that the field-induced yield stress and viscoelastic storage modulus [178], as well as the viscosity [184], will exhibit a linear dependence on the volume fraction of magnetic particles [64]. While experimental results for the field-induced dynamic yield stress have corroborated this linear relationship up to surprisingly high concentrations in both Newtonian and non-Newtonian matrix fluids, a super-linear increase with volume fraction has been observed above about $\phi_{CIP} = 0.2$ [185, 79, 167, 186]. This behavior is thought to result from the formation of thick columnar structures, as opposed to the single particle-width chains that dominate at low concentrations.

In Fig. 4.5 we show the dependence of the field-induced yield stress on the magnetic field strength, B, for suspensions with different volume fractions of CIP. The matrix fluid is a 3.0 w% aqueous Laponite® dispersion at a constant age time of $t_w = 10$ min ($\tau_{ys,0} \approx 85$ Pa). Filled symbols and solid lines represent the static yield stress, τ_{ys}, while open symbols and dashed lines represent the dynamic yield stress, τ_{yd}, which has typically been reported by previous authors for MR composites in yielding matrix fluids such as greases [79, 83]. For all CIP concentrations, both yield stress measures grow with the magnetic field up to about $B = 0.6$ T, beyond which a plateau is observed. This trend is generally consistent with previous measurements of τ_{yd} in yield stress matrix fluids [79], though the plateau in Fig. 4.5 begins at slightly higher field strengths (most likely due to a different size and grade of CIP). For the largest volume fraction examined in the present work, field-induced static and dynamic yield stresses up to about 50 kPa are observed. Because the matrix fluid yield stress is significantly larger than the gravitational stress acting on particles and continually grows as the dispersion ages, sedimentation is prevented essentially indefinitely for all CIP concentrations examined. Based on these results, it is reasonable to anticipate that gravitationally stable dispersions with higher field-induced yield stresses could be achieved by further increasing the CIP concentration to 40 or 50 v%.

With the exception of results for the lowest CIP concentration at low applied fields, the two measures τ_{ys} and τ_{yd} are in good agreement, indicating that field-induced thixotropy is negligible. This is despite the thixotropic nature of the aqueous Laponite® matrix fluid; at $t_w = 10$ min, $\tau_{ys,0} \approx 85$ Pa while the matrix fluid dynamic yield stress is measured to be $\tau_{yd,0} \approx 20$ Pa. The deviation between τ_{ys} and τ_{yd} at $\phi_{CIP} = 0.01$ and low applied magnetic fields is most likely due to the inability of some dispersed magnetic particles to overcome the matrix fluid yield stress and form gap-spanning chains during the static yield stress measurement. In this dilute dispersion, for which the average distance between particles is relatively large, inter-particle attractive forces at

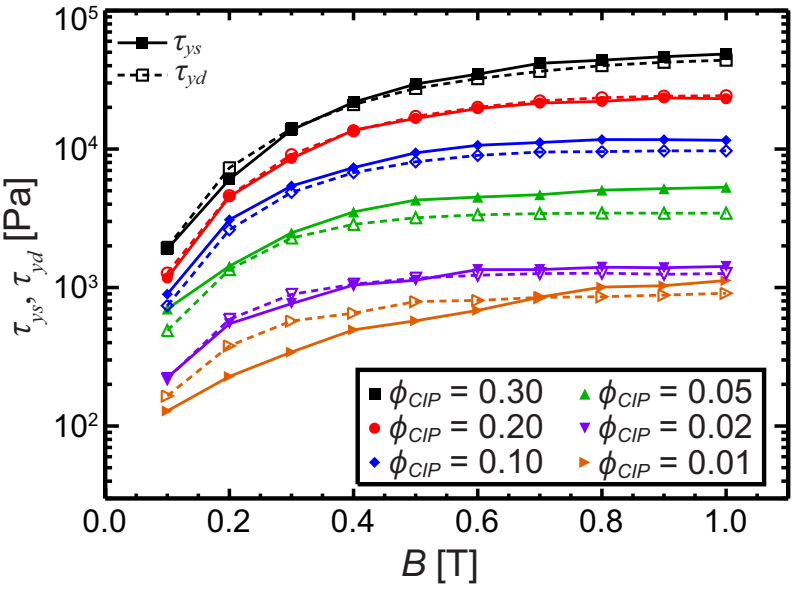

Fig. 4.5: *Field-induced yield stress as a function of magnetic field for various CIP volume fractions, ϕ_{CIP}, in a 3.0 w% aqueous Laponite® dispersion at an age time of $t_w = 10$ min. Both the static yield stress, τ_{ys} (filled symbols and solid lines), and the dynamic yield stress, τ_{yd} (open symbols and dashed lines), are shown. For all CIP concentrations considered in the present study, both measures of the yield stress follow a similar trend with the applied magnetic field, growing with B and exhibiting a plateau above about 0.6 T. Good agreement is observed between the field-induced static and dynamic yield stresses for all but the lowest CIP concentration at low magnetic fields.*

low external fields may be insufficient to overcome the matrix fluid yield stress. Quantitatively, for $\tau_{ys,0} = 85$ Pa, $\phi_{CIP} = 0.01$, and $B = 0.2$ T [$M \approx 125$ emu/g, see Fig. 4.1(c)], inserting parameters into Equation 4.6 gives a volume-fraction corrected yield parameter of $Y^*_{M,\phi} = 1.3$. Values close to unity indicate that the matrix fluid yield stress approximately balances attractive forces between particles resulting from dipolar interactions, hindering chain formation. In the dynamic yield stress measurement, however, bulk shear and rejuvenation of the matrix fluid disrupt and lower the matrix yield stress, enabling viscous flow and increasing the likelihood that particles will aggregate and form chains, as discussed above. Therefore, deviations between τ_{yd} and τ_{ys} are reasonable in this dilute regime at low magnetic field strengths. In particular, the observation that $\tau_{yd} > \tau_{ys}$, in contrast to the case of the pure matrix fluid, is consistent with the mechanism described above.

Fig. 4.5 shows that the field-induced static and dynamic yield stresses increase substantially with CIP concentration. This behavior is specifically highlighted in Fig. 4.6(a), where the yield stress results are plotted as a function of ϕ_{CIP} for constant values of the applied magnetic field. For clarity, only static yield stress measurements for three representative field strengths are shown ($B = 0.1$, 0.2, and 0.5 T), though the dynamic yield stress data is generally quantitatively similar, as previously discussed. At a given field strength, the yield stress increases by more than an order of

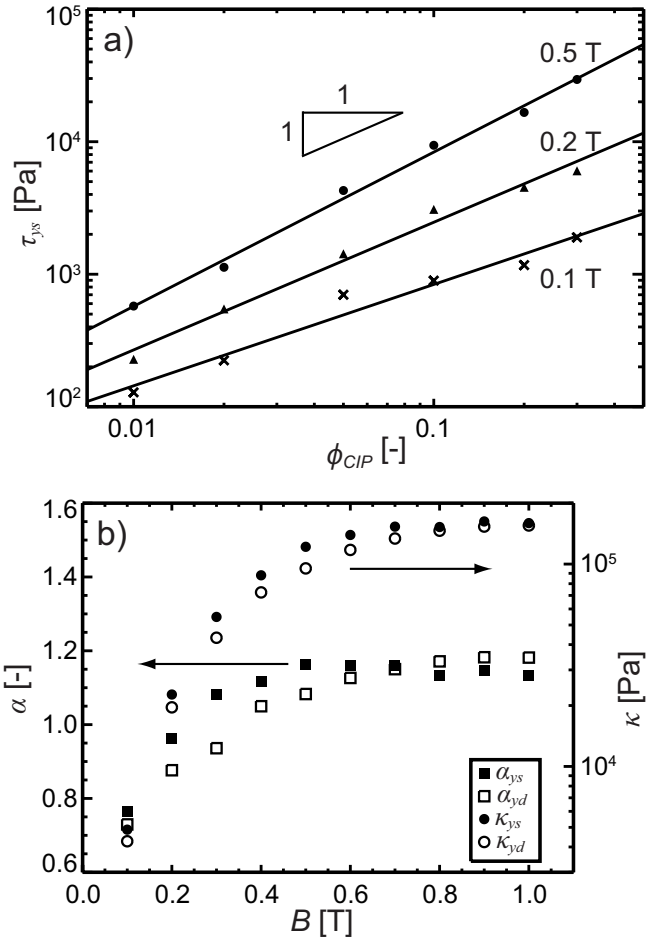

Fig. 4.6: *(a) Variation of the field-induced yield stress with CIP volume fraction in a 3.0 w% aqueous Laponite® dispersion at an age time of* $t_w = 10$ *min. For clarity only static yield stress data at three representative field strengths are shown here, but both* τ_{ys} *and* τ_{yd} *exhibit a similar power-law dependence on* ϕ_{CIP} *for all field strengths. The magnitude of* τ_{ys} *(as well as* τ_{yd}*) increases by almost two orders of magnitude from* $\phi_{CIP} = 0.01$ *to* $\phi_{CIP} = 0.30$*. In (b), the power-law exponents,* α*, and coefficients,* κ*, resulting from least-squares fitting to Equation 4.7 (for which the minimum coefficient of determination is* $R^2 = 0.96$*), are shown for the field-induced static (filled symbols) and dynamic (open symbols) yield stresses. Squares represent the exponent* α*, given on the left axis, while circles represent the front factor* κ*, given on the right axis. The coefficient* κ *grows with the magnetic field in a manner that reflects the field dependence of the yield stress, as shown in Fig. 4.5. Both sets of power-law exponents increase from* $\alpha \approx 0.75$ *at* $B = 0.1$ *T (sub-linear dependence on* ϕ_{CIP}*) to* $\alpha \approx 1.15 \pm 0.06$ *for* B *greater than about 0.5 T (super-linear dependence on* ϕ_{CIP}*).*

magnitude from $\phi_{CIP} = 0.01$ to $\phi_{CIP} = 0.30$. A nearly linear dependence on CIP volume fraction is observed, though a more general power-law relationship is most appropriate

$$\tau_{ys} = \kappa \phi_{CIP}^{\alpha} \tag{4.7}$$

The coefficient κ and the power-law exponent α depend on the field strength. Least-squares fits to Equation 4.7 are shown by black lines. The ability of the power-law form to characterize the data in Fig. 4.6(a) is representative of the goodness of fit for other field strengths, and the power-law fits provide a minimum coefficient of determination of $R^2 = 0.96$. The variation of the fitted parameters in Equation 4.7 with the applied magnetic field is shown in Fig. 4.6(b) for both the static (filled symbols) and dynamic (open symbols) yield stresses. Squares specify the power-law exponent α on the left axis, and circles give the coefficient κ on the right axis. κ values reflect the behavior of the field-induced yield stress, increasing by almost two orders of magnitude from $B = 0.1$ T to $B = 1$ T and exhibiting saturation above about $B = 0.6$ T. Additionally, κ values fitted from static and dynamic yield stress data are in good agreement. While all α values are close to unity, signifying a nearly linear dependence of the yield stress on CIP volume fraction as mentioned above, there is a clear trend in which α increases from $\alpha \approx 0.75$ at $B = 0.1$ T to $\alpha \approx 1.15$ above about $B = 0.5$ T. This indicates that the yield stress increases sub-linearly with ϕ_{CIP} for low field strengths, and super-linearly above about $B = 0.5$ T. The power-law exponents for τ_{ys} and τ_{yd} are in good agreement, deviating by less than 15%. The sub-linear volume fraction dependence of the field-induced yield stress observed here at low field strengths is in contrast to model predictions [178] and previous experimental results [185] for Newtonian matrix fluids, which show a linear dependence on magnetic particle concentration for low field strengths and dilute suspensions. Additionally, previous studies of MR composites in a viscoplastic grease have reported a linear dependence on the volume fraction for $B \approx 0.05$–0.2 T and $\phi_{CIP} = 0.02$–0.25 [79]. These discrepancies are again most likely related to the balance between inter-particle magnetic stresses and the matrix fluid yield stress. For example, for $B = 0.1$ T, $\mathrm{Y}^*_{\mathrm{M},\phi}$ grows from 0.5 to 50 as ϕ_{CIP} is increased from 0.01 to 0.30, implying that measurements will reflect a relative contribution of the matrix fluid yield stress that diminishes as the CIP concentration is increased. The fact that τ_{ys} remains close to the matrix fluid yield stress ($\tau_{ys,0} = 85$ Pa) for $B = 0.1$ T at low CIP concentrations is further evidence for the effect of the matrix fluid. As the CIP concentration increases and $\mathrm{Y}^*_{\mathrm{M},\phi}$ becomes much greater than unity, the magnetic response is expected to dominate the matrix fluid yield stress. Fitting Equation 4.7 to data spanning this range of $\mathrm{Y}^*_{\mathrm{M},\phi}$ values results in a power law exponent that averages the behavior in these two regimes and indicates a sub-linear dependence of the field-induced yield stress on CIP volume fraction. We note that the volume-fraction corrected yield parameter has values $\mathrm{Y}^*_{\mathrm{M},\phi} \geq 5$ under the conditions examined in the work of Rankin *et al.* [79], assuming similar magnetization properties as reported in Fig. 4.1(c).

4.4.3 Generation of Master Curves

Fig. 4.5 shows that the field-induced yield stresses of MR composites with different CIP concentrations exhibit similar trends with magnetic field strength, despite differences in the magnitude of the yield stress. This observation motivates the question of whether the data can be shifted to generate one master curve relating the field-induced yield stress to the magnetic field for different values of ϕ_{CIP}. Such a master curve is shown in Fig. 4.7(a), where the field-induced static yield stress data from Fig. 4.5 is shown as a reduced yield stress, $b\tau_{ys}$, plotted as a function of a

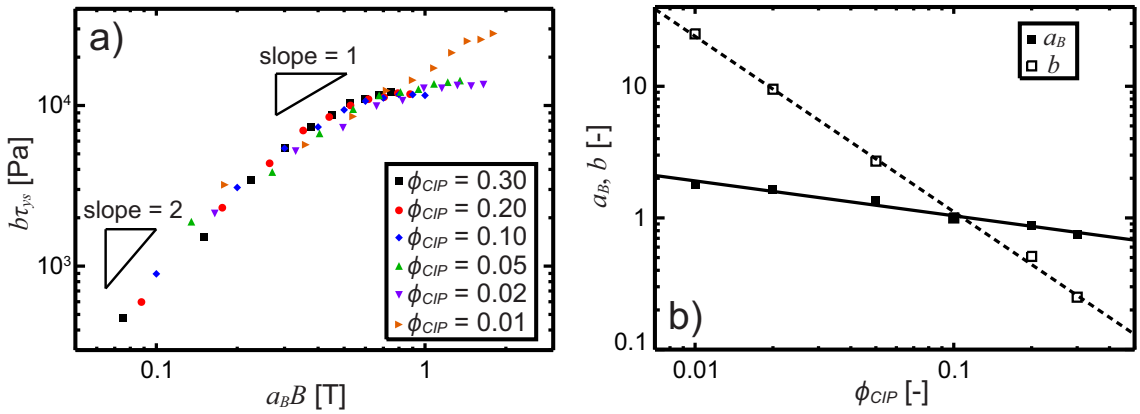

Fig. 4.7: *(a) Master curve showing the reduced field-induced static yield stress as a function of the reduced magnetic field strength in a 3.0 w% Laponite® matrix fluid at $t_w = 10$ min. Static yield stress measurements for different CIP concentrations are shifted to a reference concentration of $\phi_{CIP} = 0.10$ by the horizontal and vertical shifting factors a_B and b, respectively. As the magnitude of the reduced magnetic field increases, the logarithmic slope of the master curve decreases from 2 to 1 and eventually exhibits a plateau. The only exception is the data at 1 v% CIP, which does not appear to follow the same trend as higher CIP concentrations. (b) Horizontal (a_B) and vertical (b) shift factors for the data presented in (a) as a function of the volume fraction of CIP, ϕ_{CIP}. Both sets of shift factors follow a power-law dependence on ϕ_{CIP}; least-squares fitting results in the relationships $a_B \approx 0.56\phi_{CIP}^{-0.26}$ and $b \approx 0.05\phi_{CIP}^{-1.33}$.*

reduced magnetic field strength, $a_B B$. By employing the horizontal and vertical shift factors a_B and b, respectively, yield stress data for different CIP concentrations has been collapsed onto a single master curve that increases with the magnitude of the reduced magnetic field. The data has been shifted to a reference concentration of $\phi_{CIP} = 0.10$. The logarithmic slope of the collapsed data is approximately 2 for $a_B B \leq 0.2$ T, decreases to approximately 1 (linear dependence) in the range 0.3 T $\leq a_B B \leq$ 0.6 T, and subsequently exhibits a plateau. A notable outlier is the data at $\phi_{CIP} = 0.01$ and the highest field strengths, which does not follow quite the same trend as the data for all higher CIP concentrations examined in the present work. Close inspection of this data shows that the field-induced static yield stress for $\phi_{CIP} = 0.01$ does not exhibit a plateau until about $B \geq 0.8$ T (see Fig. 4.5), as opposed to the plateau observed at about $B \geq 0.6$ T for higher CIP concentrations that corresponds to saturation of the particle magnetization. The reason for this delayed plateau is unclear, but our current hypothesis is that this anomaly is likely an additional result of the significant matrix fluid yield stress that hinders chain formation at this dilute CIP concentration for lower magnetic fields (i.e., $Y^*_{M,\phi} \sim 1$), as previously discussed. As the magnetic field is increased, some particles that are restrained by the matrix fluid at lower magnetic fields eventually experience sufficient dipolar forces to overcome the matrix fluid yield stress. This effect may be sensitive to small changes in the average particle magnetization near saturation, but

is not expected to be significant for $\phi_{CIP} \geq 0.02$. This behavior could result in the field-induced yield stress exhibiting a plateau at higher applied magnetic fields at $\phi_{CIP} = 0.01$ than for higher CIP concentrations, leading to the poor collapse observed in Fig. 4.7(a). Numerical simulations of dipolar chain formation in a viscoplastic matrix fluid, which are described in Chapter 5, will aid in further understanding the observations at $\phi_{CIP} = 0.01$.

The variation of the shift factors with the volume fraction of CIP is shown in Fig. 4.7(b). While a_B varies relatively little with ϕ_{CIP}, the vertical shift factor b decreases by about two orders of magnitude from $\phi_{CIP} = 0.01$ to $\phi_{CIP} = 0.30$, reflecting the order of magnitude changes in the field-induced static yield stress over this range of concentrations. Both shift factors follow a power-law dependence on ϕ_{CIP} over the range investigated in the present work. Least-squares fitting to a power-law form leads to the expressions $a_B \approx 0.56\phi_{CIP}^{-0.26}$ and $b \approx 0.05\phi_{CIP}^{-1.33}$ $(0.01 \leq \phi_{CIP} \leq 0.30)$. The master curve in Fig. 4.7, combined with these expressions for the shift factors, can be used to predict the dependence of the field-induced yield stress on the applied magnetic field at CIP concentrations within the range $(0.01 \leq \phi_{CIP} \leq 0.30)$, and to reasonably extrapolate to higher concentrations.

The master curve in Fig. 4.7 relates the field-induced yield stress at various CIP concentrations to a macroscopic, externally-set parameter, the applied magnetic field B. Because different types of magnetic particles exhibit different magnetization responses to applied magnetic fields, the behavior shown in Fig. 4.7 is expected to apply strictly for the particular grade of CIP particles used in the present study. A more general master curve can be developed, however, by considering the dependence of the field-induced yield stress on the average particle magnetization, M, which is an internal variable that characterizes the magnetic response on the particle level [80]. The magnetization can then be related to the applied field via a magnetization curve, as in Fig. 4.1(c). The characteristic inter-particle magnetic stress, $\tau_{char} = \mu_0 (\rho M)^2 / 24$, which was introduced in Equation 4.4, is a physically significant quantity that is set by the average particle magnetization. A correlation or master curve relating the field-induced yield stress and τ_{char} would be applicable for a wide range of magnetic particles because it would be independent of the exact relationship between B and the average particle magnetization, M.

Fig. 4.8(a) shows such an alternative master curve relating the field-induced static yield stress to a reduced characteristic inter-particle magnetic stress, $a_M \tau_{char}$, where $a_M(\phi_{CIP})$ is the magnetization–volume fraction shift factor. The fact that shifting is only required on one axis to generate this alternative master curve suggests that the interactions between particles in field-induced chain structures are effectively scaled and characterized by τ_{char} (i.e., by the particle magnetization). As in Fig. 4.7, yield stress data are again shifted to a reference concentration of $\phi_{CIP} = 0.10$. Data for different values of ϕ_{CIP} are successfully collapsed, once again with the sole exception of the high magnetic field results for $\phi_{CIP} = 0.01$ as was discussed for the shifting in Fig. 4.7(a). These results effectively amount to a concentration–magnetization superposition. The field-induced static yield stress, τ_{ys}, increases with the magnitude of the reduced characteristic inter-particle stress, exhibiting approximately exponential growth at large values of $a_M \tau_{char}$ (appearing linear on semi-log axes). For $a_M \tau_{char} \geq 30$ kPa the argument of the exponential is about $(53 \text{ kPa})^{-1}$, as shown by the black dotted line. The shift factor a_M increases with the CIP volume fraction, and we show in Fig. 4.8(b) that the relationship can be well-approximated as a power law. Least-squares fitting results in the expression $a_M \approx 4.9\phi_{CIP}^{0.77}$ $(0.01 \leq \phi_{CIP} \leq 0.30)$, where the coefficient of determination is $R^2 = 0.98$. In summary, this alternative master curve for the field-induced static yield stress τ_{ys} in the range $a_M \tau_{char} \geq 30$ kPa can be approximately

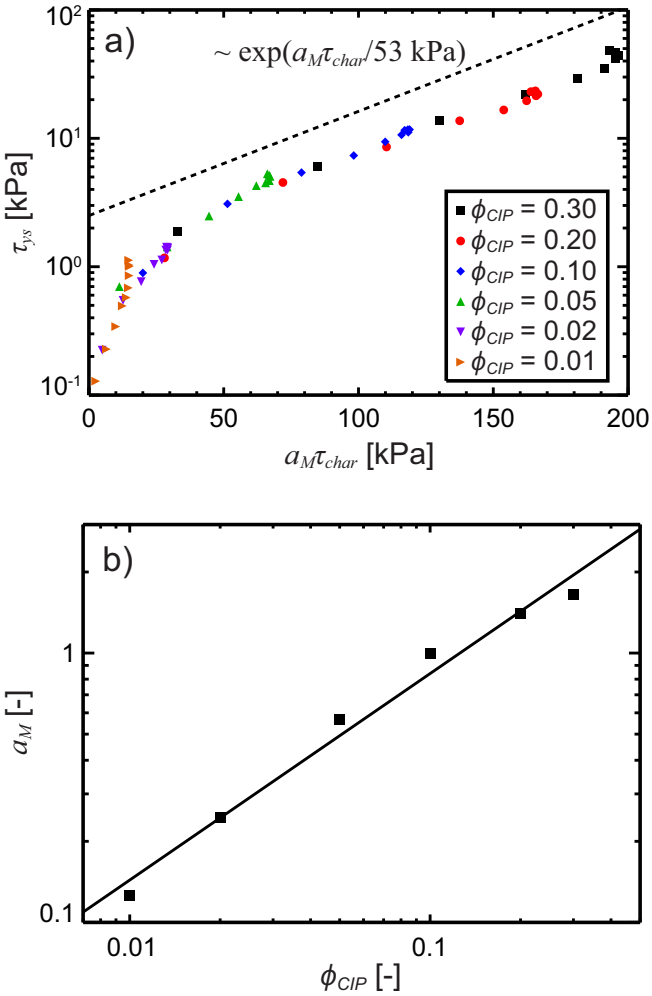

Fig. 4.8: *(a) Alternative master curve for field-induced static yield stress data at various CIP concentrations in a 3.0 w% Laponite® matrix fluid at* $t_w = 10$ *min. Here* τ_{ys} *is plotted as a function of a reduced characteristic magnetic stress between particles,* $a_M\tau_{char}$*, where* a_M *is a shift factor and* τ_{char} *is the characteristic inter-particle magnetic stress given in Equation 4.4 that is a function of the average particle magnetization per unit mass,* M*. Data is again shifted to a reference concentration of* $\phi_{CIP} = 0.10$*. Since* τ_{char} *accounts for the magnetization properties of the suspended particulate phase, the above plot is expected to be more generally applicable for different types of magnetic particles than the master curve in Fig. 4.7(a) and amounts to a concentration–magnetization superposition. In (b), the dependence of the shift factor on CIP concentration is shown. A power law provides a reasonable fit* $\left(R^2 = 0.98\right)$*, and least-squares fitting results in the relationship* $a_M \approx 4.9\phi_{CIP}^{0.77}$*.*

represented as

$$\tau_{ys} \approx A\exp\left(\frac{a_M\tau_{char}}{\tau^*}\right) \qquad (a_M\tau_{char} \geq 30 \text{ kPa}) \tag{4.8}$$

where $A \approx 1.1$ kPa, a_M is the shift factor given by $a_M \approx 4.9\phi_{CIP}^{0.77}$, $\tau^* \approx 53$ kPa, and τ_{char} is the characteristic inter-particle magnetic stress $\mu_0 (\rho M)^2 /24$, which is related to the average particle magnetization per unit mass M. This master curve provides a compact expression for design applications in which the magnitude of the yield stress must be predicted for a given field strength, volume fraction, and particle magnetization. The fact that such a master curve can be generated indicates that the field-induced yield stress in these MR fluids arises from a common physical mechanism that acts over a range of conditions, and that this mechanism depends similarly on particle magnetization and concentration. Additionally, the superposition demonstrated in Fig. 4.8 reinforces the suggestion that higher field-induced yield stresses can be achieved at a given volume fraction by employing particles with a higher saturation magnetization.

4.5 Conclusions and Outlook

The dramatic field-responsive rheological behavior of magnetorheological (MR) fluids, which results from the field-induced chaining of iron micro-particles suspended in a matrix fluid, has been successfully employed in the development of numerous field-activated, 'smart' soft materials. The stability of MR fluids against particle sedimentation remains an important concern, however, especially in applications where re-dispersion after long off-state times is unfeasible. One proposed solution to this problem is the use of yield stress matrix fluids, and previous authors have investigated the field-induced dynamic yield stress of MR composites in viscoplastic matrix fluids. In the current work, analogous studies of the field-induced *static* yield stress have been performed in MR suspensions in an aging, yield stress matrix fluid. MR composites were formulated from carbonyl iron powder (CIP) and a matrix fluid consisting of an aqueous dispersion of Laponite® clay, which is known to exhibit a yield stress that grows as the material ages. As a result, sedimentation of CIP is prevented essentially indefinitely. Using a custom-built magnetorheometry fixture, the field-induced static yield stress of this MR composite was studied as a function of the applied magnetic field strength, B, the CIP volume fraction, ϕ_{CIP}, and the age time, t_w. Results were used to generate a magnetorheological master curve (Fig. 4.8) that indicates a concentration–magnetization superposition and allows prediction of the field-induced yield stress for different types and volume fractions of magnetic particles under a wide range of conditions. A new dimensionless parameter, $\mathrm{Y}^*_{\mathrm{M},\phi}$, was defined (Equation 4.6), which relates the magnitude of the matrix fluid yield stress to the characteristic inter-particle magnetic attractive forces at a given particle concentration. For $\mathrm{Y}^*_{\mathrm{M},\phi} \gg 1$, inter-particle magnetic forces dominate and the field-induced rheology is found to be independent of the matrix fluid yield stress. From a practical perspective of MR formulations, this behavior implies that as long as $\mathrm{Y}^*_{\mathrm{M},\phi} \gg 1$, the rheology of the yield stress matrix fluid can be optimized to meet other design demands without significantly disrupting the behavior of the field-activated material. Conveniently, the condition $\mathrm{Y}^*_{\mathrm{M},\phi} \gg 1$ is frequently satisfied at the high field strengths and particle concentrations used in most commercial MR applications.

While the present study has focused solely on shear magnetorheology, the need for quantitative understanding of MR fluids in squeeze flow has recently been highlighted [64, 187]. Because yield stress matrix fluids could play a similar role in preventing particle sedimentation in squeeze flow MR devices, an important question for future work is whether the presence of a matrix fluid yield stress

has significant effects on the field-induced squeeze flow rheology of MR composites. An additional interesting problem for future studies would be to focus on some of the anomalies documented in this chapter at low volume fractions of magnetic particles. While this dilute regime has limited appeal for traditional MR fluid applications because of the relatively small field-induced yield stresses, the data presented here is suggestive of potentially interesting new regimes and phenomena, which do not appear to have been explored yet. Novel non-traditional applications could be inspired through an improved understanding of systems at $Y^*_{M,\phi} \sim 1$, for which inter-particle attractive forces are approximately in balance with the matrix fluid yield stress. Numerical simulations will aid in elucidating the dynamics and equilibrium microstructures of dipolar particles under these conditions (see Chapter 5).

The results presented here will aid designers of MR devices and guide formulators of MR suspensions in the choice of appropriate viscoplastic matrix fluids. The master curves, correlations, and scaling relationships described in the current study characterize the field-induced static and dynamic yield stress of an MR fluid that is essentially indefinitely stable to sedimentation. This behavior is especially attractive for applications such as active earthquake dampers or field-responsive drilling fluids, for which re-suspension of a dense, concentrated particle phase after long off-state times is typically unfeasible.

This chapter demonstrates that aqueous Laponite® dispersions are suitable yield stress matrix fluids for magnetorheological suspensions, preventing magnetic particle sedimentation without affecting the field-responsive magnetorheology under the conditions used in most commercial applications. In order to better understand the magnetorheological behavior presented in this chapter, especially in the regime where inter-particle attractive forces are approximately in balance with the matrix fluid yield stress, we transition in Chapter 5 to discussions of particle-level simulations of magnetic self-assembly in yield stress matrix fluids. We focus on elucidating the effect of the matrix fluid yield stress on the field-induced microstructure of these suspensions, and attempt to relate these microstructures to the magnetorheological observations in this chapter.

CHAPTER 5

Magnetic Particle Assembly in Yield Stress Matrix Fluids

In this chapter, we use particle-level simulations to investigate the field-induced structure in a suspension of dipolar particles in the presence of a matrix fluid yield stress. This work complements the bulk magnetorheology results in the previous chapter, providing insights into the nature of dipolar chains and aggregates in the MR suspension. The equilibrium microstructures determined from particle-level simulations are consistent with the magnetorheological observations in Chapter 4, and our results additionally highlight a new approach to tuning field-directed assembly through modification of the matrix fluid rheological properties. An article describing this work has been submitted to the journal *Langmuir* [92].

5.1 Overview

The process of assembling particles into organized functional structures is influenced by the rheological properties of the matrix fluid in which the assembly takes place. Therefore, tuning these properties represents a viable and as yet unexplored approach for controlling particle assembly. In this letter, we examine the effect of the matrix fluid yield stress on the directed assembly of polarizable particles into linear chains under a uniform external magnetic field. Using particle-level simulations with a simple yield stress model, we find that chain-growth follows the same trajectory

as in Newtonian matrix fluids up to a critical time that depends on the balance between the yield stress and the strength of magnetic interactions between particles; subsequently, the system undergoes structural arrest. We confirm that the dimensionless groups described in the previous chapter are appropriate for characterizing the arresting behavior and present relationships between these groups and the resulting structural properties. Since field-induced structures can be indefinitely stabilized by the matrix fluid yield stress and 'frozen' into place as desired, this approach may facilitate the assembly of more complex and sophisticated structures.

5.2 Introduction

The assembly of colloids and nanoparticles into complex and highly-ordered structures continues to be an important and effective method for creating functional materials with unique and technologically attractive properties [188, 189]. Through manipulation of the thermodynamic and kinetic interactions between particle building blocks, authors have demonstrated the assembly of materials such as photonic crystals [190] and electronic circuits [191, 192], as well as biomaterials such as peptide-based scaffolds for regenerative medicine [193, 194]. Approaches to controlling the assembly process generally fall into three categories: adjusting particle or template properties like shape, size, patterning, and chemical functionality [195, 196]; tuning particle interactions via thermodynamic variables such as temperature or pH [197, 198]; and directing particle behavior with external flows or fields, such as electric or magnetic fields [189, 199]. In particular, by applying a uniform magnetic field to polarizable colloids suspended in a matrix fluid, directed assembly of the particles into aggregated chain-like structures in the direction of the external field can be achieved [81]. The anisotropic mechanical properties of these structures have been exploited in magnetorheological (MR) fluids [71, 64], which undergo dramatic changes in bulk rheological properties upon formation of particle chains (see the schematic in Fig. 1.8), as well as for lab-on-a-chip separations [200]. The matrix fluid in most particle assembly studies, as well as in most MR fluids and devices, is typically Newtonian; however, it has long been known in the rheology community that the behavior of suspended particles is significantly influenced by the matrix fluid rheology [172]. For example, Feng and Joseph demonstrated that spherical particles dispersed in viscoelastic Boger fluids subjected to bulk torsional flow undergo radial migration to form distinct ring patterns; by contrast, no such microstructure was observed in the Newtonian case [201]. Additionally, the use of yield stress matrix fluids to prevent sedimentation in MR suspensions has motivated questions about the effects of the yield stress on the formation of field-induced structures (see Chapter 4) [79, 91].

With these considerations in mind, we present in this chapter a new approach to controlling particle assembly via the non-Newtonian properties of the matrix fluid. Because of the immediate relevance to MR fluid technology, we specifically demonstrate this approach by examining the effect of the matrix fluid yield stress on the directed assembly of polarizable particles under a uniform external magnetic field. Using 2-D particle-level simulations, we find that chain growth initially follows the same trajectory as in Newtonian matrix fluids, but is arrested at a critical time that scales with a dimensionless group that characterizes the balance between the yield stress and interparticle magnetic stresses. Adjusting this balance allows the properties of the arrested structure, including the average cluster size, to be tuned. Assuming the matrix fluid yield stress dominates over other forces on particles (i.e., thermal, gravitational, electrostatic, etc.), arrested structures are indefinitely stable even after the magnetic field is removed, being essentially 'frozen' in the matrix until additional manipulation is desired. This behavior is generic to particle dynamics in yield

stress matrix fluids and could be exploited in other types of assembly processes, including assembly via electric fields, fluid flow, or chemical interactions. Finally, this letter will have important implications for the formulation and understanding of MR suspensions stabilized by yield stress matrix fluids. We identify regimes in which the arrest of dipolar chain-formation due to the matrix fluid yield stress is expected to significantly impact the field-induced rheological properties.

5.3 Simulation Details

The simulation method used in this work is adopted from a previously described algorithm [202, 76], which was developed to study field-induced chaining of dipolar particle suspensions in Newtonian matrix fluids. We review the essential features of this method and discuss the modifications necessary to incorporate a matrix fluid yield stress. Recall the pair-wise magnetic interaction energy U_{ij}^{mag} between two dipoles separated by a distance r_{ij}, which is given in Equations 1.11 and 4.1 and repeated here for clarity:

$$U_{ij}^{mag} = \frac{m^2 \mu_0}{4\pi} \left(\frac{1 - 3\cos\theta_{ij}}{r_{ij}^3} \right) \tag{5.1}$$

Here m is the magnitude of the dipole moment, μ_0 is the magnetic permeability of the medium (assumed to be equal to the permeability of free space), and θ_{ij} is the angle that the line connecting the particle centers makes with the direction of the applied magnetic field, as shown in Fig. 1.9. Though Equation 5.1 neglects mutual magnetic induction and treats particles as point dipoles with identical dipole moments aligned with the external magnetic field, this expression has been successful in quantitatively capturing the particle-level behavior in MR suspensions subject to a uniform external magnetic field [202, 203, 204]. In the work of Haghgooie [76], the Heyes–Melrose displacement algorithm is used to correct for hard-sphere overlaps between dipolar particles at each time step of the simulation [205]. This approach complicates the incorporation of a matrix fluid yield stress, however, because it accounts for excluded volume interactions through a constraint rather than an explicit potential. Additionally, we find that when attempts are made to incorporate a matrix fluid yield stress, the Heyes–Melrose algorithm leads to unphysical behavior such as 'kinked' chains that drift in a direction perpendicular to the applied magnetic field. Therefore, we instead include a short-ranged repulsive potential between particles [206]:

$$U_{ij}^{rep} = \frac{3\mu_0 r_c m^2}{4\pi d^4} \exp\left(-\frac{r_{ij} - d}{r_c} \right) \tag{5.2}$$

where d is the particle diameter, and r_c is a constant that controls the range of the interaction. For this work, we set $r_c = 0.05d$. Lower values of r_c better approximate a hard-sphere potential, but require prohibitively short time steps. In order to simplify the simulation so that effects of the matrix fluid yield stress can be more easily distinguished, we neglect thermal forces and hydrodynamic interactions. In this case, the total force $\mathbf{F}_i$ on particle i at time t is calculated as:

$$\mathbf{F}_i(t) = \sum_{i \neq j}^{N} -\nabla \left[U_{ij}^{mag}\left(r_{ij}(t), \theta_{ij}(t)\right) + U_{ij}^{rep}\left(r_{ij}(t), \theta_{ij}(t)\right) \right] \tag{5.3}$$

The Langevin equation describing the particle velocity is then

$$d\mathbf{r}_i(t) \simeq \frac{1}{\zeta}\mathbf{F}_i(t)\,dt \tag{5.4}$$

where ζ is the drag coefficient of a particle. In order to generalize the simulation results, Equation 5.4 is made dimensionless using the characteristic length scale d and the characteristic force $F_{char} = \pi d^2 \mu_0 (\rho M)^2 /24$, where ρ is the particle mass density, and M is the particle magnetization per unit mass. M is related to the dipole moment via the expression $M = m/V\rho$, where V is the particle volume. This expression for the characteristic force is the same as that given in Equation 4.3, which is the force between two spherical dipolar particles aligned with the external magnetic field and in contact. Applying these scalings, the dimensionless Langevin equation becomes

$$d\hat{\mathbf{r}}_i\left(\hat{t}\right) \simeq \hat{\mathbf{F}}_i\left(\hat{t}\right)d\hat{t} \tag{5.5}$$

where $\hat{}$ represents dimensionless variables. Setting $t_{char} = 24\zeta/\pi d\mu_0 (\rho M)^2$ as the characteristic time scale removes all free parameters from the dimensionless Langevin equation. This time scale represents the time necessary for a particle to move a distance of one particle diameter in response to the characteristic driving force F_{char}.

A Bingham viscoplastic model for a yield stress matrix fluid is incorporated by applying a constraint to Equation 5.5. We make the simple approximation that a particle moves during a time step only if the sum of the forces on the particle (including both magnetic and short-range steric forces) is sufficient to overcome the matrix fluid yield stress, $\tau_{ys,0}$. Otherwise, the particle remains motionless for that time step. Mathematically, if $\|\mathbf{F}_i\| \geq \pi d^2 \tau_{ys,0}/2C$, then the particle executes a step according to Equation 5.5; otherwise, $d\mathbf{r}_i$ is set to 0. C is a constant that relates the matrix fluid yield stress to the critical force necessary to cause an embedded particle to yield. For spherical particles in Bingham fluids, Beris *et al.* showed using finite-element modeling that $C \approx 0.143$ [162]. In dimensionless terms, the criteria for yielding is

$$\left\|\hat{\mathbf{F}}_i\right\| \geq \frac{12\tau_{ys,0}}{\mu_0 C (\rho M)^2} = \frac{1}{\mathrm{Y}_\mathrm{M}^*} \tag{5.6}$$

where

$$\mathrm{Y}_\mathrm{M}^* \equiv \frac{\mu_0 C (\rho M)^2}{12\tau_{ys,0}} \tag{5.7}$$

The dimensionless yield parameter Y_M^* can be understood as the characteristic inter-particle magnetic stress divided by the matrix fluid yield stress $\tau_{ys,0}$. That is, for $\mathrm{Y}_\mathrm{M}^* \gg 1$, magnetic forces dominate over the yield stress, while $\mathrm{Y}_\mathrm{M}^* \ll 1$ corresponds to an immobilized system in which magnetic forces are too weak to overcome the yield stress. Note that this definition of Y_M^* is the same as that in Equation 4.5, except that the expression has been generalized by incorporating the factor C in the numerator. For Equation 4.5 and the work in Chapter 4, C is effectively taken to be 0.5.

Simulations are conducted in 2-D with a uniform external magnetic field in the vertical direction. The simulation box is square with a side length equal to 100 particle diameters and periodic boundary conditions on all sides. To begin simulations, particles are initially placed in the box in a random configuration with no particle overlaps and Equation 5.5 is integrated forward in time

using a simple Euler scheme for 1000 time steps at a time-step size of $\Delta\hat{t} = 3.3\text{e-}7$. The purpose of this short preparatory simulation using a very small time step is to resolve the trajectories of any particles positioned very close to each other in the random initial placements. Subsequently, the time-step size is increased to $\Delta\hat{t} = 3.3\text{e-}4$ for the remainder of the simulation. The constraint in Equation 5.6 is applied at each time step. A dimensionless spatial cutoff (scaled with the particle diameter) for the inter-particle forces of 15 was used along with a linked-list binning algorithm [207] with bin sizes that slightly exceed the cutoff value [202, 76]. Therefore, interactions between particles separated by a distance larger than the cutoff are not considered, resulting in faster processing times. It was confirmed that under these conditions, the simulations are converged in time step, system size, and interaction cutoff length. Interested readers are referred to earlier communications for additional details about the simulation algorithm [202, 76].

5.4 Particle Assembly Simulation Results and Discussion

It is well-known that applying a uniform magnetic field to a dispersion of polarizable spherical particles in a Newtonian matrix fluid results in the formation of long-chain structures in the direction of the external field. Since a matrix fluid with a strong enough yield stress will completely immobilize particles, we examine magnetic directed assembly in a regime where both magnetic interactions and the matrix fluid yield stress play an important role in structure formation. Because the characteristic force in our simulations is defined as the maximum force between two dipolar particles, the regime of interest corresponds to values $\mathrm{Y}_{\mathrm{M}}^{*} > 1$.

Images of magnetically assembled structures after long times $\left(\hat{t} = 2667\right)$ are shown in Fig. 5.1 for dispersions with a particle area fraction of $\phi_A = 0.15$ and magnetic yield parameters of (a) $\mathrm{Y}_{\mathrm{M}}^{*} = 6.7$, (b) $\mathrm{Y}_{\mathrm{M}}^{*} = 67$, and (c) the Newtonian case ($\mathrm{Y}_{\mathrm{M}}^{*} \to \infty$). At $\mathrm{Y}_{\mathrm{M}}^{*} = 6.7$, only a marginal development of the structure from the initial condition is observed, as the equilibrium configuration consists of a randomly distributed mixture of individual particles and small chains; the magnetic interactions are not strong enough to generate large-scale structures. At $\mathrm{Y}_{\mathrm{M}}^{*} = 67$, the average chain length is significantly longer at equilibrium, and the vast majority of particles are incorporated in vertically-aligned chains. As $\mathrm{Y}_{\mathrm{M}}^{*}$ increases, the limiting Newtonian case is approached, for which domain-spanning chains are formed and some lateral aggregation of chains is evident. We note that while Figs. 5.1(a) and 5.1(b) represent arrested configurations, chaining and lateral aggregation continue very slowly in the Newtonian system even up to $\hat{t} = 2667$.

As a first step towards understanding this behavior, we consider a simpler system of two dipolar particles in a yield stress matrix fluid. With one particle fixed at the origin, yielding occurs if the distance to the second particle is sufficiently small that the inter-particle force overcomes the matrix fluid yield stress; otherwise, both particles remain immobile. For this system, the critical positions for yielding can be found by solving for the contour on which the magnitude of the dimensionless force on the second particle is equal to $1/\mathrm{Y}_{\mathrm{M}}^{*}$, as in the yield criteria in Equation 5.6. Neglecting the repulsive steric force, which is much smaller than the magnetic force for these inter-particle distances, the magnitude of the force on the particle is calculated from Equation 5.3:

$$\|\mathbf{F}_i\| \approx \left\| \nabla U_{ij}^{mag}\left(r_{ij}, \theta_{ij}\right) \right\| = \sqrt{\left(\frac{\partial U_{ij}^{mag}}{\partial r_{ij}}\right)^2 + \frac{1}{r_{ij}^2}\left(\frac{\partial U_{ij}^{mag}}{\partial \theta_{ij}}\right)^2} \tag{5.8}$$

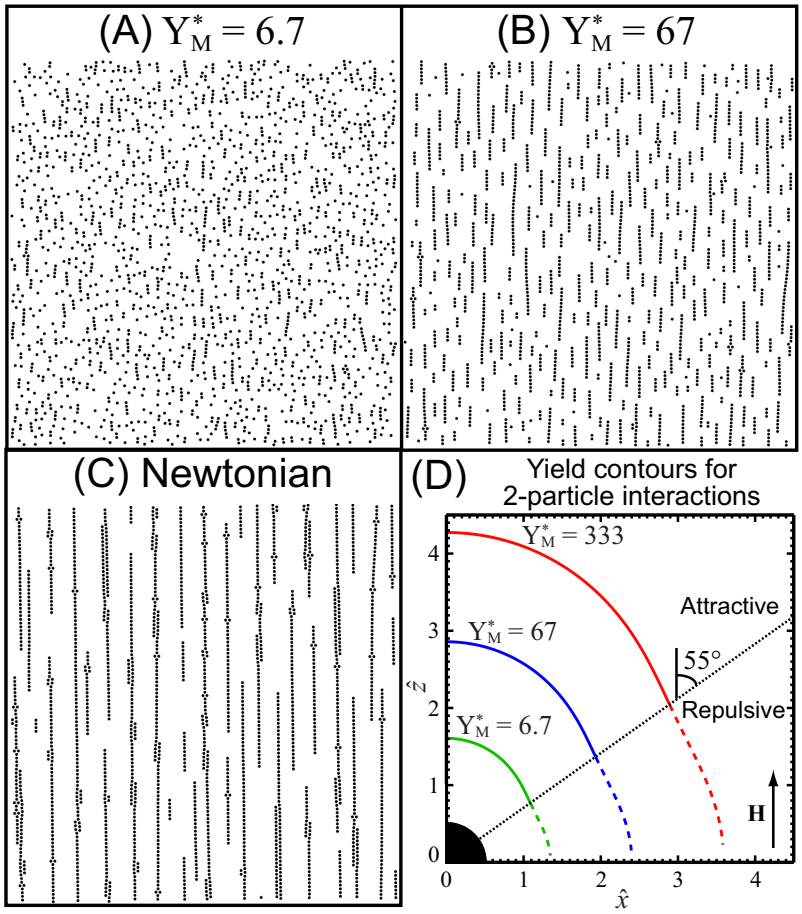

Fig. 5.1: *Magnetically assembled structures at* $\phi_A = 0.15$ *at long times* $(\hat{t} = 2667)$ *for dimensionless magnetic yield parameters of (a)* $Y_M^* = 6.7$ *and (b)* $Y_M^* = 67$ *and (c) the Newtonian case* $(Y_M^* \to \infty)$. *The applied magnetic field is in the vertical direction. While a mixture of individual particles and short chains is observed at* $Y_M^* = 6.7$, *increasing* Y_M^* *results in an equilibrium state with greater numbers of particles incorporated into longer chains. In (d), contours show the critical configurations at which yielding occurs in a 2-particle system at various values of* Y_M^*. *With one particle fixed at the origin, a second particle yields if its position is on or inside the contour (given by Equation 5.11); otherwise, the system is arrested. Depending on the angle between the line connecting the particle centers and the direction of the applied magnetic field* **H**, *magnetic interactions are attractive or repulsive. The yield contours expand with* Y_M^* *and are symmetric across the vertical and horizontal axes.*

Using the expression for U_{ij}^{mag} in Equation 5.1 and the fact that $m = V\rho M$, the magnitude of the force on the particle is given by

$$\|\mathbf{F}_i\| \approx \frac{\mu_0 \pi d^6 (\rho M)^2}{48 r_{ij}^4} \sqrt{\left(1 - 3\cos^2\theta_{ij}\right)^2 + \sin^2\left(2\theta_{ij}\right)} \tag{5.9}$$

Dividing each side of Equation 5.9 by F_{char}, we find that the magnitude of the dimensionless force is therefore

$$\left\|\hat{\mathbf{F}}_i\right\| \approx \frac{1}{2\hat{r}_{ij}^4} \sqrt{\left(1 - 3\cos^2\theta_{ij}\right)^2 + \sin^2\left(2\theta_{ij}\right)} \tag{5.10}$$

Setting $\left\|\hat{\mathbf{F}}_i\right\| = 1/\mathrm{Y}_{\mathrm{M}}^*$ gives the expression for the yield contour.

$$\hat{r}_{ij}\left(\theta_{ij}\right) \approx \left[\frac{\mathrm{Y}_{\mathrm{M}}^*}{2} \sqrt{\left(1 - 3\cos^2\theta_{ij}\right)^2 + \sin^2\left(2\theta_{ij}\right)}\right]^{1/4} \tag{5.11}$$

Contours corresponding to Equation 5.11 are plotted in Fig. 5.1(d) for an external magnetic field $\mathbf{H}$ in the vertical direction and $\mathrm{Y}_{\mathrm{M}}^*$ values of 6.7, 67, and 333. As $\mathrm{Y}_{\mathrm{M}}^*$ increases, the contours expand and particles positioned farther from the origin are able to yield in response to the applied magnetic field. Because of the angular dependence of dipolar interactions, the inter-particle force is either attractive ($0^\circ \leq \theta_{ij} < 55^\circ$, solid lines), for which yielded particles undergo aggregation, or repulsive ($55^\circ < \theta_{ij} \leq 90^\circ$, dotted lines), for which particles tend towards an unaggregated arrested state. Though only one quadrant is shown in Fig. 5.1(d), the contours are symmetric across the vertical and horizontal axes. While multi-particle interactions captured in the full simulations (including the behavior of particle chains) are more complex than this two-particle system, the contours in Fig. 5.1(d) are nonetheless helpful in understanding the basic physical phenomena underlying dipolar particle suspensions in the presence of a yield stress. In particular, Fig. 5.1(d) implies that a particle (or a chain of particles) is arrested when the envelope defined by the yield contour becomes devoid of particles.

The images in Fig. 5.1 imply that the magnetically assembled structures consist primarily of vertically-connected, chain-like aggregates, and that a relatively small amount of lateral aggregation can occur at higher values of $\mathrm{Y}_{\mathrm{M}}^*$. To explore the directionality of structures quantitatively, we calculate the vertical connectivity, C_v, and the horizontal connectivity, C_h, defined as the number of vertical and horizontal connections, respectively, scaled by $N - 1$, where N is the number of particles in the simulation [76]. One connection is counted for each pair of particles with centers separated by a dimensionless distance of at most 1.05 (i.e., the radii at contact + 5%). Connections are considered to be vertical if $\theta_{ij} \leq 30^\circ$ or $\theta_{ij} \geq 150^\circ$, and horizontal if $30^\circ < \theta_{ij} < 150^\circ$. C_v and C_h are plotted in Fig. 5.2 as functions of the dimensionless time for various values of $\mathrm{Y}_{\mathrm{M}}^*$, with the top curves representing C_v and the bottom curves representing C_h. All simulations begin with the same initial condition of randomly placed particles. C_v generally grows with time and, after an initial rearrangement of the starting configuration, is at least an order of magnitude greater than C_h for all $\mathrm{Y}_{\mathrm{M}}^*$. These observations are consistent with the formation of vertically-aligned chains as shown in Fig. 5.1. C_h decreases during the initial rearrangement, exhibiting some scatter due to very small numbers of horizontal connections, then increases as some lateral aggregation of chains occurs on longer time scales. Perhaps the most striking feature of the results is that at a critical

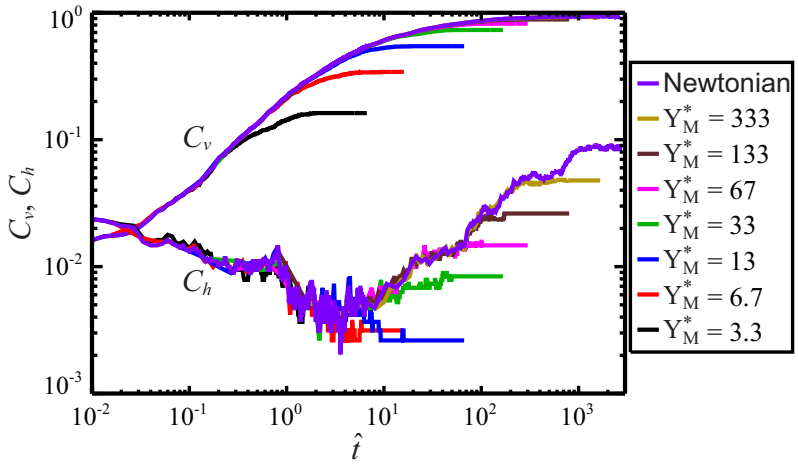

Fig. 5.2: *Time evolution of the vertical and horizontal connectivities (C_v and C_h, respectively) of magnetically assembled anisotropic chain structures for a system at $\phi_A = 0.15$ and various values of Y_M^*. All simulations begin with the same initial condition of randomly placed particles. With the exception of an initial decline in C_h during rearrangement of the starting configuration, the connectivities generally grow with time, following the Newtonian result until deviations begin at a critical time and connectivity that increase with Y_M^*. The fact that $C_v \gg C_h$ after the initial rearrangement indicates that chains are primarily vertically connected, as is seen in Fig. 5.1.*

time (which increases with Y_M^*) both connectivity measures diverge from the common trajectory that coincides with the behavior of the Newtonian system. Subsequent to this separation, both C_v and C_h plateau and cease to evolve in the systems with a yield stress matrix fluid. Visualizing the particle behavior in the simulations confirms that all particles are immobilized when the plateau in the connectivity data is attained. This behavior implies that while the matrix fluid yield stress does not affect the mechanism of structural development, it results in an arrest of chain growth. Though it is reasonable to expect that a matrix fluid yield stress would hinder structure formation, it is remarkable that the dynamics for all Y_M^* values appear to follow the Newtonian trajectory until a critical time corresponding to the onset of structural arrest.

The observation that suspensions of dipolar particles in yield stress matrix fluids undergo structural arrest from a common trajectory is also supported by data for the time-evolution of the average cluster size, $\langle c \rangle$, shown in Fig. 5.3 for the same simulation conditions shown in Fig. 5.2. The average cluster size is calculated as $\langle c \rangle = N/N_c$, where N_c is the total number of clusters and a cluster is identified as a collection of continuously connected particles according to the definition of a connection given above [76]. The average cluster size grows with time and, in accordance with the connectivity results, data at finite values of Y_M^* break away from a common trajectory at a critical time that increases with Y_M^*. In the yield stress systems, $\langle c \rangle$ eventually plateaus at equilibrium values that grow with Y_M^* but are uniformly smaller than the long-time Newtonian result. Taking the critical arrest time, $\hat{t}_{arrest}$, as the time at which $\langle c \rangle$ becomes less than 90% of the Newtonian

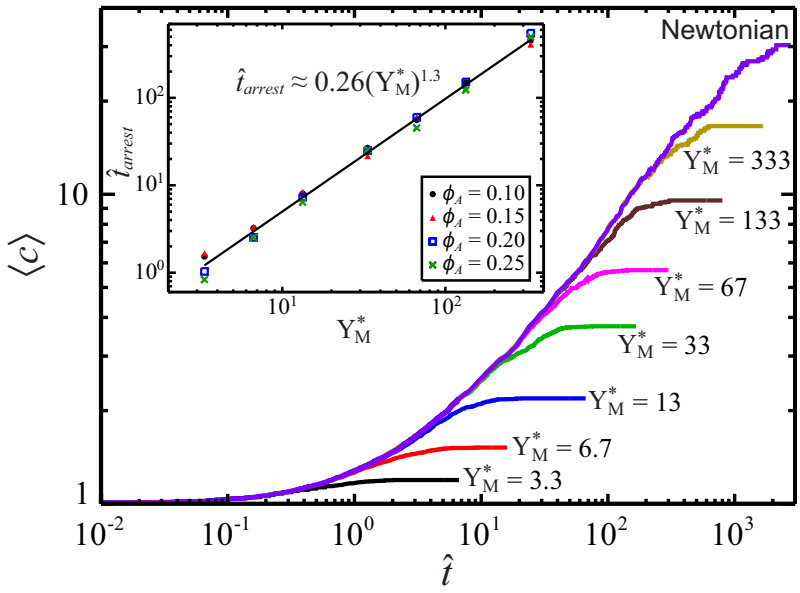

Fig. 5.3: *Average cluster size $\langle c \rangle$ of magnetically assembled structures as a function of time for various values of Y_M^*. The data is extracted from the same simulations as in Fig. 5.2, for which $\phi_A = 0.15$. As with the connectivity results, $\langle c \rangle$ generally increases with time, but chain growth is arrested when a yield stress matrix fluid is present. For all Y_M^*, $\langle c \rangle$ follows a common trajectory until structural arrest begins at a critical time (and a critical cluster size) that grows with Y_M^*. The arrest time, $\hat{t}_{arrest}$, defined as the time at which $\langle c \rangle$ becomes less than 90% of the Newtonian case, is shown in the inset as a function of Y_M^*. Results for four concentrations collapse onto a single common power law relationship.*

value, we plot $\hat{t}_{arrest}$ as a function of $\mathrm{Y_M^*}$ in the inset of Fig. 5.3 for four different concentrations of magnetic particles. The data follows a power law behavior, and least-squares fitting provides the relationship $\hat{t}_{arrest} \approx 0.26\,(\mathrm{Y_M^*})^{1.3}$, which is shown by the black line. The results for all four concentrations collapse onto this function, indicating that the arrest time is approximately independent of area fraction ϕ_A and that $\mathrm{Y_M^*}$ is the appropriate dimensionless group for characterizing the dynamics of structural arrest over a range of concentrations.

While the correspondence of statistical quantities like C_v, C_h, and $\langle c \rangle$ between the Newtonian and yield stress systems prior to arrest is a compelling indicator of a common trajectory of structural states, these averaged quantities do not uniquely identify the magnetically assembled structures. To more convincingly demonstrate that systems at finite values of $\mathrm{Y_M^*}$ truly pass through the same structural states as the Newtonian system, it is useful to examine the positions of each particle at a given time. A simple and instructive way to compare the positions of many particles simultaneously is to effectively subtract a snapshot of a simulated structure in a yield stress matrix fluid from that of the Newtonian system at the same dimensionless time. This can be accomplished

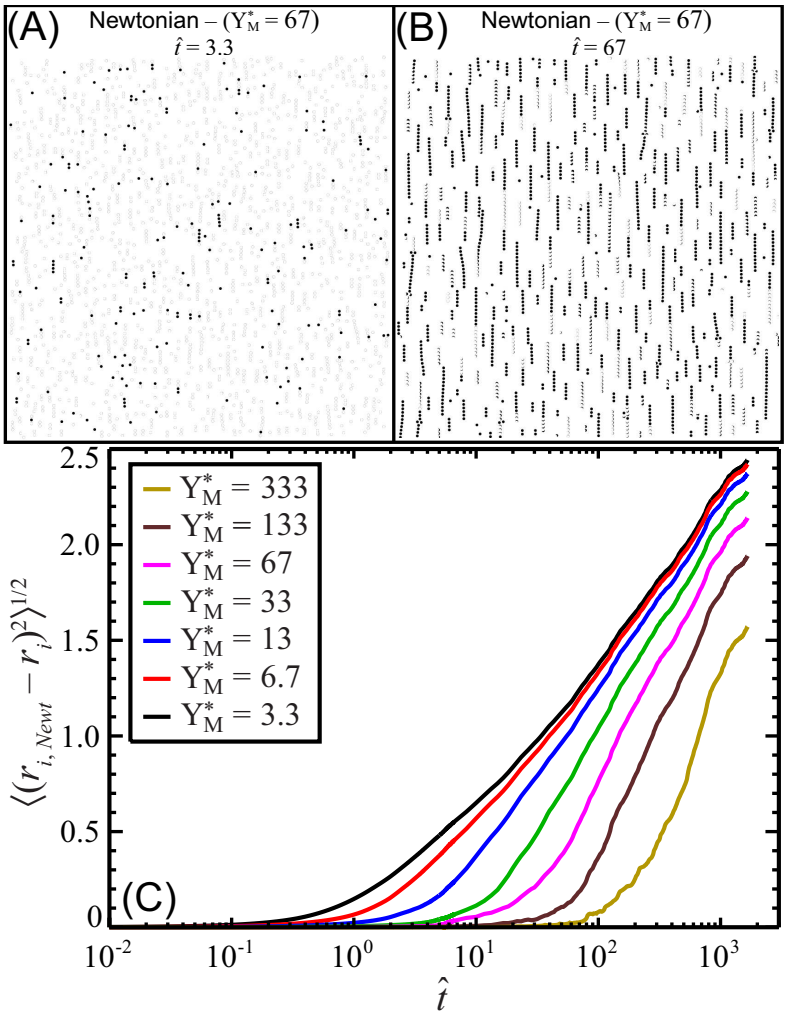

Fig. 5.4: *Comparison of the magnetically assembled structures for particle suspensions in Newtonian and yield stress matrix fluids at* $\phi_A = 0.15$. *The applied magnetic field is in the vertical direction. For times of (a)* $\hat{t} = 3.3$ *and (b)* $\hat{t} = 67$, *images of a Newtonian system are shown in black and images of a yield stress system at* $Y_M^* = 67$ *are overlaid in white. Therefore, any visible black structures indicate differences between the two systems. (a) and (b) correspond to times before and just after structural arrest in the yield stress system, respectively. At early times, the structures of the two systems are nearly identical, whereas significant deviations are apparent after the onset of structural arrest. In (c), the ensemble-averaged root mean square difference between particle positions in the Newtonian and yield stress system is plotted as a function of time for various values of* Y_M^*. *This measure of the deviation in the structure from the Newtonian case is essentially zero up to a critical time, then grows once the yield stress systems become arrested.*

by displaying the structure of the Newtonian system in black, and overlaying the structure of yield stress system in white, so that any visible black indicates structures that are not common between the two systems. Such comparisons between structures in a Newtonian matrix fluid and a matrix fluid at $Y_M^* = 67$ (starting from the same initial condition at $\phi_A = 0.15$) are shown in Fig. 5.4 at dimensionless times of (a) $\hat{t} = 3.3$ and (b) $\hat{t} = 67$, corresponding to times before and just after the onset of structural arrest in the yield stress system, respectively (here $\hat{t}_{arrest} = 60$). This effective subtraction of images almost completely obscures the structure at $\hat{t} = 3.3$, suggesting that the magnetically assembled structures of the Newtonian and yield stress systems are essentially the same prior to structural arrest. Note that the light gray outlines indicate that the white particles of the system at $Y_M^* = 67$ are overlaid almost exactly on the black particles of the Newtonian simulation. At $\hat{t} = 67$, however, there are significant deviations between the two systems, reflecting the fact that while chain-formation continues in the Newtonian system, structural evolution in the yield stress system has slowed almost to a halt. These images are consistent with the behavior presented in Figs. 5.2 and 5.3, and support the hypothesis that particles in the Newtonian and yield stress systems follow very similar trajectories up to the critical arrest time $\hat{t}_{arrest}$, after which the yield stress systems are quenched and deviations between the structures in the two systems grow. These deviations can be explored quantitatively by calculating the ensemble-averaged root mean square difference in particle position between the structures in the Newtonian matrix fluid and the yield stress matrix fluid. Denoted $\left\langle (r_{i,Newt} - r_i)^2 \right\rangle^{1/2}$, this quantity is zero if particles are in the same positions in the two systems, and grows as the structures diverge. Fig. 5.4(c) shows that for all Y_M^*, $\left\langle (r_{i,Newt} - r_i)^2 \right\rangle^{1/2} \approx 0$ up to a critical time that increases with Y_M^*. Subsequently, $\left\langle (r_{i,Newt} - r_i)^2 \right\rangle^{1/2}$ grows with time as the yield stress systems are arrested and structural development continues in the Newtonian system. These results provide further demonstration that the magnetically assembled structures in yield stress matrix fluids closely match those in Newtonian matrix fluids up to a critical time corresponding to the onset of structural arrest in the yield stress systems. In Fig. 5.5, the same data is plotted with the time axis re-scaled by the arrest time $\hat{t}_{arrest}$, shown in the inset of Fig. 5.3. We observe that deviations from the Newtonian system begin close to $\hat{t}/\hat{t}_{arrest} \approx 1$ for all values of Y_M^*, suggesting that deviations are a result of structural arrest in the systems with a yield stress matrix fluid.

The results presented thus far have implications in the design of structures generated via directed or self-assembly. While previous approaches to tuning particle assembly have focused on modifying particles (i.e., their shape, size, patterning, or chemical functionality [195]) or employing particle systems that respond to externally applied fields or stimuli [208], the concept of regulating assembled structures via matrix fluid rheology has yet to be elucidated. Our simulations suggest that by incorporating a matrix fluid with a yield stress, the chain structures that form in suspensions of dipolar particles in Newtonian matrix fluids can be arrested at essentially any point in their development. If the yield stress is sufficient to suppress sedimentation and Brownian motion, then arrested structures will be 'frozen' into place indefinitely even if the magnetic field is decreased or removed. Increasing the magnetic field (i.e., increasing Y_M^*) leads to the continuation of chain growth, and the resulting equilibrium value of $\langle c \rangle$ is approximately independent of the exact history as long as it is approached from below. This behavior is demonstrated in Fig. 5.6, where the time evolution of $\langle c \rangle$ is shown at $Y_M^* = 67$, starting from initial conditions with various degrees of chain development. The initial conditions correspond to the arrested states from the simulations in Fig.

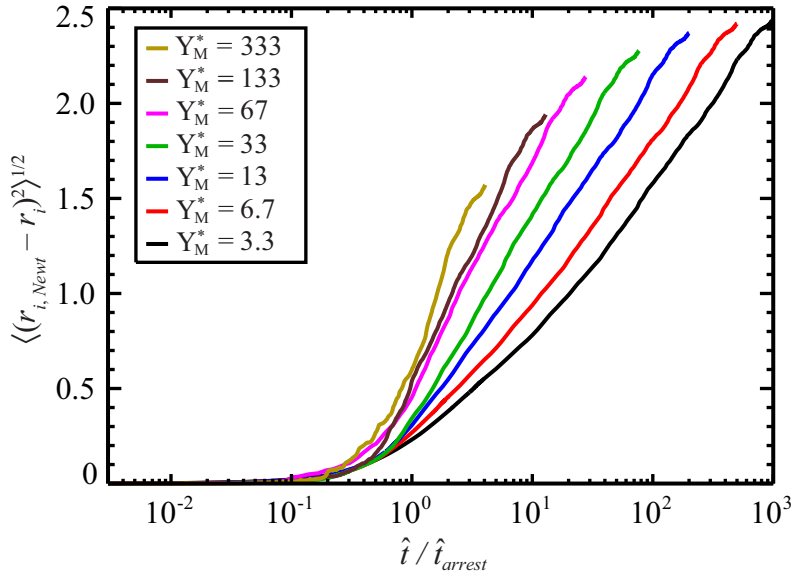

Fig. 5.5: *The data from Fig. 5.4(c) is re-plotted as a function of the dimensionless time scaled by the arrest time $\hat{t}_{arrest}$, as given in the inset of Fig. 5.3. Results are shown for the same concentration ($\phi_A = 0.15$) and Y_M^* values as in Fig. 5.4(c). Rescaling time in this way leads to an approximate collapse of the data at the time where significant deviations between particle positions in the Newtonian and yield stress systems begin to occur, indicating that this critical time scales with Y_M^* in a similar way as $\hat{t}_{arrest}$. Additionally, the fact that deviations between Newtonian and yield stress systems begin to grow close to $\hat{t}/\hat{t}_{arrest} \approx 1$ is evidence that the deviations are associated with structural arrest in the yield stress systems. Beyond $\hat{t}/\hat{t}_{arrest} \approx 1$, the data for different Y_M^* values diverge, so that re-scaling time by $\hat{t}_{arrest}$ is insufficient to collapse the data in this region.*

5.3 at $\mathrm{Y}_\mathrm{M}^* = \mathrm{Y}_\mathrm{M}^{*0}$. That is, a simulation is conducted starting from a random initial condition at $\mathrm{Y}_\mathrm{M}^* = \mathrm{Y}_\mathrm{M}^{*0}$ until structural arrest occurs. The resulting arrested configuration is set as the initial condition in a new simulation at $\mathrm{Y}_\mathrm{M}^* = 67$ with the time reset to 0. Therefore, the data in Fig. 5.6 corresponds to applying a step-change in Y_M^* to an arrested system. Fig. 5.6 shows that for all systems in which Y_M^* is increased (i.e., $\mathrm{Y}_\mathrm{M}^{*0} \leq 67$), the equilibrium value of $\langle c \rangle$ is approximately independent of the starting condition. However, if $\mathrm{Y}_\mathrm{M}^{*0} > 67$, the system remains arrested upon decreasing the magnetic yield parameter to $\mathrm{Y}_\mathrm{M}^* = 67$.

In order to confirm the results presented here, it will be necessary to show that experiments corroborate our observations. These experiments could be accomplished by examining the magnetic directed assembly of monodisperse spherical polymer-based superparamagnetic particles (available from a variety of vendors) in a yield stress matrix fluid. A simple yield stress fluid that exhibits negligible thixotropy, such as a Carbopol 'microgel', would be useful in exploring and demonstrating the basic phenomena of these field-activated suspensions [16, 173]. For example, a system at $\mathrm{Y}_\mathrm{M}^* \approx$

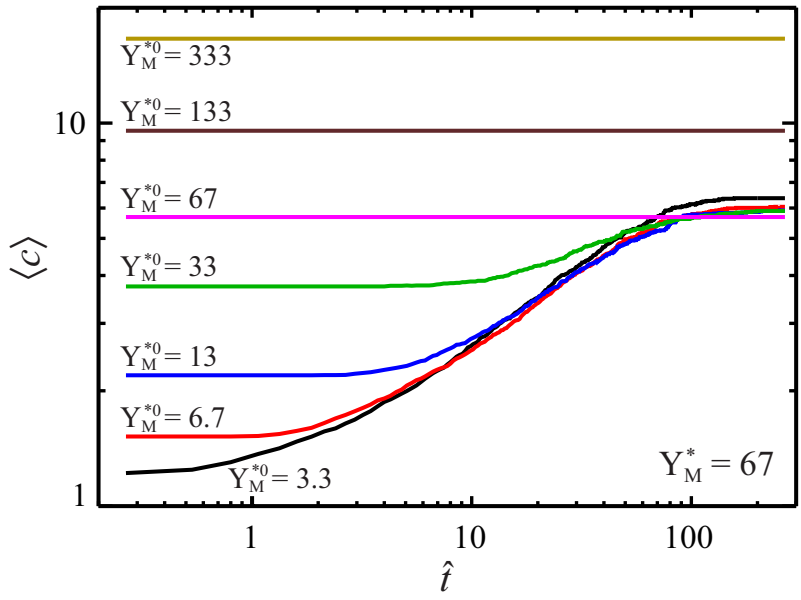

Fig. 5.6: *Time evolution of the average cluster size, $\langle c \rangle$, for systems at $\phi_A = 0.15$ and $Y_M^* = 67$, starting from various initial conditions with different values of $\langle c \rangle$. The starting configurations correspond to the arrested states at Y_M^* values of 3.3 (black), 6.7 (red), 13 (blue), 33 (green), 67 (pink), 133 (brown), and 333 (gold) from Fig. 5.3. In other words, the data above corresponds to the situation in which a system is simulated until equilibrium at $Y_M^* = Y_M^{*0}$ (as in Fig. 5.3), and the resulting equilibrium state is set as the starting configuration for a new simulation at $Y_M^* = 67$ with $\hat{t}$ reset to zero. Experimentally, this condition could be achieved by, for example, implementing a step-change to the magnetic field applied to an arrested system. Under these conditions, systems previously arrested at $Y_M^* < 67$ resume chain growth, eventually reaching a new equilibrium state with an average cluster size that is essentially independent of the starting configuration. We generally observe that the time necessary to escape the previous arrested state increases as the change in Y_M^* decreases, noting in particular that the green data, which corresponds to a transition from $Y_M^* = 33$ to $Y_M^* = 67$, remains constant for about 6 dimensionless time units before $\langle c \rangle$ begins to grow. The systems previously arrested at $Y_M^* > 67$ remain arrested upon decreasing Y_M^* to 67. These results demonstrate that the equilibrium value of $\langle c \rangle$ is essentially independent of history when increasing Y_M^* from an arrested state, but that the yield stress leads to a 'freezing' of the structure when Y_M^* is decreased.*

67 could be achieved by suspending 4.5 μm Dynabeads® superparamagnetic particles (Invitrogen, Carlsbad, CA) in a dilute Carbopol microgel with a yield stress of about 0.1 Pa [209] and by applying a uniform magnetic field of about 0.1 T (according to the magnetization data in Fig. 1.3).

With the exception of data for the critical arrest time shown in the inset of Fig. 5.3, all the results presented thus far have been at a representative concentration of $\phi_A = 0.15$. While systems at different concentrations exhibit qualitatively similar behavior (and, in particular, Fig. 5.3 shows that $\hat{t}_{arrest}$ is approximately independent of concentration), it would be beneficial to identify the scaling relationship between structural parameters and particle concentration. A simple approximation for the effect of particle concentration can be obtained by adjusting the characteristic length scale in the problem to reflect the concentration dependence of the average inter-particle distance in the random initial condition. For a 2-dimensional homogeneous spatial distribution of spherical particles with diameter d, the average inter-particle distance scales according to $d\phi_A^{-1/2}$. The effect of re-defining $d\phi_A^{-1/2}$ as the new characteristic length scale can be seen from the non-dimensionalization and rearrangement of Equation 5.9, for example. With this new scaling, the expression analogous to Equation 5.11 contains the product $\mathrm{Y}^*_{\mathrm{M}}\phi_A^2$ rather than simply $\mathrm{Y}^*_{\mathrm{M}}$ as in Equation 5.11. This motivates the definition of a re-scaled yield parameter, $\mathrm{Y}^*_{\mathrm{M},\phi}$, that incorporates the concentration dependence:

$$\mathrm{Y}^*_{\mathrm{M},\phi} = \mathrm{Y}^*_{\mathrm{M}}\phi_A^2 = \frac{\mu_0 C\left(\rho M\right)^2}{12\tau_{ys,0}}\phi_A^2 \tag{5.12}$$

This expression is a 2-dimensional analog of the definition given for $\mathrm{Y}^*_{\mathrm{M},\phi}$ in Table 1.2 and in Equation 4.6 in the previous chapter. By analogy with the yield parameter $\mathrm{Y}^*_{\mathrm{M}}$, we expect largely immobilized particles for $\mathrm{Y}^*_{\mathrm{M},\phi} \ll 1$, and extensive chain formation for $\mathrm{Y}^*_{\mathrm{M},\phi} \gg 1$. The equilibrium average cluster size, $\langle c \rangle_{eq}$, is shown as a function of $\mathrm{Y}^*_{\mathrm{M},\phi}$ in Fig. 5.7 for four particle area fractions. Despite the crude approximations used to arrive at the concentration scaling in Equation 5.12, plotting $\langle c \rangle_{eq}$ as a function of $\mathrm{Y}^*_{\mathrm{M},\phi}$ collapses data at different concentrations over almost two orders of magnitude of $\mathrm{Y}^*_{\mathrm{M},\phi}$. For $\mathrm{Y}^*_{\mathrm{M},\phi}$ values of about 0.2 to 7, a range in which both the matrix fluid yield stress and magnetic interactions are expected to play significant roles in the structure and dynamics, $\langle c \rangle_{eq}$ is given by the expression $\langle c \rangle_{eq} \approx 4.5\left(\mathrm{Y}^*_{\mathrm{M},\phi}\right)^{0.65}$ for $0.10 \leq \phi_A \leq 0.25$. The collapse of data for different concentrations indicates that Equation 5.12 provides an appropriate scaling for describing the equilibrium structure in this regime. The scaling breaks down, however, above about $\mathrm{Y}^*_{\mathrm{M},\phi} \approx 7$. In this regime, $\langle c \rangle_{eq}$ approaches the Newtonian values and for $\mathrm{Y}^*_{\mathrm{M},\phi} \approx 60$ the systems essentially behave as Newtonian. The gray band gives the range of $\langle c \rangle_{eq}$ values for Newtonian systems with concentrations $0.10 \leq \phi_A \leq 0.25$, which represents an upper bound for $\langle c \rangle_{eq}$ at a given concentration. For the Newtonian systems, $\langle c \rangle_{eq}$ exhibits a weak dependence on ϕ_A that precludes perfect collapse of the data at large values of $\mathrm{Y}^*_{\mathrm{M},\phi}$. Below about $\mathrm{Y}^*_{\mathrm{M},\phi} \approx 0.2$, the equilibrium structures consist almost entirely of un-yielded individual particles that are arrested immediately in their initial positions, so that $\langle c \rangle_{eq}$ approaches 1 for $\mathrm{Y}^*_{\mathrm{M},\phi} \ll 1$.

5.5 Conclusions and Outlook

The chain structures formed when dispersions of polarizable particles are subjected to a uniform magnetic field provide the basis for a number of emerging and promising technologies involving multi-phase complex fluids, including magnetorheological suspensions [64] and lab-on-a-chip sepa-

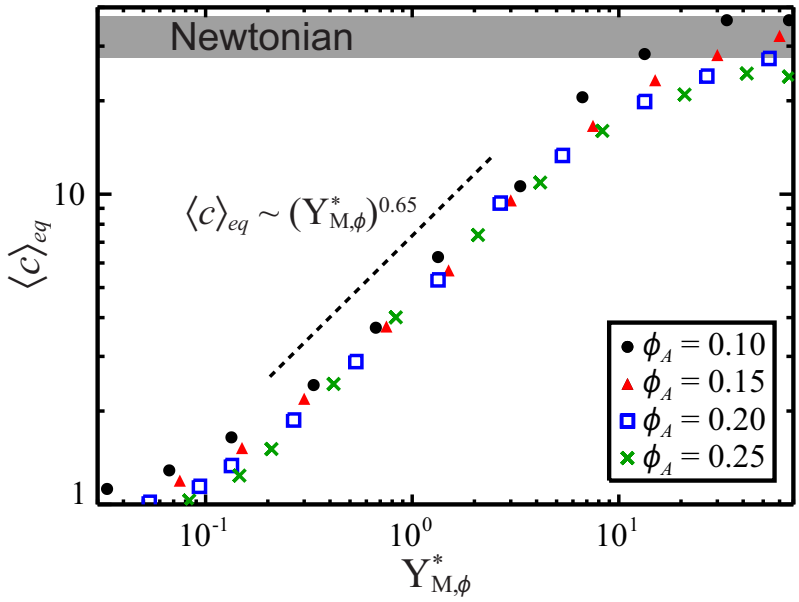

Fig. 5.7: *Equilibrium average cluster size, $\langle c \rangle_{eq}$, as a function of the concentration-scaled magnetic yield parameter, $Y^*_{M,\phi}$ (see Equation 5.12). Data for four concentrations of magnetic particles collapse onto a universal power law over two orders of magnitude in $Y^*_{M,\phi}$. Below about $Y^*_{M,\phi} = 0.2$, the equilibrium structures consist primarily of individual particles, so that $\langle c \rangle_{eq}$ approaches 1. The scaling begins to break down for $Y^*_{M,\phi}$ values grater than about 7, as Newtonian behavior is approached.*

ration techniques [200]. More generally, field-directed assembly of magnetic colloids and nanoparticles has been exploited to design and engineer highly-ordered functional materials [210], including materials with unique optical [199] or electrical properties [211]. In this chapter, we have used particle-level simulations to investigate a new approach for mediating the field-induced assembly of dipolar particles via control of the non-Newtonian properties of the matrix fluid. Specifically, we have demonstrated the ability of the matrix fluid yield stress to arrest chain formation and growth at a critical point along the Newtonian trajectory. The magnetic yield parameter Y^*_M (Equation 5.7), which characterizes the balance between inter-particle magnetic stresses and the matrix fluid yield stress, as well as the more general form $Y^*_{M,\phi}$ (Equation 5.12) incorporating concentration variations, have been identified as the appropriate dimensionless groups that govern the structure and dynamics in these systems. This work addresses important questions in the field of magnetorheological (MR) suspensions regarding the nature of the field-induced microstructure when yield stress matrix fluids are used to prevent magnetic particle sedimentation. Our observations indicate that for $Y^*_{M,\phi}$ values less than about 10, the matrix fluid yield stress will arrest chain growth and significantly decrease the size of clusters compared to the Newtonian case. Depending on the gap thickness in the rheometer or MR device, these truncated clusters will likely diminish or eliminate the gain in the yield stress anticipated upon application of the magnetic field, consistent with our

observations from bulk magnetorheology in Chapter 4. It is therefore desirable to operate yield-stress stabilized MR devices in the regime $\mathrm{Y}^*_{\mathrm{M},\phi} \gg 10$, where the structures giving rise to the MR effect closely resemble those in Newtonian matrix fluids.

While the arrested structures demonstrated here represent states along the Newtonian trajectory, the effect of the matrix fluid yield stress to 'freeze' structures in place could be exploited in more exotic systems to assemble and stabilize more complex anisotropic particle structures with high degrees of order. As long as the inter-particle forces in the final structured states are insufficient to overcome the matrix fluid yield stress (a balance that could be characterized by dimensionless groups analogous to those used here), the assembled structures will be stable essentially indefinitely. If necessary, the structures can be adjusted subsequently by increasing the forces on particles as desired, or, alternatively, by decreasing the yield stress. This approach is not limited to magnetic assembly, but is straightforwardly extendable to systems with other types of particle interactions or external forces (e.g., electric fields, optical tweezers, etc.). It is even possible that different assembly techniques could be applied sequentially, with the yield stress matrix fluid trapping particles in place between steps, allowing the complexity of achievable structures to be greatly expanded. Additionally, other types of non-Newtonian behavior in the matrix fluid could be similarly utilized to alter assembly. Though the task remains to confirm experimentally the behavior presented here, our results are physically reasonable and expected to be in at least qualitative agreement with experiments as long as the matrix fluid yield stress and inter-particle dipolar interactions are the dominant phenomena.

CHAPTER 6

Conclusions and Future Work

The work presented in this thesis represents a thorough rheological characterization of aqueous dispersions of Laponite® at bulk and microscopic length scales. We have also demonstrated the ability of these materials to address sedimentation problems in magnetorheological suspensions, and have explored the use of yield stress matrix fluids for tuning magnetic assembly. Our results will be of significant interest to rheologists, soft matter physicists, and MEMS researchers, as well as industrial formulation engineers and product developers.

6.1 Length-scale–dependent Linear Rheology of Laponite® Dispersions

We began in Chapter 2 by exploring the gelation of dilute (1 w%) aqueous dispersions of Laponite® using a combination of bulk rheology and Multiple Particle Tracking (MPT) microrheology [89]. While previous reports indicated discrepancies between rheological properties and gelation times measured at bulk and microscopic scales [59], our MPT microrheology results over a range of probe sizes show that length-scale–dependent rheology is a general feature of aqueous Laponite® gels. We find that the use of smaller probes is accompanied by the observation of significantly lower viscoelastic moduli and longer gelation times. To explain this behavior, we hypothesize that as the material ages, a porous network structure develops that traps larger probe particles, while smaller probes generally have more time to diffuse relatively unhindered through pores and more weakly gelled regions. In agreement with this picture, we find that probe dynamics exhibit significant

spatial heterogeneity, from which a novel characteristic length scale is determined. Finally, using theory and simulation we clarify the relationship between the correlated probe displacements reported by previous authors [59] and the elasticity of the material.

This work will impact the understanding of the gelation behavior and microstructure of aqueous Laponite® dispersions. The microstructural length scales we measure using MPT are generally consistent with previous scattering measurements of cluster sizes in aqueous Laponite® dispersions [103], and indicate that for the experimental conditions in our study the resulting phase can be more aptly characterized as a 'gel' than a 'repulsive glass', in agreement with previous reports [43]. Our analysis also demonstrates novel methods for elucidating microstructural length scales and quantifying features of the probe trajectories that could be applied to a variety of complex fluids. Finally, the length-scale–dependent behavior we observe will be of interest to industrial formulation engineers and product developers using Laponite® as a rheological modifier. For many commercial applications of Laponite®, such as paints and oil-drilling fluids, the rheological properties on microscopic length scales can be important for proper function.

There are a number of interesting issues motivated by this work that could be addressed in the future. The primary conclusion of this study, that dispersion rheological properties depend on the length scale that is probed, could be examined in greater depth through the use of two-point microrheology [130]. By analyzing the correlated motions of two neighboring probe particles as a function of separation distance, the length-scale dependence of the rheology could be more explicitly studied. Also, the task remains to develop a suitable quantitative particle-level model for the gelation mechanism of aqueous Laponite® dispersions that is consistent with the probe-size–dependent behavior we observe. Another future opportunity is further clarification of the physical interpretation of the correlations between successive probe particle displacements, $\langle x_{12} \rangle$. Our study has shown that probes diffusing in a continuum material with no 'microstructure' but finite elasticity can exhibit non-zeros values of $\langle x_{12} \rangle$. It would be interesting to examine these correlations for other model systems, including probes diffusing in Newtonian fluids confined to pores, to see if imposed microstructural length scales can be extracted from the analysis of $\langle x_{12} \rangle$. Finally, it would be interesting to repeat this study in different areas of the phase space shown in Fig. 1.7, and to examine how microrheological results change as the interactions between Laponite® platelets are adjusted via the concentration of added salt.

6.2 Nonlinear Microrheology of Laponite® Dispersions

In Chapter 3, the comparison between the bulk and micro-scale rheology of aqueous Laponite® dispersions was extended to large deformation experiments (i.e., nonlinear rheology) at higher concentrations (1.5 to 2.5 w%) [90]. In this work, a magnetic tweezer microrheology device is thoroughly characterized in terms of the accessible stresses, the applied magnetic fields, and the range of measurable shear rates and viscosities. Magnetic probe particles sufficiently close to the tweezers exhibit rapid acceleration towards the tweezer surface, allowing measurement of the strong shear-thinning behavior of the viscosity. In contrast, probes at a farther distance undergo only a slow creep, appearing to be 'jammed' in the gel. This distinction between mobile and jammed probes is used to demonstrate the first use of magnetic tweezers to measure yield stresses on the microscopic scale. We additionally provide the first comparison between bulk and micro-scale yield stress measurements, finding good agreement provided that a geometric factor is included that approximately corrects for the differences in flow kinematics between the two measurements. Both

yield stress measures grow approximately logarithmically with age time.

Since this work represents only the second report of yield stress measurements on the microscopic scale [139] and comes at a time of growing interest in active and nonlinear microrheology [109], it will be of wide appeal to the rheology and microrheology communities. Additionally, the agreement between bulk and micro-scale yield stresses for Laponite® concentrations greater than or equal to 2.0 w% expands upon our results from Chapter 2, implying that the characteristic size of microstrucutral features (for example, the characteristic pore size) decreases as the Laponite® concentration increases. The results of this project will assure industrial formulators that bulk rheological measurements are representative of local micro-scale properties for sufficient Laponite® concentration.

There are a number of ways in which the magnetic tweezer device used in this project could be optimized for future work. Ideally, a second-generation device would incorporate more precise micromachining at the tip, which would reduce the variation in the stress near the tip where the stresses are largest, as well as a high-camera to capture more of the shear-thinning behavior during which particles accelerate rapidly. If possible, probe particles with higher saturation magnetizations could also be obtained, allowing higher stresses on particles to be achieved. These adjustments would expand the dynamic range of the instrument without modifying the design of the magnetic core. Future experiments with this device on aqueous Laponite® dispersions could address the probe size dependence in a manner similar to the MPT experiments in this thesis. For 2.0 or 2.5 w% Laponite®, is there a critical probe size below which agreement between bulk and micro-scale measurements of the yield stress breaks down? Our hypothesis is that such a critical probe size must exist between a probe diameter of 4.5 μm (the probe size in this magnetic tweezer study) and the size of Laponite® platelets ($\sim$ 30 nm). Additionally, our work has highlighted the importance of taking into account differences between the geometry and flow kinematics in bulk and micro-scale experiments. If the bulk flow kinematics could be more closely mimicked at the micro-scale, perhaps through the use of disk-, plate-, or rod-shaped probe particles, bulk and micro-scale measurements could be more directly compared. Finally, there are other aspects of the nonlinear rheology of aqueous Laponite® dispersions that would be very interesting to explore with this device on the microscopic scale. For example, perhaps shear rejuvenation could be studied by comparing the behavior of particles that move individually towards the tip with those that follow in another's path through 'rejuvenated' fluid. Also, it is possible that the relaxation of probes *after* switching off the magnetic field could reveal information about jamming and elastic recoil of the Laponite® dispersion.

6.3 Magnetic Particles in Yield Stress Matrix Fluids

Taking advantage of the yield stress behavior of aqueous Laponite® dispersions to inhibit sedimentation of magnetic particles, we examined magnetorheology in matrix fluids composed of aqueous Laponite® dispersions in Chapter 4. We find that sedimentation is prevented and our results indicate that the matrix fluid yield stress has a negligible effect on the magnetorheology for sufficient applied magnetic fields. This behavior is understood in terms of a dimensionless magnetic yield parameter, $Y^*_{M,\phi}$, that characterizes the balance between inter-particle magnetic stresses and the matrix fluid yield stress. Despite the thixotropic nature of the aqueous Laponite® matrix fluid, field-induced dynamic and static yield stress measurements are in agreement for $Y^*_{M,\phi} \gtrsim 10$. A master curve was developed that relates the field-induced yield stress to the particle magnetization and

the magnetic particle concentration, amounting to a concentration–magnetization superposition that is expected to be generally applicable for essentially any type of magnetic particle. Chapter 5 describes simulation studies of the field-induced structure of dipolar particle suspensions in a simple Bingham yield stress matrix fluid. We find that the yield stress results in an arrest of chain growth when the separation distance to neighboring particles and chains is too large to cause yielding, leading to shorter chains at equilibrium than in the case of Newtonian matrix fluids. Also, we find that the 'zippering' mechanism for lateral aggregation of chains is suppressed, resulting in lower horizontal connectivity of chains at equilibrium when a yield stress is present.

The negligible effect of the matrix fluid yield stress on magnetorheological properties for sufficient magnetic fields is likely to be a result welcomed by formulators of MR fluids. As long as $Y^*_{M,\phi} \gg 1$, which is frequently satisfied at the high field strengths and particle concentrations used in most commercial MR applications, the yield stress of the matrix fluid can be optimized to meet other design demands without significantly disrupting the behavior of the field-activated material. Additionally, this work clarifies previous research on MR suspensions in yield stress matrix fluids by explicitly measuring both the field-induced static and dynamic yield stresses and showing that they are equivalent for sufficient values of $Y^*_{M,\phi}$. The magnetorheological master curves we present will aid in the development of MR fluids and MR devices by providing a simple, analytical relationship between the field-induced yield stress and system parameters. Finally, our simulation work examines the microstructure of MR suspensions in a previously unexplored regime that could be useful in novel technologies. In particular, the concept of tuning particle assembly via the rheological properties of the matrix fluid will be of significant interest to MEMS researchers.

Recent work has highlighted the opportunity for using squeeze flows in MR devices and the need to quantitatively characterize squeeze flow magnetorheology [64, 187]. Since yield stress matrix fluids could play a similar role in preventing particle sedimentation in squeeze flow MR devices, an important question to address for future work in this area is the effect of a matrix fluid yield stress on MR behavior in squeeze flows. For thixotropic matrix fluids like aqueous Laponite® dispersions, it is also important to understand whether the suspension remains resistant to sedimentation even after the application of large shear rates for long periods of time (which would tend to 'rejuvenate' the matrix fluid). Additionally, the simulations of magnetic assembly in this thesis have provided motivation and basic groundwork for many potential future studies. In addition to extending results to 3-D simulations or incorporating more complex rheological constitutive relations that more appropriately capture real matrix fluid behavior, future computational work could more thoroughly address the link between the simulated microstructures and the predicted field-responsive rheology. Finally, analogous experiments in quasi-2D slits should be performed on suspensions of superparamagnetic particles in yield stress matrix fluids to check that the observed microstructures match those obtained in simulations.

Appendix A

Three-point Correlation Calculations

A.1 Three-point Correlations in a Kelvin–Voigt Material

To derive expressions for the correlations between successive displacements $\langle x_{12} \rangle$ and the b parameter for probe particles undergoing Brownian motion in a Kelvin–Voigt material, we begin with the autocorrelation function of the probe position $\mathbf{r}(t)$ over a lag time τ.

$$C_{\mathbf{r}}(\tau) = \langle \mathbf{r}(t+\tau) \cdot \mathbf{r}(t) \rangle - \langle \mathbf{r}(t) \rangle^2 \tag{A.1}$$

Here brackets represent time averages. For successive probe displacements $\mathbf{r}_{01}$ and $\mathbf{r}_{12}$, each over a lag time τ, it can be shown that

$$\langle \mathbf{r}_{01} \cdot \mathbf{r}_{12} \rangle = 2C_{\mathbf{r}}(\tau) - C_{\mathbf{r}}(2\tau) - C_{\mathbf{r}}(0) \tag{A.2}$$

$$\langle \mathbf{r}_{01} \cdot \mathbf{r}_{01} \rangle = 2C_{\mathbf{r}}(0) - 2C_{\mathbf{r}}(\tau) \tag{A.3}$$

Here we have used the fact that $\langle \mathbf{r}(t) \rangle$ in a Kelvin–Voigt material (i.e. the material is a viscoelastic solid). In order to proceed, we make the following approximations. First, we approximate $\langle \|\mathbf{r}_{01}\| \rangle = \left\langle \sqrt{\mathbf{r}_{01} \cdot \mathbf{r}_{01}} \right\rangle \approx \sqrt{\langle \mathbf{r}_{01} \cdot \mathbf{r}_{01} \rangle}$ where we have taken the square root outside of the average. Second, noting the form of $\langle x_{12} \rangle$ versus r_{01} in Equation 2.6, we make the so-called 'Peterlin Approximation'

that the average of a quotient is approximately equal to the quotient of the averages:

$$\langle x_{12}\rangle = \left\langle \frac{\mathbf{r}_{01}\cdot\mathbf{r}_{12}}{\|\mathbf{r}_{01}\|}\right\rangle = \left\langle \frac{\mathbf{r}_{01}\cdot\mathbf{r}_{12}}{\sqrt{\mathbf{r}_{01}\cdot\mathbf{r}_{01}}}\right\rangle \approx \frac{\langle \mathbf{r}_{01}\cdot\mathbf{r}_{12}\rangle}{\left\langle\sqrt{\mathbf{r}_{01}\cdot\mathbf{r}_{01}}\right\rangle} \approx \frac{\langle \mathbf{r}_{01}\cdot\mathbf{r}_{12}\rangle}{\sqrt{\langle \mathbf{r}_{01}\cdot\mathbf{r}_{01}\rangle}} \tag{A.4}$$

Combining these approximations with Equations A.2 and A.3 and using the fact that $r_{01} = \langle\|\mathbf{r}_{01}\|\rangle$, we arrive at an expression for $\langle x_{12}\rangle$ in terms of $C_{\mathbf{r}}(\tau)$ and r_{01}:

$$\langle x_{12}\rangle = \frac{2C_{\mathbf{r}}(\tau) - C_{\mathbf{r}}(2\tau) - C_{\mathbf{r}}(0)}{2C_{\mathbf{r}}(0) - 2C_{\mathbf{r}}(\tau)} r_{01} \tag{A.5}$$

This expression shows a linear variation between $\langle x_{12}\rangle$ and r_{01} of the form $\langle x_{12}\rangle = -br_{01}$. The expression for b in terms of $C_{\mathbf{r}}(\tau)$ is therefore

$$b = -\frac{2C_{\mathbf{r}}(\tau) - C_{\mathbf{r}}(2\tau) - C_{\mathbf{r}}(0)}{2C_{\mathbf{r}}(0) - 2C_{\mathbf{r}}(\tau)} \tag{A.6}$$

This expression can be simplified by recognizing that $C_{\mathbf{r}}(\tau)$ is the inverse Fourier transform of the power spectral density of the probe position $S^*_{\mathbf{r}}(\omega)$, given in Equation 2.8 for Brownian probes embedded in a Kelvin–Voigt material:

$$C_{\mathbf{r}}(\tau) = \frac{(\lambda_+ + \lambda_-)\,k_BT}{4\pi aG}\left(\frac{e^{-\tau/\lambda_+} + e^{-\tau/\lambda_-}}{\lambda_+ + \lambda_-} + \frac{e^{-\tau/\lambda_+} - e^{-\tau/\lambda_-}}{\lambda_+ - \lambda_-}\right) \tag{A.7}$$

where the roots $\lambda_\pm$ are given in Equation 2.9. In realistic situations, the inertial time scale for the probe is many orders of magnitude less than the relaxation time of the material, so that $\lambda_I/\lambda_V \ll 1$. In this limit, $\lambda_+ \approx \lambda_V$ and $\lambda_- \approx 0$. Applying the inertia-less limit to Equation A.7 we obtain

$$C_{\mathbf{r}}(\tau) = \frac{k_BT}{2\pi aG}\exp(-\tau/\lambda_V) \tag{A.8}$$

The autocorrelation function of the probe position decays with a characteristic time constant λ_V. Finally, substituting this equation into Equation A.6 yields a simple expression for b that matches Equation 2.12.

$$b = \frac{1}{2}\left[1 - \exp(-\tau/\lambda_V)\right] \tag{A.9}$$

$\langle x_{12}\rangle$ is then given by

$$\langle x_{12}\rangle = -\frac{1}{2}\left[1 - \exp(-\tau/\lambda_V)\right] r_{01} \tag{A.10}$$

which matches Equation 2.11. In the limit $\tau/\lambda_V \ll 1$, $b \to 0$ and there are no correlations between successive probe particle displacements. The lag time is not long enough for probe motions to be affected by the elasticity of the material. In the limit $\tau/\lambda_V \gg 1$, $b \to 0.5$ and the successive displacements of probe particles are significantly correlated. In this case, probe motions are highly influenced by the elasticity of the material over the time scale of the lag time τ. Since a number of approximations were made to obtain these expressions, a Brownian dynamics (BD) simulation was conducted in order to check the theoretical results. The details of the simulation are given below.

A.2 Simulations of Probe Diffusion in a Kelvin–Voigt Material

The equation of motion for a Brownian probe particle in a Kelvin–Voigt material is given in Equation 2.7. We wish to solve this stochastic differential equation using Brownian dynamics (BD). Physical insight and computational efficiency can be gained by first using appropriate length and time scales to make the equation of motion dimensionless. We invoke the equipartition theorem for a tethered Brownian spring to obtain the scaling relationship

$$GL^2 \sim \frac{k_B T}{a} \tag{A.11}$$

where L is the characteristic length scale at which Brownian and elastic forces on the probe particle (having radius a) balance. Rearranging this expression and substituting $G = \eta/\lambda_V$ and $D = k_B T/6\pi\eta a$ gives the length scale L to be

$$L = \sqrt{D\lambda_V} \tag{A.12}$$

If we now take the characteristic time scale t^* to be the characteristic time for the probe to diffuse the distance L, we see from Equation A.12 that $t^* = \lambda_V$. Applying this scaling, we obtain a dimensionless equation of motion:

$$\frac{\lambda_I}{\lambda_V}\ddot{\hat{\mathbf{r}}}\left(\hat{t}\right) + \dot{\hat{\mathbf{r}}}\left(\hat{t}\right) + \hat{\mathbf{r}}\left(\hat{t}\right) = \frac{\mathbf{f}\left(\hat{t}\right)}{6\pi a G}\sqrt{\frac{1}{\lambda_V D}} \tag{A.13}$$

where $\hat{\mathbf{r}}\left(\hat{t}\right) = \mathbf{r}\left(t\right)/L$ and over-dots represent derivatives with respect to the dimensionless time variable $\hat{t} = t/\lambda_V$. The right-hand side of Equation A.13 is a dimensionless Brownian force $\hat{\mathbf{f}}\left(\hat{t}\right)$:

$$\hat{\mathbf{f}}\left(\hat{t}\right) = \frac{\mathbf{f}\left(\hat{t}\right)}{6\pi a G}\sqrt{\frac{1}{\lambda_V D}} = \frac{\mathbf{f}\left(\hat{t}\right)}{k_B T/L} \tag{A.14}$$

This stochastic force is expressed at each dimensionless time step $\hat{t} = \hat{t}_n$ in terms of a random number $[r_n]$ taken from a uniform distribution with $[r_n] \in \left[-\frac{1}{2}, \frac{1}{2}\right]$.

$$\hat{\mathbf{f}}\left(\hat{t}\right) = \sqrt{\frac{24}{\Delta\hat{t}}}\,[r_n] \tag{A.15}$$

Here $\Delta\hat{t} = \Delta t/\lambda_V$ is the dimensionless time increment. Substituting this expression into the right-hand side of Equation A.13, we obtain a dimensionless equation of motion that can be solved numerically in Euler integration steps:

$$\frac{\lambda_I}{\lambda_V}\ddot{\hat{\mathbf{r}}} + \dot{\hat{\mathbf{r}}} + \hat{\mathbf{r}} = \sqrt{\frac{24}{\Delta\hat{t}}}\,[r_n] \tag{A.16}$$

If we now take the inertia-less limit $\lambda_I/\lambda_V \ll 1$, then the resulting dimensionless equation of motion is

$$\dot{\hat{\mathbf{r}}} + \hat{\mathbf{r}} = \sqrt{\frac{24}{\Delta\hat{t}}}\,[r_n] \tag{A.17}$$

There are no free parameters in this equation, indicating that the simulation needs only to be performed once in dimensionless coordinates in order to obtain a probe particle trajectory that can subsequently be analyzed for specific correlations. Therefore correlations between successive displacements should only depend on the dimensionless lag time τ/λ_V. We run the simulation with a time step of $\Delta\hat{t} = 0.001$ and a total of 5.0×10^8 time steps, exploring values of τ/λ_V from 10^{-2} to 10^3.

Bibliography

[1] Reiner, M. *Phys. Today* **1964**, *17*, 62.

[2] Larson, R. G. *The Structure and Rheology of Complex Fluids*; Oxford University Press: New York, 1999.

[3] Morrison, F. A. *Understanding Rheology*; Oxford University Press: New York, 2001.

[4] Barnes, H. A.; Hutton, J. F.; Walters, K. *An Introduction to Rheology*; Elsevier., 1989.

[5] Chhabra, R.; Richardson, J. *Non-Newtonian Flow and Applied Rheology: Engineering Applications*, 2nd ed.; Elsevier.

[6] Hartt, W.; Bacca, L.; Baer, T.; Majmudar, T. S.; Thomas, O. Piling up of high speed, yield stress fluid jets: Experimentally observed flow regimes. *Presented at the 81st Annual Meeting of The Society of Rheology, Madison, WI, USA*, 2009.

[7] *Rheology for Polymer Melt Processing*; Piau, J.-M., Agassant, J.-F., Eds.; Elsevier: New York, 1996.

[8] Bird, R. B.; Armstrong, R. C.; Hassager, O. *Dynamics of Polymeric Liquids: Volume 1 Fluid Mechanics*; Wiley: New York, 1987; Vol. 1: Fluid Mechanics.

[9] Chambon, F.; Winter, H. H. *J. Rheol.* **1987**, *31*, 683–697.

[10] Helgeson, M. E.; Hodgdon, T. K.; Kaler, E. W.; Wagner, N. J.; Vethamuthu, M.; Ananthapadmanabhan, K. P. *Langmuir* **2010**, *26*, 8049–8060.

[11] Macosko, C. W. *Rheology: Principles, Measurements and Applications*; Wiley: New York, 1994.

[12] Deshmukh, S. S. *Ph.D. Thesis*, Massachusetts Institute of Technology, 2006.

[13] Wagner, N. J.; Brady, J. F. *Phys. Today* **2009**, *62*, 27–32.

[14] Barnes, H. A. *J. Non-Newtononian Fluid Mech.* **1999**, *181*, 133–178.

[15] Barnes, H. A. *Appl. Rheol.* **2007**, *17*, 43110.

[16] Møller, P. C. F.; Fall, A.; Bonn, D. *Europhys. Lett.* **2009**, *87*, 6.

[17] Nguyen, Q. D.; Boger, D. V. *Annu. Rev. Fluid Mech.* **1992**, *24*, 47–88.

[18] Møller, P. C. F.; Mewis, J.; Bonn, D. *Soft Matter* **2006**, *2*, 274–283.

[19] Cicuta, P.; Donald, A. M. *Soft Matter* **2007**, *3*, 1449–1455.

[20] MacKintosh, F. C.; Schmidt, C. F. *Curr. Opin. Colloid Interface Sci.* **1999**, *4*, 300–307.

[21] Waigh, T. A. *Rep. Prog. Phys.* **2005**, *68*, 685–742.

[22] Liu, J.; Gardel, M. L.; Kroy, K.; Frey, E.; Hoffman, B. D.; Crocker, J. C.; Bausch, A. R.; Weitz, D. A. *Phys. Rev. Lett.* **2006**, *96*, 118104.

[23] Levine, A. J.; Lubensky, T. C. *Phys. Rev. E* **2001**, *63*, 041510.

[24] Gardel, M. L.; Valentine, M. T.; Weitz, D. A. Microrheology. In *Microscale Diagnostic Techniques*; Breuer, K. S., Ed.; Springer Verlag: New York, 2005; pp 1–55.

[25] http://www.bris.ac.uk/Depts/Synaptic/info/imaging/figs/fluomicro.gif.

[26] Crocker, J. C.; Grier, D. G. *J. Coll. Int. Sci.* **1996**, *179*, 298–310.

[27] http://web.mit.edu/savin/Public/.Tutorial/.

[28] Savin, T.; Doyle, P. S. *Biophys. J.* **2005**, *88*, 623–638.

[29] Khair, A. S.; Brady, J. F. *J. Rheol.* **2008**, *52*, 165–196.

[30] Shevkoplyas, S. S.; Siegel, A. C.; Westervelt, R. M.; Prentiss, M. G.; Whitesides, G. M. *Lab Chip* **2007**, *7*, 1294–1302.

[31] Wilhelm, C.; Elias, F.; Browaeys, J.; Ponton, A.; Bacri, J.-C. *Phys. Rev. E* **2002**, *66*, 021502.

[32] Bausch, A. R.; Ziemann, F.; Boulbitch, A. A.; Jacobson, K.; Sackmann, E. *Biophys. J.* **1998**, *75*, 2038–2049.

[33] Hough, L.; Ou-Yang, H. *J. Nanopart. Res.* **1999**, *1*, 495–499.

[34] Weitz, D. A.; Pine, D. J. Diffusing-Wave Spectroscopy. In *Dynamic Light Scattering*; Brown, W., Ed.; Oxford University Press: Oxford, 1993; pp 652–721.

[35] Ewoldt, R.; Clasen, C.; Hosoi, A. E.; McKinley, G. H. *Soft Matter* **2007**, *3*, 634–643.

[36] Bonn, D.; Coussot, P.; Huynh, H. T.; Bertrand, F.; Debrégeas, G. *Europhys. Lett.* **2002**, *59*, 786–792.

[37] Bonn, D.; Tanase, S.; Abou, B.; Tanaka, H.; Meunier, J. *Phys. Rev. Lett.* **2002**, *89*, 015701.

[38] Bonn, D.; Tanaka, H.; Wegdam, G.; Kellay, H.; Meunier, J. *Europhys. Lett.* **1999**, *45*, 52–57.

[39] Abou, B.; Bonn, D.; Meunier, J. *Phys. Rev. E* **2001**, *64*, 021510.

[40] Tanaka, H.; Meunier, J.; Bonn, D. *Phys. Rev. E* **2004**, *69*, 031404.

[41] Luckham, P. F.; Rossi, S. *Adv. Coll. Int. Sci.* **1999**, *82*, 43–92.

[42] *Laponite product information*, Rockwood Additives: Southern Clay Products, Inc.

[43] Ruzicka, B.; Zaccarelli, E. *Soft Matter* **2011**, *7*, 1268–1286.

[44] van Olphen, H. *An Introduction to Clay Colloid Chemistry*; Wiley: New York, 1977.

[45] Mourchid, A.; Delville, A.; Lambard, J.; LéColier, E.; Levitz, P. *Langmuir* **1995**, *11*, 1942–1950.

[46] Kroon, M.; Vos, W. L.; Wegdam, G. H. *Phys. Rev. E* **1998**, *57*, 1962.

[47] Tawari, S. L.; Koch, D. L.; Cohen, C. *J. Coll. Int. Sci.* **2001**, *240*, 54–66.

[48] Martin, C.; Pignon, F.; Piau, J.-M.; Magnin, A.; Lindner, P.; Cabane, B. *Phys. Rev. E* **2002**, *66*, 021401.

[49] Mongondry, P.; Nicolai, T.; Tassin, J. F. *J. Coll. Int. Sci.* **2004**, *275*, 191–196.

[50] Thompson, D. W.; Butterworth, J. T. *J. Coll. Int. Sci.* **1992**, *151*, 236–243.

[51] Mourchid, A.; Levitz, P. *Phys. Rev. E* **1998**, *57*, R4887–R4890.

[52] Jabbari-Farouji, S.; Wegdam, G. H.; Bonn, D. *Phys. Rev. Lett.* **2007**, *99*, 065701.

[53] Bonn, D.; Kellay, H.; Tanaka, H.; Wegdam, G.; Meunier, J. *Langmuir* **1999**, *15*, 7534–7536.

[54] Baghdadi, H. A.; Parrella, J.; Bhatia, S. R. *Rheol. Acta* **2007**, *47*, 349–357.

[55] Meeten, G. H. *Rheol. Acta* **2000**, *39*, 399–408.

[56] Meeten, G. H. *Rheol. Acta* **2001**, *40*, 279–288.

[57] Jabbari-Farouji, S.; Mizuno, D.; Atakhorrami, M.; MacKintosh, F. C.; Schmidt, C. F.; Eiser, E.; Wegdam, G. H.; Bonn, D. *Phys. Rev. Lett.* **2007**, *98*, 108302.

[58] Jabbari-Farouji, S.; Atakhorram, M.; Mizuno, D.; Eiser, E.; Wegdam, G.; MacKintosh, F.; Bonn, D.; Schmidt, C. *Phys. Rev. E* **2008**, *78*, 061402.

[59] Oppong, F. K.; Coussot, P.; de Bruyn, J. R. *Phys. Rev. E* **2008**, *78*, 10.

[60] Sollich, P.; Lequeux, F.; Hébraud, P.; Cates, M. E. *Phys. Rev. Lett.* **1997**, *78*, 2020.

[61] Sollich, P. *Phys. Rev. E* **1998**, *58*, 738.

[62] Fielding, S. M.; Sollich, P.; Cates, M. E. *J. Rheol.* **2000**, *44*, 323–369.

[63] Shahin, A.; Joshi, Y. M. *Phys. Rev. Lett.* **2011**, *106*, 038302.

[64] de Vicente, J.; Klingenberg, D. J.; Hidalgo-Alvarez, R. *Soft Matter* **2011**, *7*, 3701–3710.

[65] Rabinow, J. *AIEE Trans.* **1948**, *67*, 1308–1315.

[66] Spencer, B. F.; Dyke, S. J.; Sain, M. K.; Carlson, J. D. *J. Eng. Mech.-ASCE* **1997**, *123*, 230–238.

[67] Dyke, S. J.; Spencer, B. F.; Sain, M. K.; Carlson, J. D. *Smart Mater. Struct.* **1996**, *5*, 565–575.

[68] Carlson, J. D.; Matthis, W.; Toscano, J. R. Smart prosthetics based on magnetorheological fluids. In *Smart Structures and Materials 2001: Industrial and Commercial Applications of Smart Structures Technologies*; Spie-Int Soc Optical Engineering: Bellingham, 2001; Vol. 4332, pp 308–316.

[69] Kordonski, W. I.; Golini, D. *J. Intell. Mater. Syst. Struct.* **1999**, *10*, 683–689.

[70] Zitha, P. L. J. *Method of drilling with magnetorheological fluid*, 2004, US patent number 7021406.

[71] Klingenberg, D. J. *AIChE J.* **2001**, *47*, 246–249.

[72] Parthasarathy, M.; Klingenberg, D. J. *Mat. Sci. Eng. R* **1996**, *17*, 57–103.

[73] Goncalves, F. D.; Koo, J.-H.; Ahmadian, M. *Shock Vib. Digest* **2006**, *38*, 203–219.

[74] Bombard, A. J. F.; Knobel, M.; Alcantara, M. R.; Joekes, I. *J. Intel. Mat. Sys. Str.* **2002**, *13*, 471–478.

[75] Tao, R. *J. Phys.-Condens. Mat.* **2001**, *13*, R979–R999.

[76] Haghgooie, R. Ph.D. thesis, Massachusetts Institute of Technology, 2006.

[77] Zahn, M. *Electromagnetic Field Theory: A Problem Solving Approach*; Krieger Publishing Co.: Malabar, FL, 1979.

[78] Goncalves, F. D.; Ahmadian, M.; Carlson, J. D. *Smart Mater. Struct.* **2006**, *15*, 75–85.

[79] Rankin, P. J.; Horvath, A. T.; Klingenberg, D. J. *Rheol. Acta* **1999**, *38*, 471–477.

[80] Klingenberg, D. J.; Ulicny, J. C.; Golden, M. A. *J. Rheol.* **2007**, *51*, 883–893.

[81] Fermigier, M.; Gast, A. P. *J. Coll. Int. Sci.* **1992**, *154*, 522–539.

[82] Furst, E. M.; Gast, A. P. *Phys. Rev. E* **2000**, *62*, 6916–6925.

[83] Park, B. O.; Park, B. J.; Hato, M. J.; Choi, H. J. *Colloid Polym. Sci.* **2011**, *289*, 381–386.

[84] de Vicente, J.; Lopez-Lopez, M. T.; Gonzalez-Caballero, F.; Duran, J. D. G. *J. Rheol.* **2003**, *47*, 1093–1109.

[85] Lopez-Lopez, M. T.; Zugaldia, A.; Gonzalez-Caballero, F.; Duran, J. D. G. *J. Rheol.* **2006**, *50*, 543–560.

[86] Kordonski, W.; Gorodkin, S.; Zhuravski, N. *Int. J. Mod. Phys. B* **2001**, *15*, 1078–1084.

[87] Rosensweig, R. E. *Ferrohydrodynamics*; Dover: Mineola, NY, 1997.

[88] Fuchs, A.; Zhang, Q.; Elkins, J.; Gordaninejad, F.; Evrensel, C. *J. Appl. Polym. Sci.* **2007**, *105*, year.

[89] Rich, J. P.; McKinley, G. H.; Doyle, P. S. *J. Rheol.* **2011**, *55*, 273–299.

[90] Rich, J. P.; Lammerding, J.; McKinley, G. H.; Doyle, P. S. *Soft Matter* **2011**, *7*, 9933–9943.

[91] Rich, J. P.; Doyle, P. S.; McKinley, G. H. *Rheol. Acta* **2011**, (under review).

[92] Rich, J. P.; McKinley, G. H.; Doyle, P. S. *Langmuir* **2011**, (under review).

[93] Russel, W. B.; Saville, D.; Schowalter, W. *Colloidal Dispersions*; Cambridge University Press: New York, 1989.

[94] Zaccarelli, E. *J. Phys.-Condens. Mat.* **2007**, *19*, 323101.

[95] Grim, R. E. *Clay Mineralogy*, 2nd ed.; McGraw-Hill: New York, 1968.

[96] Mason, T. G.; Weitz, D. A. *Phys. Rev. Lett.* **1995**, *74*, 1250–1253.

[97] Mason, T. G. *Rheol. Acta* **2000**, *39*, 371–378.

[98] Mourchid, A.; Delville, A.; Levitz, P. *Faraday Discuss.* **1995**, *101*, 275–285.

[99] van Megen, W.; Underwood, S. M.; Pusey, P. N. *Phys. Rev. Lett.* **1991**, *67*, 1586.

[100] Jabbari-Farouji, S.; Tanaka, H.; Wegdam, G. H.; Bonn, D. *Phys. Rev. E* **2008**, *78*, 061405.

[101] Shalkevich, A.; Stradner, A.; Bhat, S. K.; Muller, F.; Schurtenberger, P. *Langmuir* **2007**, *23*, 3570–3580.

[102] Ruzicka, B.; Zulian, L.; Ruocco, G. *Langmuir* **2006**, *22*, 1106–1111.

[103] Pignon, F.; Magnin, A.; Piau, J. M.; Cabane, B.; Lindner, P.; Diat, O. *Phys. Rev. E* **1997**, *56*, 3281–3289.

[104] Pignon, F.; Piau, J.-M.; Magnin, A. *Phys. Rev. Lett.* **1996**, *76*, 4857.

[105] Ramsay, J. D. F. *J. Coll. Int. Sci.* **1986**, *109*, 441–447.

[106] Cocard, S.; Tassin, J. F.; Nicolai, T. *J. Rheol.* **2000**, *44*, 585–594.

[107] Abou, B.; Bonn, D.; Meunier, J. *J. Rheol.* **2003**, *47*, 979–988.

[108] Fielding, S. M.; Cates, M. E.; Sollich, P. *Soft Matter* **2009**, *5*, 2378–2382.

[109] Squires, T. M.; Mason, T. G. *Annu. Rev. Fluid Mech.* **2010**, *42*, 413–438.

[110] Valentine, M. T.; Kaplan, P. D.; Thota, D.; Crocker, J. C.; Gisler, T.; Prud'homme, R. K.; Beck, M.; Weitz, D. A. *Phys. Rev. E* **2001**, *64*, 061506.

[111] Oppong, F. K.; Rubatat, L.; Frisken, B. J.; Bailey, A. E.; de Bruyn, J. R. *Phys. Rev. E* **2006**, *73*, 9.

[112] Caggioni, M.; Spicer, P. T.; Blair, D. L.; Lindberg, S. E.; Weitz, D. A. *J. Rheol.* **2007**, *51*, 851–865.

[113] Savin, T.; Doyle, P. S. *Soft Matter* **2007**, *3*, 1194–1202.

[114] Larsen, T. H.; Furst, E. M. *Phys. Rev. Lett.* **2008**, *100*, 4.

[115] Houghton, H. A.; Hasnain, I. A.; Donald, A. M. *Eur. Phys. J. E* **2008**, *25*, 119–127.

[116] Strachan, D. R.; Kalur, G. C.; Raghavan, S. R. *Phys. Rev. E* **2006**, *73*, 041509.

[117] Petit, L.; Barentin, C.; Colombani, J.; Ybert, C.; Bocquet, L. *Langmuir* **2009**, *25*, 12048–12055.

[118] Valentine, M. T.; Perlman, Z. E.; Gardel, M. L.; Shin, J. H.; Matsudaira, P.; Mitchison, T. J.; Weitz, D. A. *Biophys. J.* **2004**, *86*, 4004–4014.

[119] Wegmann, M.; Michen, B.; Luxbacher, T.; Fritsch, J.; Graule, T. *Water Res.* **2008**, *42*, 1726–1734.

[120] O'Brien, R.; Ladbury, J.; Chowdry, B. Isothermal Titration Calorimetry of Biomolecules. In *Protein-Ligand interactions: hydrodynamics and calorimetry*; Harding, S., Chowdry, B., Eds.; Oxford University Press, 2000.

[121] Savin, T.; Doyle, P. S. *Phys. Rev. E* **2007**, *76*, 021501.

[122] Doliwa, B.; Heuer, A. *Phys. Rev. Lett.* **1998**, *80*, 4915–4918.

[123] Weeks, E. R.; Weitz, D. A. *Chem. Phys.* **2002**, *284*, 361–367.

[124] Oppong, F. K.; de Bruyn, J. R. *J. Non-Newtonian Fluid Mech.* **2007**, *142*, 104–111.

[125] Weeks, E. R.; Crocker, J. C.; Levitt, A. C.; Schofield, A.; Weitz, D. A. *Science* **2000**, *287*, 627–631.

[126] Kegel, W. K.; van Blaaderen, A. *Science* **2000**, *287*, 290–293.

[127] Savin, T.; Doyle, P. S. *Phys. Rev. E* **2005**, *71*, 041106.

[128] Volkov, V. S.; Leonov, A. I. *J. Chem. Phys.* **1996**, *104*, 5922–5931.

[129] Kroon, M.; Wegdam, G. H.; Sprik, R. *Phys. Rev. E* **1996**, *54*, 6541.

[130] Crocker, J. C.; Valentine, M.; Weeks, E. R.; Gisler, T.; Kaplan, P.; Yodh, A.; Weitz, D. *Phys. Rev. Lett.* **2000**, *85*, 888–891.

[131] Wirtz, D. *Ann. Rev. Biophys.* **2009**, *38*, 301–326.

[132] Wilson, L. G.; Poon, W. C. K. *Phys. Chem. Chem. Phys.* **2011**, *13*, 10617–10630.

[133] Habdas, P.; Schaar, D.; Levitt, A. C.; Weeks, E. R. *Europhys. Lett.* **2004**, *67*, 477–483.

[134] Squires, T. M.; Brady, J. F. *Phys. Fluids* **2005**, *17*, 21.

[135] Meyer, A.; Marshall, A.; Bush, B. G.; Furst, E. M. *J. Rheol.* **2006**, *50*, 77–92.

[136] Carpen, I. C.; Brady, J. F. *J. Rheol.* **2005**, *49*, 1483–1502.

[137] Sriram, I.; Meyer, A.; Furst, E. M. *Phys. Fluids* **2010**, *22*, 10.

[138] Khair, A. S.; Squires, T. M. *Phys. Rev. Lett.* **2010**, *105*, 4.

[139] Wilking, J. N.; Mason, T. G. *Phys. Rev. E* **2008**, *77*, 055101.

[140] Seifriz, W. *Br. J. Exp. Biol.* **1924**, *2*, 1–11.

[141] Gordon, M.; Hunter, S. C.; Love, J. A.; Ward, T. C. *Nature* **1968**, *217*, 735.

[142] Haber, C.; Wirtz, D. *Rev. Sci. Instrum.* **2000**, *71*, 4561–4570.

[143] Lammerding, J.; Kazarov, A. R.; Huang, H.; Lee, R. T.; Hemler, M. E. *Proc. Natl. Acad. Sci. U. S. A.* **2003**, *100*, 7616–7621.

[144] Lammerding, J. *PhD Thesis*, Massachusetts Institute of Technology, 2004.

[145] Barnes, H. A. *J. Non-Newtonian Fluid Mech.* **1997**, *70*, 1–33.

[146] Ruzicka, B.; Zulian, L.; Ruocco, G. *Phys. Rev. Lett.* **2004**, *93*, 258301.

[147] Negi, A. S.; Osuji, C. O. *Phys. Rev. E* **2010**, *82*, 031404.

[148] Joshi, Y. M.; Reddy, G. R. K. *Phys. Rev. E* **2008**, *77*, 021501.

[149] Kollmannsberger, P.; Fabry, B. *Rev. Sci. Instrum.* **2007**, *78*, 6.

[150] Bozorth, R. M. *Ferromagnetism*; Wiley - IEEE Press, 1993.

[151] Ebert, F.; Dillmann, P.; Maret, G.; Keim, P. *Rev. Sci. Instrum.* **2009**, *80*, 083902.

[152] Coussot, P.; Nguyen, Q. D.; Huynh, H. T.; Bonn, D. *Phys. Rev. Lett.* **2002**, *88*, 175501.

[153] Coussot, P.; Nguyen, Q. D.; Huynh, H. T.; Bonn, D. *J. Rheol.* **2002**, *46*, 573–589.

[154] Bandyopadhyay, R.; Mohan, P. H.; Joshi, Y. M. *Soft Matter* **2010**, *6*, 1462–1466.

[155] Chow, T. S. *Polymer* **1993**, *34*, 541–545.

[156] Chen, K.; Schweizer, K. S. *Phys. Rev. E* **2008**, *78*, 031802.

[157] Steel, R. G. D.; Torrie, J. H. *Principles and Procedures of Statistics*, 2nd ed.; McGraw-Hill: New York, 1980.

[158] Squires, T. M. *Langmuir* **2007**, *24*, 1147.

[159] Rayleigh, J. *The Theory of Sound*, 2nd ed.; Dover, 1945.

[160] Russel, W. B.; Sperry, P. R. *Prog. Org. Coat.* **1994**, *23*, 305–324.

[161] Deen, W. M. *Analysis of Transport Phenomena*; Oxford University Press: New York, 1998.

[162] Beris, A. N.; Tsamopoulos, J. A.; Armstrong, R. C.; Brown, R. A. *J. Fluid Mech.* **1985**, *158*, 219–244.

[163] Park, B. J.; Fang, F. F.; Choi, H. J. *Soft Matter* **2010**, *6*, 5246–5253.

[164] Olabi, A. G.; Grunwald, A. *Mater. Des.* **2007**, *28*, 2658–2664.

[165] Lemaire, E.; Meunier, A.; Bossis, G.; Liu, J.; Felt, D.; Bashtovoi, V.; Matoussevitch, N. *J. Rheol.* **1995**, *39*, 1011–1020.

[166] Cho, M. S.; Choi, H. J. Magnetorheological characterization of polymer-iron composite suspensions. In *Designing, Processing and Properties of Advanced Engineering Materials*; Kang, S.-G., Kobayashi, T., Eds.; Trans Tech Publications Ltd: Zurich-Uetikon, 2004; Vol. 449-452, pp 1201–1204.

[167] Chin, B. D.; Park, J. H.; Kwon, M. H.; Park, O. O. *Rheol. Acta* **2001**, *40*, 211–219.

[168] Lopez-Lopez, M. T.; de Vicente, J.; Bossis, G.; Gonzalez-Caballero, F.; Duran, J. D. G. *J. Mater. Res.* **2005**, *20*, 874–881.

[169] Lim, S. T.; Cho, M. S.; Jang, I. B.; Choi, H. J. *J. Magn. Magn. Mater.* **2004**, *282*, 170–173.

[170] Lim, S. T.; Choi, H. J.; Jhon, M. S. *IEEE Trans. Magn.* **2005**, *41*, 3745–3747.

[171] Ngatu, G. T.; Wereley, N. M.; Karli, J. O.; Bell, R. C. *Smart Mater. Struct.* **2008**, *17*, 8.

[172] Chhabra, R. *Bubbles, drops, and particles in non-Newtonian fluids*; CRC Press: Boca Raton, FL, 1993.

[173] Møller, P. C. F.; Fall, A.; Chikkadi, V.; Derks, D.; Bonn, D. *Philos. Trans. R. Soc. A-Math. Phys. Eng. Sci.* **2009**, *367*, 5139–5155.

[174] Bonn, D.; Denn, M. M. *Science* **2009**, *324*, 1401–1402.

[175] Ocalan, M. *Ph.D. Thesis*, Massachusetts Institute of Technology, 2011.

[176] Shahin, A.; Joshi, Y. M. *Langmuir* **2010**, *26*, 4219–4225.

[177] Klingenberg, D. J.; Zukoski, C. F. *Langmuir* **1990**, *6*, 15–24.

[178] Ginder, J. M.; Davis, L. C.; Elie, L. D. *Int. J. Mod. Phys. B* **1996**, *10*, 3293–3303.

[179] de Vicente, J.; Vereda, F.; Segovia-Gutierrez, J. P.; Morales, M. D.; Hidalgo-Alvarez, R. *J. Rheol.* **2010**, *54*, 1337–1362.

[180] Bossis, G.; Lacis, S.; Meunier, A.; Volkova, O. *J. Magn. Magn. Mater.* **2002**, *252*, 224–228.

[181] Bossis, G.; Lemaire, E. *J. Rheol.* **1991**, *35*, 1345–1354.

[182] Park, J. H.; Kwon, M. H.; Park, O. O. *Korean J. Chem. Eng.* **2001**, *18*, 580–585.

[183] Jolly, M. R.; Bender, J. W.; Carlson, J. D. *J. Intell. Mater. Syst. Struct.* **1999**, *10*, 5–13.

[184] Martin, J. E.; Anderson, R. A. *J. Chem. Phys.* **1996**, *104*, 4814–4827.

[185] Felt, D. W.; Hagenbüchle, M.; Liu, J.; Richard, J. *J. Intell. Mater. Syst. Struct.* **1996**, *7*, 589–593.

[186] Volkova, O.; Bossis, G.; Guyot, M.; Bashtovoi, V.; Reks, A. *J. Rheol.* **2001**, *44*, 91–104.

[187] de Vicente, J.; Ruiz-Lopez, J. A.; Andablo-Reyes, E.; Segovia-Gutierrez, J. P.; Hidalgo-Alvarez, R. *J. Rheol.* **2011**, *55*, 753–779.

[188] Whitesides, G. M.; Grzybowski, B. *Science* **2002**, *295*, 2418–2421.

[189] Grzelczak, M.; Vermant, J.; Furst, E. M.; Liz-Marzan, L. M. *ACS Nano* **2010**, *4*, 3591–3605.

[190] Xia, Y. N.; Gates, B.; Li, Z. Y. *Adv. Mater.* **2001**, *13*, 409–413.

[191] Gracias, D. H.; Tien, J.; Breen, T. L.; Hsu, C.; Whitesides, G. M. *Science* **2000**, *289*, 1170–1172.

[192] Boncheva, M.; Andreev, S. A.; Mahadevan, L.; Winkleman, A.; Reichman, D. R.; Prentiss, M. G.; Whitesides, S.; Whitesides, G. M. *Proc. Natl. Acad. Sci. U.S.A.* **2005**, *102*, 3924–3929.

[193] Cui, H. G.; Webber, M. J.; Stupp, S. I. *Biopolymers* **2010**, *94*, 1–18.

[194] Zhang, S. *Mater. Today* **2003**, *6*, 20–27.

[195] Glotzer, S. C.; Solomon, M. J. *Nat. Mater.* **2007**, *6*, 557–562.

[196] Yin, Y. D.; Lu, Y.; Gates, B.; Xia, Y. N. *J. Am. Chem. Soc.* **2001**, *123*, 8718–8729.

[197] Park, S. J.; Lazarides, A. A.; Mirkin, C. A.; Letsinger, R. L. *Angew. Chem.-Int. Edit.* **2001**, *40*, 2909–2912.

[198] Choi, J.; Rubner, M. F. *Macromolecules* **2005**, *38*, 116–124.

[199] Golosovsky, M.; Saado, Y.; Davidov, D. *Appl. Phys. Lett.* **1999**, *75*, 4168–4170.

[200] Doyle, P. S.; Bibette, J.; Bancaud, A.; Viovy, J.-L. *Science* **2002**, *295*, 2237.

[201] Feng, J.; Joseph, D. D. *J. Fluid Mech.* **1996**, *324*, 199–222.

[202] Haghgooie, R.; Doyle, P. S. *Physical Review E* **2007**, *75*, 061406.

[203] Mohebi, M.; Jamasbi, N.; Liu, J. *Physical Review E* **1996**, *54*, 5407–5413.

[204] Zhang, H.; Widom, M. *Phys. Rev. E* **1995**, *51*, 2099–2103.

[205] Heyes, D. M.; Melrose, J. R. *J. Non-Newtonian Fluid Mech.* **1993**, *46*, 1–28.

[206] Pappas, Y.; Klingenberg, D. J. *Rheologica Acta* **2006**, *45*, 621–629.

[207] Frenkel, D.; Smit, B. *Understanding Molecular Simulation: From Algorithms to Applications*, 2nd ed.; Academic Press: Boston, MA, 2002.

[208] Velev, O. D.; Bhatt, K. H. *Soft Matter* **2006**, *2*, 738–750.

[209] Roberts, G. P.; Barnes, H. A. *Rheol. Acta* **2001**, *40*, 499–503.

[210] Ahniyaz, A.; Sakamoto, Y.; Bergstrom, L. *Proc. Natl. Acad. Sci. U.S.A.* **2007**, *104*, 17570–17574.

[211] Tanase, M.; Silevitch, D. M.; Hultgren, A.; Bauer, L. A.; Searson, P. C.; Meyer, G. J.; Reich, D. H. *J. Appl. Phys.* **2002**, *91*, 8549–8551.